Few-electron Qubits in Silicon Quantum Electronic Devices

Ke Wang

A Dissertation
Presented to the Faculty
of Princeton University
in Candidacy for the Degree
of Doctor of Philosophy

Recommended for Acceptance
by the Department of
Physics
Adviser: Jason R. Petta

September 2014

Abstract

Artificial two-level quantum systems are widely investigated as the fundamental building blocks of future quantum computers. These quantum bits (qubits) can be realized in many solid state systems, including Josephson junction based devices, nitrogen vacancy centers in diamond, and electron spins in semiconductor quantum dots. Among these systems, Si is very promising since it can be isotopically purified to eliminate random fluctuating hyperfine fields from lattice nuclei, leading to ultra-long quantum coherence times. However, lower heterostructure quality, higher electron effective mass and valley degeneracy present many challenges in realizing high quality qubits in Si.

This thesis demonstrates consistent realization of robust single-electron silicon qubits with high yield. With optimized device designs and DC/RF measurement techniques developed at Petta lab in Princeton University, we have achieved versatile quantum control of a single electron, as well as sensitive read-out of its quantum state. By applying microwave radiation to the gate electrodes, we can probe the energy level structure of the system with 1 μeV resolution. We apply bursts of microwave radiation to extract the qubit lifetime, T_1. By experimentally tuning the qubit, we demonstrate a four order of magnitude variation of T_1 with gate voltage. We show that our experimental results are consistent with a theory that takes into account phonon-mediated charge relaxation.

Acknowledgements

I joined Princeton university as one of the first graduate students of Professor Jason Petta. As a result, I had the rare privilege to be involved in the rise of a world class lab. With the patient advises from Professor Petta, I was able to actively participate in setting up the lab, building equipments, and other exciting activities such as concrete mixing, hard soldering, carpentering, cell drilling, wall hammering, machining and heavy lifting.

In the following years of my PhD, I've also had the honor to be trained hand by hand by Professor Petta in many areas of experimental low temperature physics. These fields include but not limited to, nano/micro-fabrication skills, DC and RF measurement techniques, and cryogenics which is literally one of the coolest things in the world (10mK). I would first like to thank Professor Jason Petta for the research opportunities, supports and advices he gave me, and the great lab environment and experimental setups he provided me which made this thesis research possible.

I would also like to thank Princeton University for its supports to graduate students' research life. Claude Champagne, Mary Santay, Barbara Grunwerg, Regina Savadge and Catherine Brosowsky saved me from the details of the lab purchases, travelling and reimbursements, leaving me with the pure fun of spending lab money. Mike Peloso and Bill Dix had introduced me to the art of the machining with a great selection of materials made available by Ted Lewis, while James Kukon and Geoffrey Gettelfinger provided me with thorough safety trainings and timely helium supplies. I thank George Watson, Yong Sun, Joseph Palmer and Michael Geavski for the valuable helps and guidance in the cleanroom. My thesis research would have been impossible without all of their supports.

I want to thank all my colleagues who have made Petta lab one of the most heartwarming places to work in. Michael Schroer and Michael Kolodrubetz helped me with basic lab knowledge and responsibilities when I got started. Panu Koppinen

had taught me how to be efficient in the cleanroom while Chris Payette had taught me the teaching skills to clearly explain these ideas to other people. The lab is a beautiful mix of different personal charismas that keeps our daily research lively. Yuliya Dovzhenko raised our morale with her cheerful spirit, while Jiri Stehlik excited us with the burning passion in his eyes. Loren Alegria then calmed us down with a hint of seriousness by resembling Al Pacino, while Yinyu Liu and Sorawis Sangtawesin imbued the lab with some peaceful Asian culture that is different from my own. I'm relieved to know that brilliant junior graduate students such as David Zajac, Thomas Hazard and Xiao Mi will be taking over the Silicon quantum dot project after my graduation.

The work represented in this thesis would have been impossible without collaborations. The Sturm group at Princeton EE department had provided us with many high quality Si wafers and I've learned a lot about semiconductors from Professor Sturm's patient explanations. Hughes Research Laboratory (HRL) has also provided this project with valuable suggestions and wafers in our efforts to develop high quality Si DQD devices. Nan Yao and Gerry Poirier at Princeton Imaging Analysis Center provided training which made the high quality SEM images in this thesis possible, and Professor John Martinis at UCSB generously provided the 1K pot design for the first refrigerator I've made. I acknowledge helpful discussion with many brilliant theorists I have worked with, such as Jaroslav Fabian, Xuedong Hu, Martin Raith, Peter Stano and Charles Tahan. Finally, the research has been supported by the Sloan Foundation, the Packard Foundation, the Army Research Office, the National Science Foundation, and the Defense Advanced Research Projects Administration.

Finally, I want to especially thank my mother for her understanding and support. I wasn't able to go back to China and pay her a single visit during my six years of PhD, but she had never complained and instead kept encouraging me to pursue my dream. I'm also grateful to all of my family for their continued supports and the cultural environment they have raised me up in. Their philosophies that used to be incomprehensible to me, have gradually become powerful beliefs that keeps my mind focused, peacefully and joyfully, in the heat of scientific research.

To My Mother Xiurong Cui and My Late Father Dafeng Wang

The work described in this dissertation has been published in the following articles and presented at the following conferences:

Phys. Rev. Lett. **111**, 046801 (2013).
Appl. Phys. Lett. **100**, 043508 (2012).

American Physical Society Meeting, March 2014, Denver, Colorado.
American Physical Society Meeting, March 2013, Baltimore, Maryland.
American Physical Society Meeting, March 2012, Boston, Massachusetts.
American Physical Society Meeting, March 2011, Dallas, Texas.

Contents

List of Tables

List of Figures

Chapter 1

Introduction

The invention of the modern computer is one of the greatest scientific achievements of the last century [1]. At the early days of analog computers, it was hardly scalable and practical. However, the invention of the transistor [2] by John Bardeen, Walter Brattain, and William Shockley in 1947, greatly advanced the rate of industrialization, leading to personal computers. This arguably completely revolutionized modern society, from personal life to scientific research.

In a modern computer, the transistor is the basic computation and logic component [1]. The classical information is stored in the classical bit as two possible classical states, namely “0” (off) and “1” (on), realized as the voltage or the current modes. With inventions such as electron-beam lithography and atomic force microscopy, the quantum world becomes experimentally accessible with modern nano-technology. As such, scientists are now actively developing quantum bits (qubits), the building block of the future quantum computer [3, 4].

Quantum mechanics has also often been referred to as “wave mechanics”, since one of the most crucial differences between the quantum and the classical is none other than the word “phase”. The quantum states of the qubit can be written as $|\psi\rangle = \cos\theta\,|0\rangle + e^{i\phi}\sin\theta\,|1\rangle$. As a result, instead of the binary information storage, in a quantum bit the quantum information can be stored anywhere on the Bloch sphere, as an arbitrary quantum superposition of two basis states, with phase information represented in θ and ϕ.

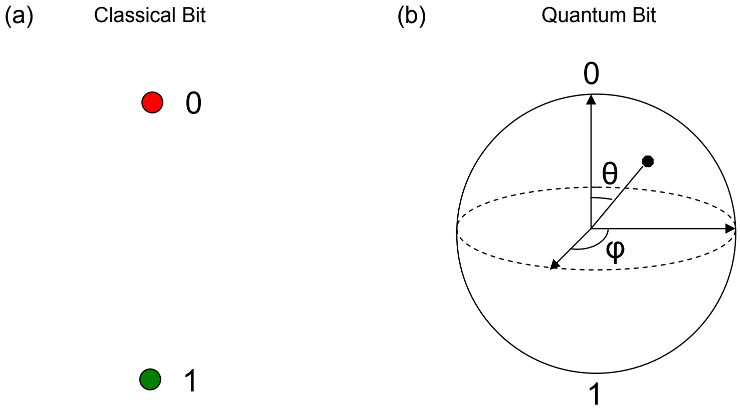

Figure 1.1: The comparison between (a) a classical bit and (b) a quantum bit. In contrast to the classical binary information storage mechanism, quantum information is represented as a superposition of states, $|\psi\rangle = \cos\theta\,|0\rangle + e^{i\phi}\sin\theta\,|1\rangle$.

In addition to this data storage efficiency, quantum computers also promise the enhancement of computational speed and power for many realistic problems, by implementing quantum algorithms [5, 6]. Certain problems that require astronomical computational power from a classical computer can be significantly simplified when they are performed in a quantum computer. One example of a quantum algorithm is the Shor's quantum Fourier transform scheme [5], which provides an exponential enhancement of computational speed over problems such as factorization and ordering, compared to the best known classical algorithms. Another good example is Grover's quantum search algorithm [6] which gives a quadratic computational speed boost in this type of computation. Moreover, the recently developed quantum cryptography schemes, as well as the famous quantum no-cloning theorem [7], promise almost unbreakable quantum information securities.

Similar to the classical computer, the realization of a scalable quantum computer relies on the successful real world implementation of a robust quantum bit. The physical quantum two-level systems can be realized in many different condensed matter environments, such as the circuit quantum electrodynamics system (cQED) [8, 9, 10, 11, 12, 13, 14, 15, 16, 17, 18] utilizing superconducting Josephson-junction-based devices, or in nitrogen vacancy centers in diamond [19].

This thesis focuses on electron qubits in electrically defined semiconductor quantum dots [20, 21, 22, 23, 24, 25, 26, 27, 28, 29]. Motivated by mechanisms to suppress the decoherence in conventional GaAs qubits [21, 30, 31, 32, 33, 34, 35, 36], we have developed a robust device architecture for Si qubits. We demonstrate high quality transport and charge-sensing measurements in Si double quantum dot (DQD) devices. We implement fast single charge sensing using rf reflectometry [37] and probe the energy level diagram of the charge qubit using photon assisted tunneling [38]. We have systematically measured the qubit lifetime T_1, and demonstrate a four order of magnitude tunability of T_1 up to as long as 100 μs.

1.1 GaAs Quantum Dot Devices and Coulomb Blockade

Proposed by Daniel Loss and David DiVincenzo [20, 39], one physical qubit utilizes the spin of electrons trapped in semiconductors. In this proposal, the qubit basis states are defined by the electron spin polarization, with the exchange coupling between adjacent electron spins controlled by gate voltages. This approach has been extremely successful in the past ten years for the experiments based on the AlGaAs/GaAs heterostructures, where the coherent Rabi oscillations as well as dynamic decoupling has been demonstrated in singlet-triplet qubits [21, 30, 31, 33, 34, 32]. The remainder of the chapter will be focused on introducing the charge qubit as well as the S-T_0

qubit in the AlGaAs/GaAs system [21, 30], the discussion of which will eventually motivate the development of Si/SiGe qubit devices.

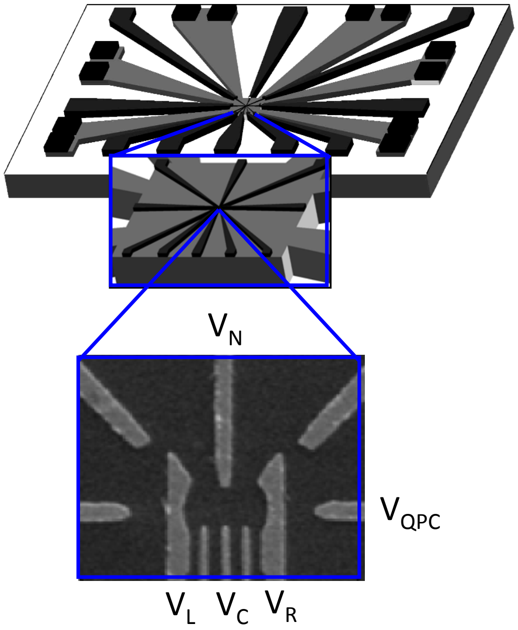

Figure 1.2: A typical DQD device contains a mesa-etched 2DEG, electrically connected with ohmic-contacted arms. On top of the central mesa, a set of gate electrodes are used to form the quantum dot. The gate voltages V_L and V_R define the lead-dot coupling strength, while the gate voltages V_N and V_C set the interdot tunnel coupling strength.

A spin qubit is generally realized in a DQD device fabricated on a semiconductor heterostructure [Fig. 1.2]. Taking the AlGaAs/GaAs system as an example, the most crucial part of the heterostructure is the interface between the n-type AlGaAs and intrinsic GaAs [Fig. 1.2]. The charges that transfer from AlGaAs to GaAs create a triangular quantum well at the GaAs/AlGaAs interface. The free electrons provided by the dopants then reside in it, with the electron wavefunction taking on a quasi two-dimensional form due to the strong confinement in z. This thin layer of electron is generally referred to as a two-dimensional electron gas (2DEG), which provides the electrons the qubit are formed from [Fig. 1.2] [21].

In a typical GaAs quantum dot device, the heterostrucuture is etched into a small mesa (typically on the length scale of 100 μm), which is connected by a few arms leading to the ohmic contacts. A fine set of electron-beam lithography defined gates is deposited on top of the small mesa. As negative gate voltage is applied to these gates to selectively deplete the electrons in the underlying 2DEG, a quasi zero dimensional electron gas in the active device region (quantum dot) is isolated from (and at the same time, weakly coupled to) the rest of the 2DEG (source/drain reservoirs) [21, 30, 31, 33, 34, 32]. In this device geometry, the gate voltages V_L and V_R define the lead-dot coupling strength, while the gate voltages V_N and V_C set the barrier height between the left/right side of the active device region, determining the so called interdot tunnel coupling strength, t_c [Fig. 1.2].

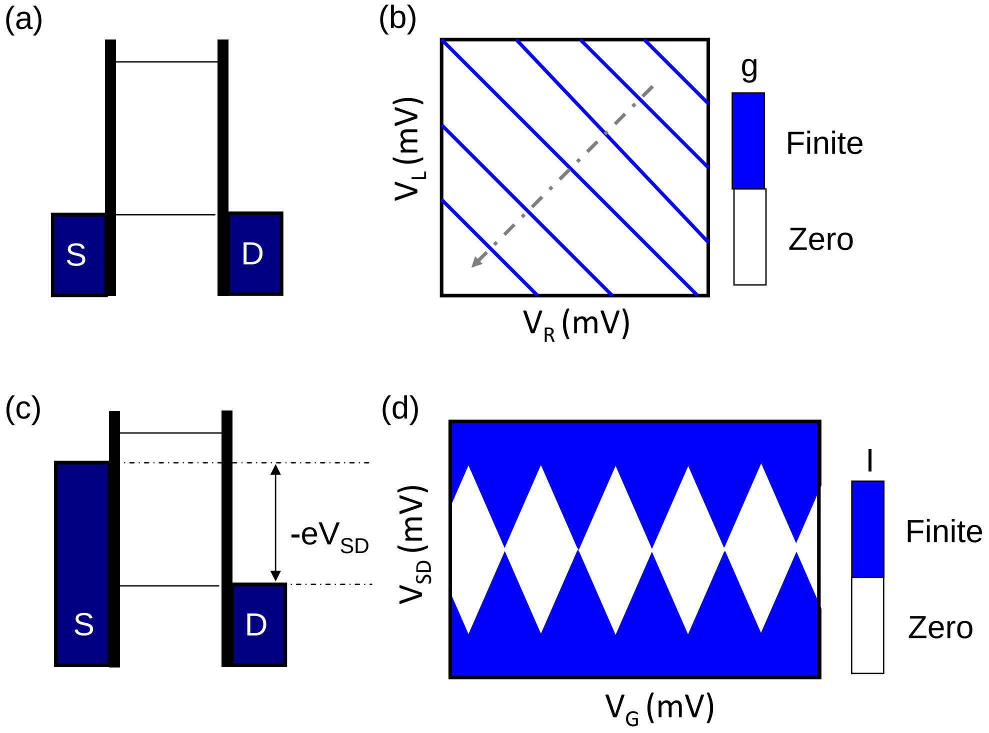

Figure 1.3: At zero bias, when the single quantum dot (SQD) level is (a) in resonance with source-drain chemical potential, a finite conductance is measured. This yields (b) a pattern of parallel lines in the conductance measured as a function of V_L and V_R. At finite source-drain bias, a finite current is measured (c) when one or more dot levels resides in the source-drain bias window. Due to their shape, these features are called (d) Coulomb diamonds.

Due to the strong spatial confinement, the energy levels in the single quantum dot (SQD) are quantized [Fig. 1.3(a)] [21]. In the zero-bias regime, $V_{SD} = 0$, current can only flow through the device when one of the energy levels in the dot matches in energy with the source/drain Fermi level (resonance condition)[Fig. 1.3(a)] [40]. As a result, when the conductance of the quantum dot is measured as a function of V_L and V_R, a non-zero signal appears in a pattern of parallel lines [Fig. 1.3(b)]. Along these lines, the resonance condition is satisfied. As V_L is swept towards more negative values (which raises the dot potential), V_R needs to be swept towards more positive values (which lowers the dot potential) in order to keep the dot energy level in resonance with the lead Fermi level, giving rise to the negative slope of the parallel line pattern in the voltage parameter coordinates. Taking a 1D cut in a direction orthogonal to these parallel lines, as shown by the dashed arrow in [Fig. 1.3(b)], yields a typical set of Coulomb blockade peaks [41, 42, 43]. The gate voltage sweep along this direction is defined as V_G hereafter.

When a finite source-drain bias is applied, a finite current is measured when one or more dot energy levels fall within the source-drain bias window [Fig. 1.3(c)]. Along the vertical axis of Fig. 1.3(c), as the source drain bias voltage $|V_{SD}|$ increases, the source drain bias window becomes larger for the dot energy levels to fall into. As a result, the range of V_G at which through-dot current can be measured scales linearly with $|V_{SD}|$ [Fig. 1.3(d)]. Eventually, when $|V_{SD}|$ becomes greater than the electron charging energy, the dot conduction requirement will always be met, since at least one of the dot energy levels will lay in the source drain bias window. The blockaded region is shaped like a specific symbol in poker cards, hence it is generally referred to as “Coulomb diamonds”.

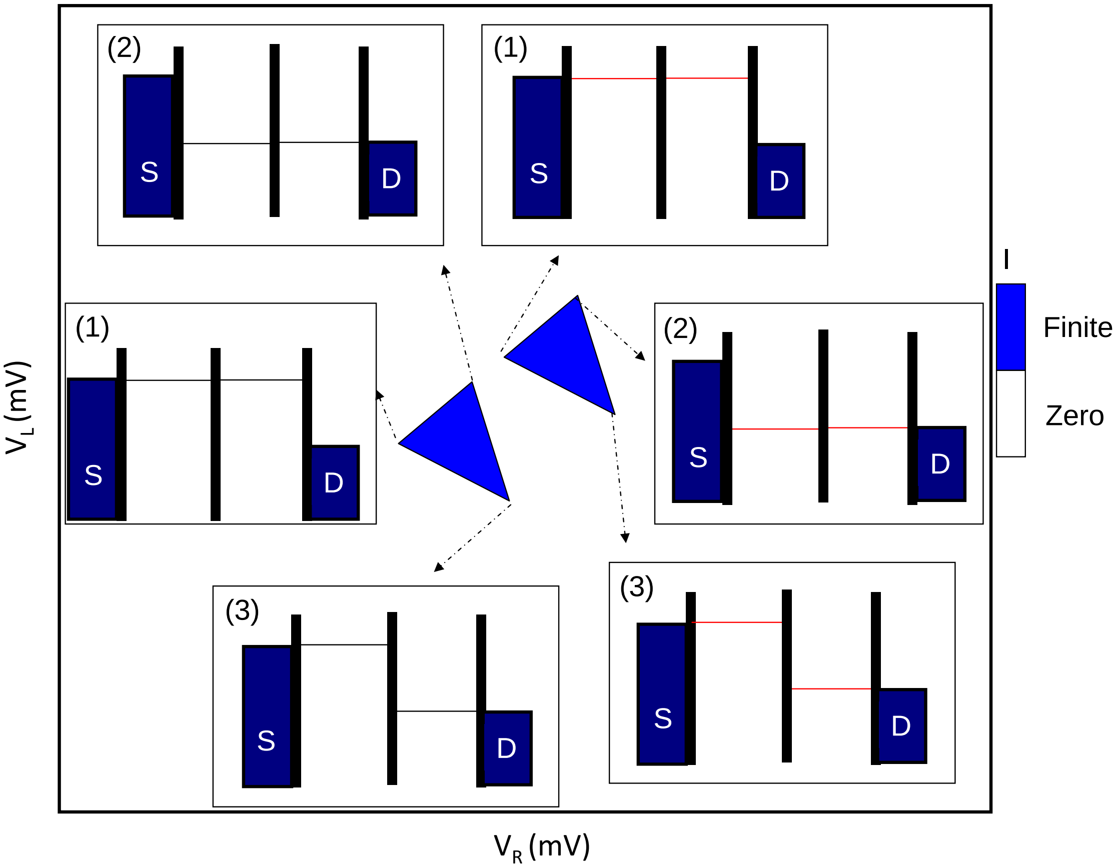

Figure 1.4: Transport through a DQD can be observed when at least one dot energy level for both left dot and right dot lie between the source-drain bias window and the energy level of the left dot is lower/higher than that of the right dot at positive/negative bias. Three extreme points defines the triangular shape of the conduction region, at gate voltages where (1) both left and right dot energy levels are in resonance with source, (2) both left and right dot energy level are in resonance with drain, (3) left dot evergy level is in resonance with source while the right dot energy level is in resonance with drain.

1.2 Double Quantum Dot and Charge Sensing

If a more negative gate voltage is applied to V_N and V_C (which results in a less transparent interdot tunnel barrier), the electron wavefunction originally spanning freely over the entire dot region will be divided into two weakly connected counterparts. As one can intuitively see, the conduction condition becomes harder to meet [21, 44]. At finite source-drain bias, the regions of gate parameter space where current can be measured correspond to the energy level configurations in which [Fig. 1.4] at least one dot energy level for both left dot and right dot fall in the source-drain bias window and the energy level of the left dot is lower/higher than that of the right dot at positive/negative source-drain bias. Three extreme points define the triangular shape of the current region, at gate voltages where (1) both left and right dot energy levels are in resonance with source, (2) both left and right dot energy level are in resonance with drain, (3) left dot energy level is in resonance with source while the right dot energy level is in resonance with drain.

To identify the number of electrons trapped in a quantum dot system, it is helpful to introduce the notation (N_L, N_R), where N_L/N_R is the number of electrons in the left/right quantum dot. Taking negative bias as an example, the electron is pumped one by one from source to drain via the "finite bias triangles" [Fig. 1.4]. There are two distinct ways where this single electron pumping process can happen [44]. One of them is the electron-like process in which an electron is directly pumped from the source to the left dot, then being pumped to the right dot, and then to the drain. This corresponds to a charge transition cycle of (N_L, N_R) $\rightarrow$ (N_L+1, N_R) $\rightarrow$ (N_L, N_R+1) $\rightarrow$ (N_L, N_R), and corresponds to the lower triangle. Another involves the hole-like process where an electron in the right dot is first tunneled to the drain, then another electron in the left dot tunnels to the right dot to take the newly available vacancy, and finally yet another new electron in source tunnels into the left dot to occupy it again, putting the dot back to its original charge occupation. This corresponds to a charge transition cycle of (N_L+1, N_R+1) $\rightarrow$ (N_L+1, N_R) $\rightarrow$ (N_L, N_R+1) $\rightarrow$ (N_L+1, N_R+1) , and corresponds to the upper triangle.

Transport measurements are useful to estimate the tunnel rates as well as the dot configuration. However, the measurement requires exchange of dot electrons with leads, and therefore cannot be used to probe the qubit states. A non-invasive method of determining the dot electron charge configuration was developed in the early days

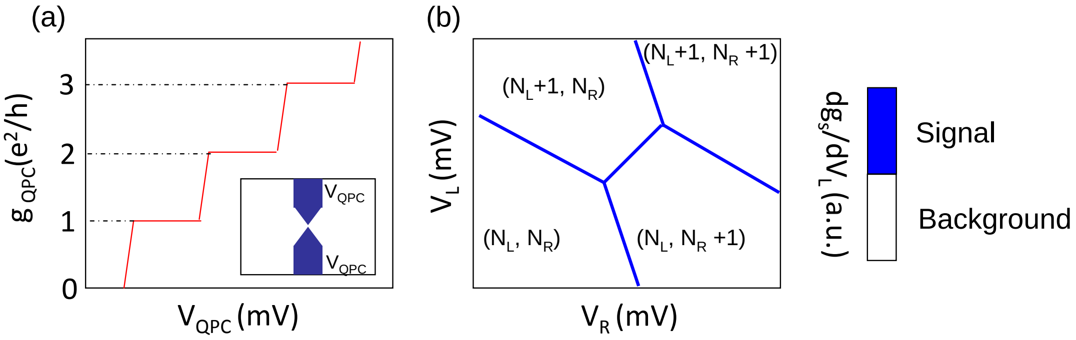

Figure 1.5: (a) Due to the strong confinement in the the QPC channel (inset), measuring conductance g_{QPC} as a function of V_{QPC} yields the famous "quantized steps in conductance", in steps of a single quantum conductance g_0. (b) By parking g_{QPC} at one of the steps in conductance, the quantum dot occupation can be sensitively measured, providing access to the charge stability diagram.

of GaAs quantum dot research, generally known as "charge sensing" [21, 45, 37, 46, 47, 48, 36, 49, 50]. This technique utilizes a nearby gate V_{QPC} which forms a conductance channel together with V_R or V_L, with a channel width comparable to the Fermi wavelength of the 2DEG. Due to the strong confinement in the channel, its energy levels are quantized and a measurement of channel conductance g_{QPC} as a function of V_{QPC} yields the famous "quantized steps in conductance", in steps of a single quantum conductance g_0 [Fig. 1.5(a)].

By parking the QPC conductance g_{QPC} at one of the sharp steps in conductance, even a very small perturbation in local electrostatic potential (due to the change of electron occupation inside the DQD) will result into a robustly measurable response in QPC conductance g_{QPC}. A "charge stability diagram" can be then generated by measuring g_{QPC} as a function of V_L and V_R and then numerically differentiating it. Figure 1.5 shows a typical charge stability diagram near the (N_L+1, N_R) - (N_L, N_R+1) charge configuration, with two sets of parallel lines corresponding to the lead-dot electron tunneling events and the center line (positive slope) corresponding to the interdot electron tunneling events. When the quantum dots are completely emptied of electrons, no more charge transitions will be observed in the left bottom corner of the charge stability diagram. By counting up from the (0,0) charge occupation, we can determine the electron occupation at any arbitrary V_L and V_R.

1.3 Charge Qubits

With knowledge of the charge occupation, we are ready to form a few electron quantum bit in our DQD device [Fig. 1.6(a)]. In the past 15 years, two main types of electron qubits have been widely implemented and investigated in DQD systems, namely charge qubits and singlet-triplet spin qubits.

The basis states $|0\rangle$ and $|1\rangle$ of a charge qubit are the one-electron charge states (1,0) and (0,1) [Fig. 1.6(b)] [38]. Simply sweeping the gate voltage across the (1,0) - (0,1) interdot charge transition (a parameter hereafter defined as detuning, ε) in the stability diagram tunes the left dot potential with respect to the right dot potential, setting the energy splitting between the (1, 0) and (0, 1) states [Fig. 1.6(b)]. Therefore, the diagonal matrix elements of the Hamiltonian is simply $\mathrm{H} = \frac{\varepsilon}{2}\sigma_z$.

The off-diagonal term in the Hamiltonian is given by the interdot tunnel coupling between the left QD and the right QD. In our experiment, the interdot tunnel coupling t_c can be continuously adjusted over a wide range by tuning the gate voltages V_N and V_C, giving a fully tunable Hamiltonian $\mathrm{H} = \frac{\varepsilon}{2}\sigma_z + t_c\sigma_x$. The energy level diagram is plotted as a function of detuning in Fig. 1.6(c). Tunnel coupling leads to an avoided crossing near the zero detuning and an total energy splitting of $\Omega = \sqrt{\varepsilon^2 + 4t_c^2}$.

One way to realize charge qubit manipulation is through the photon-assisted tunneling (PAT) technique [38, 51, 52]. By applying continuous microwaves on one of the gate electrodes [Fig. 1.6(d)], coherent oscillations between the electron charge states can be observed at the detunings where the energy splitting matches with a single photon energy, namely $\Omega = \sqrt{\varepsilon^2 + 4t_c^2} = hf$, in which f is the microwave frequency [Fig. 1.6(e)]. By carefully tracking the PAT peak position as a function of detuning

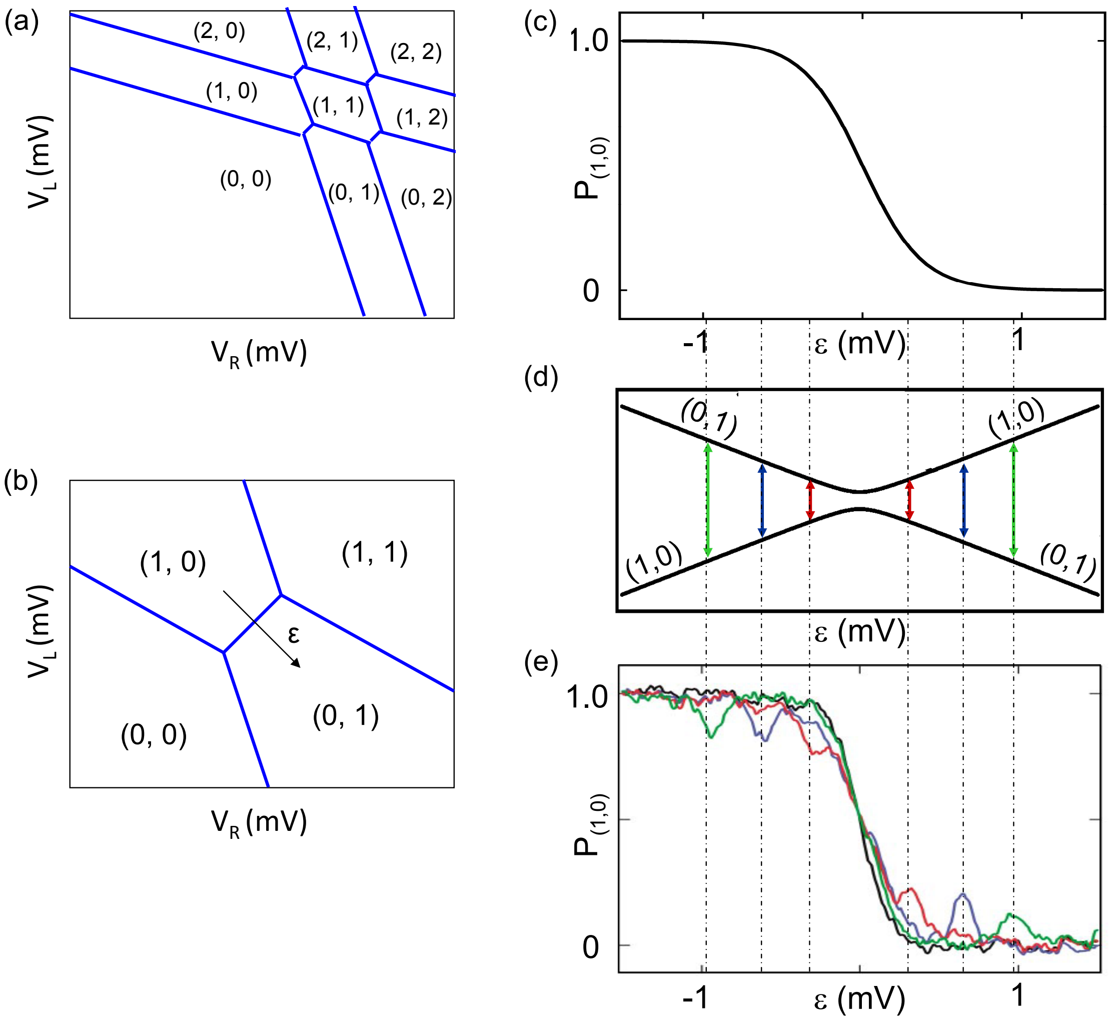

Figure 1.6: (a) Large scale and (b) zoomed in charge stability diagram at the few electron regime. (c) The probability of measuring the electron in the (1,0) charge state, $P_{(1,0)}$, as a function of detuning ε, shows a step like feature with the step width positively correlated with the interdot tunnel coupling t_c. When (d) microwave excitation is applied to one of the DQD gate electrodes, coherent Rabi oscillation happens at the detuning where the energy splitting $\Omega = \sqrt{\varepsilon^2 + 4t_c^2}$ matches with a single photon energy hf. This gives rise to the (e) PAT peaks (data adapted from [38]).

ε and applied microwave frequency f, a detailed energy level diagram of the system can be accurately mapped out. By applying a "chopped" microwave signal with a 50/50 on/off ratio (in the first half of the duty cycle, the microwave is on; while in the second half of the duty cycle, the microwave is off), and stepping the duty cycle period, one can measure the decay behavior of the qubit states and extract from it the charge relaxation time T_1 (In this case, this equals to the qubit lifetime by definition).

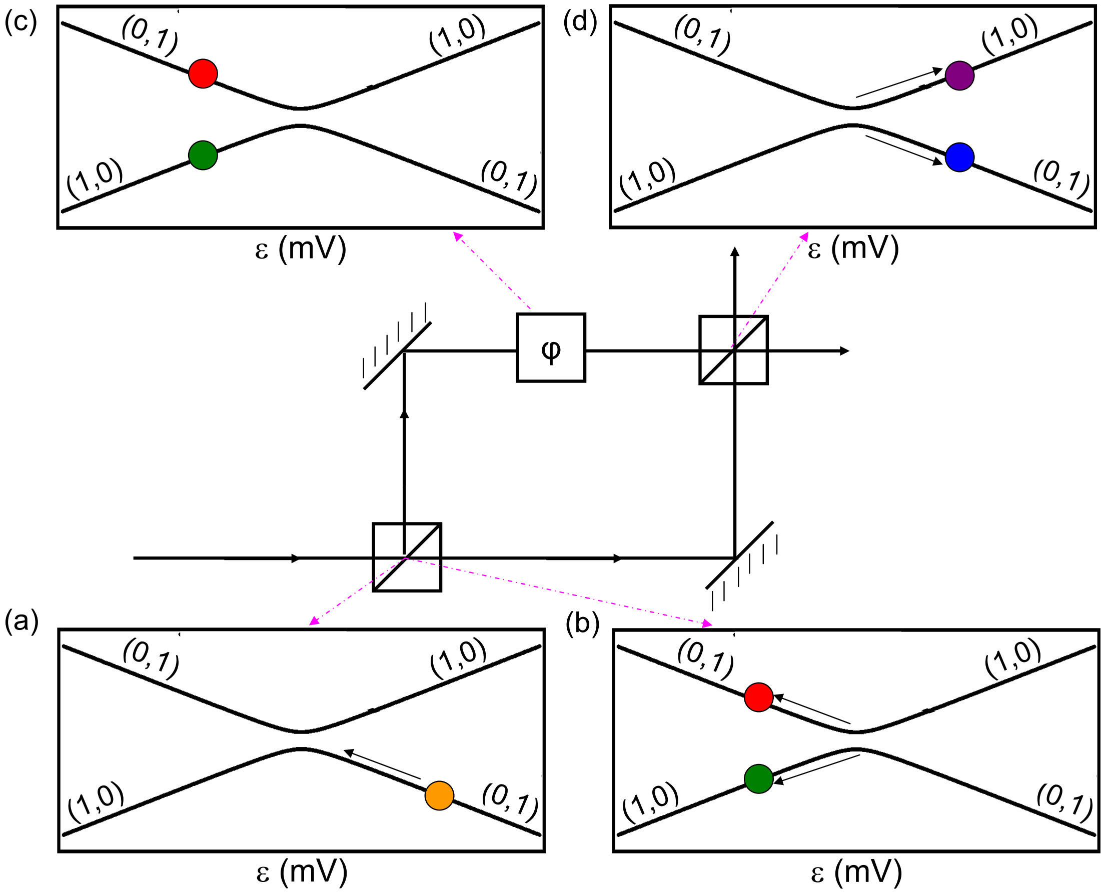

Figure 1.7: A Mach-Zehnder type of experiment can be performed for charge qubit manipulation. (a) The qubit state is initialized in (0,1), and (b) non-adiabatically swept across zero detuning, resulting in a 50/50 probability of finding electron in either the (1,0) or (0,1) charge states. This sweep essentially works like a 50/50 beam splitter. (c) The qubit state will then be allowed to precess in the x-y plane with a certain free evolution time, after which the (d) qubit states will be pulsed back to positive detuning across the avoided crossing. A charge-sensing measurement is then performed. The fundamental physics is very similar to that in the optical Mach-Zehnder interferometry experiment.

Another way of achieving coherent charge manipulation comes from an experimental scheme similar to the Mach-Zehnder interferometry experiment [Fig. 1.7] [53, 33]. Instead of applying a continuous microwave signal, a sequence of voltage pulses is applied to adjust the DQD detuning. As an example, let's choose the initial state to be (0,1), the ground state at positive detuning [Fig. 1.7(a)]. When adiabatically swept across zero detuning from (0,1) to far negative detuning, the new qubit state becomes the new ground state (1,0). However, when the sweep is non-adiabatic and fast compared to the interdot tunneling rate, nearly all of the population remains in the initial state (0,1). There is an intermediate regime [53] where passage through the avoided crossing acts as a quantum beam splitter, with the resulting state being a superposition of (0,1) and (1,0) charge states, depending on the speed of the sweep [Fig. 1.7(b)]. The probability of finding the qubit in the original (0,1) state (non-adiabatic transition), after pulsing across the avoided crossing, is given by the famous Landau-Zener formula, $P = e^{-\frac{2\pi t_c^2}{\hbar v}}$, in which t_c is the interdot tunnel coupling and $v = |d\Omega/dt|$ is the speed of change of the energy splitting for the charge qubit. One can calibrate the pulse speed so that the resulting qubit state contains 50% of both (1,0) and (0,1), analogous to an optical 50/50 beam splitter. Viewing this process in the Bloch sphere, the qubit state is effectively projected onto the x-y plane of the Bloch sphere [Fig. 1.7(b)].

Then the qubit state will precess in the x-y plane with a Larmor frequency proportional to the energy splitting $\Omega = \sqrt{\varepsilon^2 + 4t_c^2}$ [Fig. 1.7(c)], after which the qubit states will be pulsed back to positive detuning across the avoided crossing [Fig. 1.7(d)]. At the end of the pulse cycle, the measurement of the probability of finding the qubit in the (1,0) state, $P_{(1,0)}$, is essentially a Mach-Zehnder interference pattern in which $|1,0\rangle$ and $|0,1\rangle$ are analogous to the two light paths in a conventional Mach-Zehnder experiment. With careful calibration of pulse height and pulse length, coherent manipulation of the charge qubit can be realized using this technique [18, 53].

1.4 Singlet-Triplet Spin Qubits

In contrast to charge qubits, singlet-triplet spin qubits utilize two-electron spin states as the qubit basis states [30]. There are total of four possible spin configurations for an electron pair, namely the singlet state $|S\rangle$, and the triplet states $|T_0\rangle$, $|T_+\rangle$ and $|T_-\rangle$. With a typical 100 mT external magnetic field applied, the four spin states become the ground state $|T_+\rangle$ ($m_s = 1$), the doubly degenerate $|S\rangle$ and $|T_0\rangle$ ($m_s = 0$), and the excited state $|T_-\rangle$ (m_s = -1). The qubit basis states are chosen to be $|S\rangle$ and $|T_0\rangle$, which are energetically well isolated from $|T_+\rangle$ and $|T_-\rangle$ [Fig. 1.8(a)].

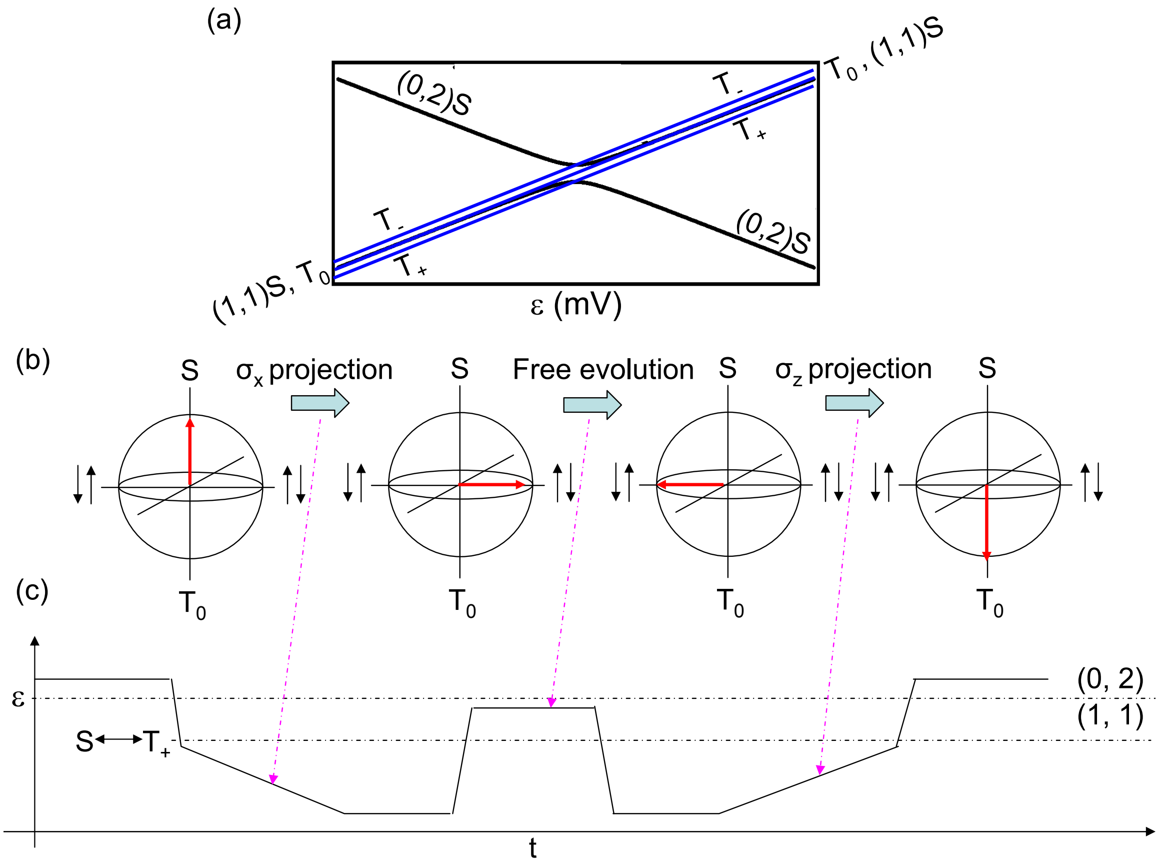

Figure 1.8: (a) The energy level diagram of a S-T_0 qubit. (b) A typical spin manipulation experiment consists of initialization, σ_x projection, free evolution, σ_z projection and spin read out. These are realized by (c) applying a combination of adiabatic and non-adiabatic step pulses to the detuning parameter, ε.

The singlet-triplet qubit can be formed at either the (1,1) - (0,2) or (1,1) - (2,0) charge transitions. In the following context, we will use the (1,1) - (0,2) transition as an example. Similar to charge qubit, the energy splitting between $|S\rangle$ and $|T_0\rangle$ (or the σ_z term in the Hamiltonian) is also experimentally tunable. However, instead of scaling almost linearly with the detuning parameter ε, the singlet-triplet splitting has a more complicated detuning dependence. As required by the Pauli exclusion principle, the total electron wave function is required to be anti-symmetric. So the spatial wavefunction for the $|S\rangle$ state (antisymmetric spin wavefunction) is required to be symmetric. And similarly the spatial wavefunction for the $|T_0\rangle$ state (symmetric spin wavefunction) is required to be antisymmetric. As a result, as long as there is electron wave function overlap between the left quantum dot and the right quantum dot, there will be a difference in terms of spatial electron probability distributions between the $|S\rangle$ state and the $|T_0\rangle$ state. This difference in turn causes different Coulomb repulsion strengths between the two electrons, which then results in a detuning-dependent energy splitting (usually called the exchange coupling $J(\varepsilon)$) between $|S\rangle$ and $|T_0\rangle$.

As previously mentioned, the S-T_0 splitting can be simply tuned by sweeping the detuning parameter ε. When ε is pulsed deep into the (1,1) charge configuration, the two electrons are well separated spatially and have minimum overlap with each other. As a result, there will be minimal difference between the electron probability distribution between the $|S\rangle$ and $|T_0\rangle$ states, giving $J \sim 0$. In the other case, when ε is pulsed deep into the (0,2) charge configuration, the two electrons are forced to reside in the right quantum dot and therefore have maximum overlap with each other. As a result, the exchange splitting J is maximized deep in the (0,2) charge configuration. Figure 1.8(a) shows the energy level diagram of the S-T_0 qubit system.

Now that we have experimentally tunable σ_z matrix elements, what about the σ_x matrix elements? Each electron spin in the GaAs DQD experiences an effective magnetic field via the so called contact hyperfine interaction [21]. The word "contact" arises from the fact that the predominant contribution of the hyperfine field comes from the integration of the electron wavefunction over the divergent point right at the nucleus, instead of the nuclear dipole field itself which decays with $1/R^3$ law. In a typical GaAs DQD, the effective hyperfine field is on the order of a few mT, and is fluctuating as a function of time with a typical timescale of tens of μs [21]. As a result, the hyperfine field in the left quantum dot and right quantum dot are different from one another. It is exactly this field gradient that sets the σ_x matrix element.

The full Hamiltonian can be then written as H $= \frac{J(\varepsilon)}{2}\sigma_z + \Delta B_{nuc}\sigma_x$, in which ΔB_{nuc} is the difference between the nuclear field in left quantum dot and right quantum dot.

A typical Rabi pulse sequence consists the following steps [Fig. 1.8(b)–(c)] [30, 21]. The qubit is initialized in the $|S\rangle$ state, then the detuning is swept non-adiabatically through the $|S\rangle$ - $|T_+\rangle$ anti-crossing, to prevent the leakage of $|S\rangle$ into $|T_+\rangle$ [Fig. 1.8(c)]. After this, the detuning is swept adiabatically deep into the (1,1) charge configuration. In this process, the exchange coupling $J(\varepsilon)$ is adiabatically turned off and the qubit state is therefore projected to the new eigenstates of the system, which are in the x-y plane of the Bloch sphere [Fig. 1.8(b)]. The detuning is then swept back toward zero-detuning non-adiabatically to turn the exchange coupling back on, enabling the qubit to precess in the x-y plane of the Bloch sphere with a Larmor frequency proportional to the exchange coupling $J(\varepsilon)$ [Fig. 1.8(b)–(c)].

At the end of free evolution, the qubit state is projected back onto the σ_z axis [Fig. 1.8(b)–(c)] to perform spin readout using the “spin to charge” conversion technique. The attempt of pulsing the qubit from the (1,1) to (0,2) charge configurations will only be successful when the qubit is in $|S\rangle$ state. If the qubit state is in $|T_0\rangle$, then the (1,1) - (0,2) charge transition will be energetically forbidden due to the large exchange coupling at the (0,2) charge configuration, and the qubit will be blockaded in the (1,1) charge configuration. Utilizing this “spin blockade” [50, 54] and monitoring the qubit charge configuration (using a charge sensor) after pulsing from (1,1) to (0,2), enables us to perform sensitive spin read-out. Combined with the calibrated control of the exchange coupling, coherent control of singlet-triplet qubit has been demonstrated [30].

Chapter 2

Spin Qubit Decoherence Mechanisms - Towards Silicon-Based Quantum Devices

In the previous chapter, we reviewed the successful implementation of charge and spin qubits in GaAs DQDs. In this chapter, we introduce the main decoherence mechanisms in the GaAs system [21, 34], and justify our motivation to move to Si/SiGe based heterostructures in order to improve the robustness of the semiconductor qubits.

We have shown in the previous chapter that coherent spin manipulation can be realized in singlet-triplet qubits in GaAs DQDs. However, the amplitude of the coherent Rabi oscillation is found to quickly decay on a timescale of tens to hundreds of nanoseconds [30]. The processes that lead to the observed decay are generally categorized as qubit relaxation and qubit decoherence. The relaxation process, as the name suggests, corresponds to the qubit relaxation from the qubit excited state ($|0\rangle$) to the qubit ground state ($|1\rangle$). The timescale of relaxation is described by the qubit lifetime T_1, which is strongly correlated with the spin-orbit coupling strength in the host material. The coherence time T_2 describes the timescale that it takes for the qubit to "lose" its in-plane coherent phase information. Many processes can lead to decoherence, such as qubit relaxation, hyperfine interaction, as well as charge noise. In this chapter we will focus on discussing the former two mechanisms, as they can directly be improved by switching to a new qubit host heterostructure with more favorable material properties. Although the qubit coherence time can be significantly improved through the dynamic decoupling techniques (decoherence correction/compensation techniques using trains of well calibrated π-pulses), a more straightforward solution to the qubit decoherence problem is to directly suppress the spin-orbit and hyperfine interaction by moving to Si.

2.1 Spin-orbit Interaction

In a semiconductor qubit, the excited state $|0\rangle$ can relax to the ground state $|1\rangle$ via phonon mediated mechanisms [21, 34, 55]. While this is a straightforward process in charge qubit experiments, the relaxation of pure electron spin states (in spin qubits) involves a spin flip process and therefore a change of spin angular momentum. As a result, phonons are unable to directly participate in the pure spin relaxation process since they carry zero angular momentum. In fact, the spin states are never "pure" in realistic condensed matter systems, as the spin degree of freedom is always coupled to the orbital levels via the spin-orbit interaction [56].

The spin-orbit interaction arises from the relativistic correction of the Schrodinger equation (or equivalently speaking, non-relativistic approximation to the Dirac equation) [57]. Conduction electrons in bands move at the Fermi velocity, which is significantly less than the speed of light [58]. However, the Fermi velocity only represents a time-averaged, center of mass velocity of the electron. Microscopically, each electron in a solid is moving with relativistic velocity relative to the the host lattice nucleus [Fig. 2.1(a)]. As a result of invariant Lorenzian transformation of electromagnetic field

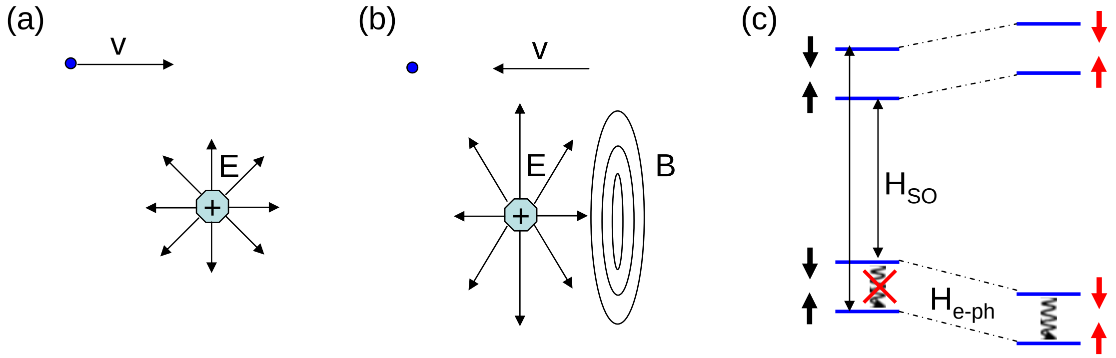

Figure 2.1: (a) In the lab frame, an electron in a solid state environment moves with relativistic velocity relative to the host lattice nuclei. As a result, the electron experiences (b) a "stretched" version of lattice Coulomb potential, and an effective magnetic field in the plane perpendicular to the electron movement. (c) The spin-orbit interaction couples the originally "pure" spin states to the higher orbitals, thereby allowing spin relaxation via spontaneous emission of a phonon.

[59], these relativistic electrons experience a "stretched" version of lattice Coulomb potential, and most importantly, an effective magnetic field in the plane perpendicular to the electron movement with a strength proportional to its velocity [Fig. 2.1(b)]. These characteristics are also well represented in the spin-orbit Hamiltonian, given as

$$H_{SO} = -\frac{\hbar}{4m_0^2c^2}\sigma \cdot \mathbf{p} \times (\bigtriangledown V_0), \tag{2.1}$$

in which $\hbar$ is the reduced Planck's constant, m_0 is the electron mass, σ are Pauli spin matrices, $\mathbf{p}$ is the electron momentum and V_0 is the local Coulomb potential.

The spin-orbit interaction mechanisms are generally categorized into bulk inversion asymmetry induced (BIA) and structure inversion asymmetry (SIA) induced. The BIA spin-orbit interaction (also known as Dresselhaus effect) exists in III-V semiconductors with a zinc blende lattice structure (such as GaAs, whose lattice lacks a center of inversion), while the SIA spin-orbit interaction exists in QD devices with a structure inversion asymmetry of the confinement potential (also known as Rashba effect). It is worth noting that while the SIA spin-orbit interaction is mainly contributed by the macroscopic electric field (which is gate tunable), the BIA spin-orbit interaction is dominated by the microscopic spin-orbit interaction from the atomic cores of the host lattice. For electrons in a 2DEG, the Dresselhaus spin-orbit interaction can be generally written as

$$H_D = \beta[-p_x\sigma_x + p_y\sigma_y], \tag{2.2}$$

where β is a constant describing the strength of Dresselhaus spin-orbit interaction. The Rashba spin-orbit interaction is written in the form of

$$H_R = \alpha[-p_y\sigma_x + p_x\sigma_y], \tag{2.3}$$

where α is a constant describing the Rashba spin-orbit interaction strength.

The strength of the spin-orbit coupling can be represented by the spin-orbit length, which is a function of α and β,

$$l_{SO} = \frac{\hbar}{m\sqrt{\alpha^2 + \beta^2}}. \tag{2.4}$$

The spin-orbit length can be qualitatively understood as the distance over which the electron spin flips due to the spin-orbit interaction. In InAs, the spin-orbit length is usually 100-200 nm [60], while the spin-orbit length in GaAs is on the order of tens of μm [61].

Independent of the specific mechanisms, the pure spin states are coupled to the higher orbitals via the spin-orbit interaction [Fig. 2.1(c)]. And as a result, neither spin nor orbital is a good quantum number anymore and the resulting qubit states become spin-orbit mixed states. The previous selection rule for the pure spin relaxation process is therefore lifted and the phonon's participation in the relaxation process becomes allowed. In order to achieve a long spin qubit lifetime in semiconductor QDs, a weaker spin-orbit coupling strength is therefore desired.

2.2 Contact Hyperfine Interaction and Inhomogenious Spin Dephasing

In this section we will discuss the hyperfine interaction [62, 30, 34, 63, 64, 65] in more detail and show how it leads to spin qubit decoherence. Each nucleus in GaAs carries spin I = 3/2 and therefore generates a nuclear magnetic dipole field

$$\begin{aligned}\mathbf{B}(\mathbf{r},\mathbf{R}) &= \bigtriangledown\times\bigtriangledown\times\left(\frac{\boldsymbol{\mu}}{|\mathbf{r}-\mathbf{R}|}\right)\\ &= \bigtriangledown\left[\boldsymbol{\mu}\cdot\bigtriangledown\left(\frac{1}{|\mathbf{r}-\mathbf{R}|}\right)\right]-\boldsymbol{\mu}\bigtriangledown^2\left(\frac{1}{|\mathbf{r}-\mathbf{R}|}\right),\end{aligned} \tag{2.5}$$

in which $\mathbf{B}$ is the dipole field at $\mathbf{r}$, generated by the nucleus at $\mathbf{R}$, and $\boldsymbol{\mu}$ is the magnetic dipole moment of the nuclear spin [59].

The first term takes the form of

$$\bigtriangledown\left[\boldsymbol{\mu}\cdot\bigtriangledown\left(\frac{1}{|\mathbf{r}-\mathbf{R}|}\right)\right]=\frac{3(\mathbf{r}-\mathbf{R})[\boldsymbol{\mu}\cdot(\mathbf{r}-\mathbf{R})]}{|\mathbf{r}-\mathbf{R}|^5}-\frac{\boldsymbol{\mu}}{|\mathbf{r}-\mathbf{R}|^3}, \tag{2.6}$$

giving the well known dipole field equation that decays by R^3 law. However, this only contributes very marginally to the effective nuclear magnetic field felt by the electrons in the GaAs DQD, as the magnetic dipole field decays quickly at the vicinity of the nucleus. Instead, the hyperfine field is dominated by the contribution from the second term [66], which is given by

$$\boldsymbol{\mu}\bigtriangledown^2\left(\frac{1}{\mathbf{r}-\mathbf{R}}\right)=\boldsymbol{\mu}4\pi\delta(\mathbf{r}-\mathbf{R}). \tag{2.7}$$

Since the dominant term in the Hamiltonian takes the form of Dirac function, the effective nuclear field is also referred to as contact hyperfine field. The strength of the contact hyperfine field depends both on the local nuclear bath and the spatial electron wavefunction. It can be generally written as a sum over all the nuclei in the active device region

$$\mathbf{B}_N = \frac{16\pi v_0}{3g_e}\sum_j \mu_j |u_c(\mathbf{R}_j)|^2 |\psi(\mathbf{R}_j)|^2 \frac{\mathbf{I}_j}{I_j}, \tag{2.8}$$

in which v_0 is the unit cell volume, g_e is the electron g factor, μ_j, $\mathbf{I}_j$ and $\mathbf{R}_j$ are the magnetic moment, spin and coordinate of the jth nuclei, $u_c(\mathbf{r})$ and $\psi(\mathbf{r})$ are electron Bloch wavefunction and electron envelope wavefunction [62].

Due to the fact that the g factor of a nuclear spin is about 1000 times smaller than that of an electron spin, the Zeeman splitting of the nuclear spin is well below the electron temperature (typically measured to be 100 mK in our dilution refrigerators, which corresponds to 8.6 μeV) at a typical external magnetic field of 100 mT. As a result, at any given time, the direction at which each $\mathbf{I}_j$ is pointing is considered to be random and fluctuating. This gives rise to a Gaussian distribution of the total contact hyperfine field, in the form of

$$W(\mathbf{B}_N) = \frac{1}{\pi^{\frac{3}{2}}\Delta B_{nuc}^3} exp\left[-\frac{|\mathbf{B}_N|^2}{\Delta B_{nuc}^2}\right]. \tag{2.9}$$

In a typical GaAs DQD, ΔB_{nuc} is normally found to be on the order of a few mT [21].

In order to see how this Gaussian distribution of the hyperfine field leads to decoherence, let's use a single electron spin as an example. After projecting the electron spin onto the x-y plane of the Bloch sphere, it precesses with a Larmor frequency proportional to the Zeeman splitting, $\omega_L = g_e\mu_B B/\hbar$. The in-plane phase of the spin as a function of time can then be written as $e^{i\omega_n t + i\omega_0 t}$, in which $\omega_n \propto \mathbf{B}_N \cdot \hat{z}$ is contributed by the nuclear field and is therefore fluctuating, and ω_0 is contributed by the 100 mT external field generated by the superconducting magnet and is therefore constant.

In reference [30], spin read-out is performed using a lock-in measurement of the QPC conductance, with a measurement time on the order of tens of ms. Meanwhile, a typical Rabi pulse sequence has a duty cycle period of tens of ns to tens of μs. As a result, for each of the data points taken, it's effectively measuring a time-ensemble-averaged value over many repeated pulse sequences. Due to the fluctuating nature of the hyperfine field, the Larmor frequency fluctuates as a function of time, resulting into a time-ensemble-averaged in-plane spin vector given by

$$< \sigma_x >= \sum_i C_0 exp \left[-\frac{\omega_i^2}{\Delta\omega^2} \right] e^{i\omega_i t + i\omega_0 t} = C_1 e^{-t^2 \Delta\omega^2} e^{i\omega_0 t}, \tag{2.10}$$

where C_0 and C_1 are both constants. This corresponds to coherent in-phase Rabi oscillations $e^{i\omega_0 t}$ that exhibit Gaussian decay with a form e^{-t^2/T_2^2}, and coherence time $T_2 = 1/\Delta\omega \propto 1/\Delta B_{nuc}$.

In order to extend T_2, one can apply the dynamic decoupling pulse sequences, such as spin echo [67, 30] and Carr-Purcell-Meiboom-Gill pulse sequences [68, 69, 35], or simply reduce the number of nuclear spins in the 2DEG. This thesis focuses on using the latter method to improve the lifetime and coherence time of the qubits, by switching from GaAs to Si based DQDs.

2.3 Si/SiGe Heterostructures

In GaAs DQDs, the spin-orbit interaction and the hyperfine interaction are the dominant spin relaxation and decoherence mechanisms. In order to increase spin dephasing times, it is desirable to implement the qubit in a material environment whose decoherence and relaxation mechanisms are significantly reduced. As a result, silicon becomes one of the best candidates for future ultra-coherent qubits [70]. Due to its small atomic number, the spin-orbit coupling strength in silicon is much weaker compared to GaAs. And most importantly, its naturally abundant isotope, ^{28}Si, carries zero nuclear spin. In addition, with the help of isotopic purification, one can create a nearly-nuclear-spin-free environment for qubit electron with a ^{29}Si (which carries nuclear spin I=1/2) concentration smaller than 400 ppm [71].

There are several differences between GaAs and Si 2DEGs [72, 73, 74, 75, 76, 77, 78]. For $Si_{1-x}Ge_x$ alloys, the band structure is "silicon-like" when x<0.85, and the conduction band minima are found along the six equivalent (100) directions. Whereas when x>0.85, the conduction band minima are found along the eight (111) directions and the band structure is "germanium like". The Si/SiGe heterostructures used in this thesis research, either modulation doped or enhancement mode, the SiGe layers consists of $Si_{0.7}Ge_{0.3}$. The indirect bandgap of $Si_{1-x}Ge_x$ is given by Δ = 1.12 - 0.41x + 0.008x^2 eV [79]. For $Si_{0.7}Ge_{0.3}$, we have $\Delta = 0.998$ eV. Taking into account the band alignment of strained $Si_{1-x}Ge_x$/Si heterostructure grown on $Si_{1-y}Ge_y$ substrate [80], the heterostrcuture creates an effective quantum well potential for the conduction electrons with the confinement along the growth direction.

While the lattice mismatch in GaAs system is negligible, there is a 4.2% lattice constant difference between Si and Ge, which induces in-plane strain on the Si 2DEG layer and may also leads to threading dislocations during the wafer growth. Last but not least, while GaAs is a direct band gap semiconductor, the conduction minima in Si are found along the six [100] directions near the X points in the Brillouin zone [81], specifically at $\mathbf{k}$ = [k_0, 0, 0], [-k_0, 0, 0], [0, k_0, 0], [0, -k_0, 0], [0, 0, k_0] and [0, 0, -k_0], where $k_0 \sim 0.85\ \frac{2\pi}{a_0}$.

A two-level system based on spin is required to build the spin qubit. However, adding in the degenerate valley degree of freedom would lead to a 12-state manifold. This provides leakage paths for relaxation and decoherence, and will render the "spin to charge conversion" ineffective as it can lift the spin blockade. It is therefore desirable to have only one low-lying valley, well separated in energy from the higher valley states. In chapter 5, we provide in-depth discussions about valley degeneracy and our new devices designed to overcome this challenge.

In addition to the valley degeneracy, there are many other challenges that need to be overcome before a robust Si qubit can be realized. The relatively low heterostructure quality of the Si/SiGe 2DEG with a typical mobility on the order of $\sim$ 100,000 cm^2/Vs [82, 51], the larger electron effective mass in Si, and the instability of the P donor in modulation doped Si/SiGe wafers, have all presented us with difficulties in our quest to fabricate high quality Si/SiGe DQD devices. In the remainder of this thesis, we explain in detail our experimental approaches to solve each of the problems along our way of realizing robust qubits in Si.

Chapter 3

Depletion-Mode Si Quantum Dots

In the previous chapters, we described the recent successes of spin qubits based on modulation-doped GaAs/AlGaAs heterostructures, and the limitations of their coherence times due to the hyperfine and spin-orbit interactions. As we transition to silicon, whose material properties hold promise for ultra-coherent qubits, a first natural step to take in terms of device fabrication is to reproduce the successful methods in GaAs. Hence, we started this project by investigating depletion-mode DQD devices fabricated on modulation-doped heterostructures.

In this chapter, we systematically explore the relationship between the heterostructure growth profile and 2DEG quality by varying 2DEG depths and doping levels. We identify several heterostructure growth profiles where the 2DEG has low electron density, n, high electron mobility, μ, and shows no evidence of parallel conduction attributable to charge accumulation near the Si cap layer. Double quantum dots fabricated on the most promising wafers are investigated using dc transport and quantum point contact based charge sensing. When tuned to the single dot regime, we observe clear signatures of single electron charging and low electron temperatures, $T_e = 100$ mK. However, we show that the depletion-mode DQD devices are unstable, possibly due to the existence of the P modulation doping layer (see

Chapter 4 for results from undoped devices). The charge population/depopulation of the phosphorus dopants induces switching noise in the device at large negative gate voltages. In addition, the dopants cause potential fluctuations which lead to non-uniform 2DEGs and unintentional quantum dot formation (defect dots).

3.1 Quantum Hall Characterization of Commercially-Grown Depletion-Mode Samples

To fabricate few electron DQDs, we need high quality heterostructures that can provide low electron densities and high mobilities. Based on results from the GaAs system, we desire charge densities $n \leq 5 \times 10^{11}/\text{cm}^2$ and mobilities $\mu \geq 50{,}000$ cm^2/Vs. In order to optimize the 2DEG parameters, we investigated several sample growth profiles using the quantum Hall effect.

We measure the transport properties of Si/SiGe heterostructures grown using chemical vapor deposition by Lawrence Semiconductor Research Laboratories (LRSL). Three main heterostructure growth profiles are investigated, based on previous reports in the literature [83, 84]. Series 1, Series 2, Series 3 are each adapted from heterostructure designs used at HRL Laboratories, Prof. Eriksson's group at the University of Wisconsin Madison [83] and Prof. Sturm's group at Princeton

Table 3.1: Layer thicknesses for three different heterostructure growth profiles

Layer	Series 1	Series 2	Series 3
Si Cap (nm)	7.5	9	11
SiGe Top Spacer (nm)	25	45	25
SiGe Supply Layer (nm)	20	2.6	2.5
Doping Range ($/\text{cm}^3$)	$2\text{–}10\text{x}10^{17}$	$6\text{–}50\text{x}10^{17}$	$5\text{–}50\text{x}10^{17}$
SiGe Bottom Spacer (nm)	5 or 10	22	22
Si Quantum Well (nm)	15	18	10
SiGe Buffer Re-grow (nm)	225	225	225
SiGe Relaxed Buffer (μm)	3	3	3

University [84]. Layer thicknesses and doping profiles are listed in Table 3.1. Relaxed buffer layers are first grown on Si substrates by varying the Ge content from 0 to 30% over a thickness of 3 μm. A 300-nm thick layer of $\mathrm{Si}_{0.7}\mathrm{Ge}_{0.3}$ is grown on the relaxed buffer before it is polished. After polishing, the wafers are completed by growing a 225-nm thick $\mathrm{Si}_{0.7}\mathrm{Ge}_{0.3}$ layer, followed by a strained-Si quantum well, a $\mathrm{Si}_{0.7}\mathrm{Ge}_{0.3}$ bottom spacer, a phosphorus-doped $\mathrm{Si}_{0.7}\mathrm{Ge}_{0.3}$ supply layer, a $\mathrm{Si}_{0.7}\mathrm{Ge}_{0.3}$ top spacer, and a Si cap. The growth structure is shown in the upper left inset of Figure 3.1.

We perform magnetotransport measurements on Hall bars fabricated from the wafers (see upper right inset of Fig. 3.1). Ohmic contacts are made by thermally evaporating a 20/1/30/1/70 nm stack of Au/Sb/Au/Sb/Au and annealing at 390 °C for 10 min. Low-frequency ac lock-in techniques are used to simultaneously measure the longitudinal voltage, V_{xx}, and Hall voltage, V_{xy}, as a function of field, B, with a 10 nA current excitation. Charge density is extracted from the low-field Hall response ($B < 1$ T) and the mobility is extracted from measurements of the zero-field V_{xx}. All measurements were performed in a top-loading dilution refrigerator equipped with a 14 T superconducting magnet. The base temperature of the cryostat is 35 mK.

Figure 3.1 shows typical Hall data measured on a series 1 sample after illumination with a red light-emitting diode (LED) for 1 min. The wafer has a 10-nm bottom spacer layer and doping level of $6 \times 10^{17}/\mathrm{cm}^3$. Clear integer quantum Hall plateaus are visible for filling factors, $\nu = 1$, 2, 4, 6, 8, 10 and 12 at values of $\rho_{xy} = h/(\nu e^2)$. As is the case in Fig. 3.1, we always observe more Hall plateaus for even values of ν than for odd values. This is consistent with previous reports that the valley splitting is smaller than the Zeeman splitting in similar Si/SiGe heterostructures in the quantum Hall regime [85]. The data in Fig. 3.1 also reveal vanishing minima in ρ_{xx} at fields corresponding to the $\nu = 1$, 2, and 4 plateaus. The vanishing quantum Hall minima in ρ_{xx}, coupled with the high mobilities observed, confirm that the 2DEG is the only conduction channel, which is an important prerequisite for operating QD devices.

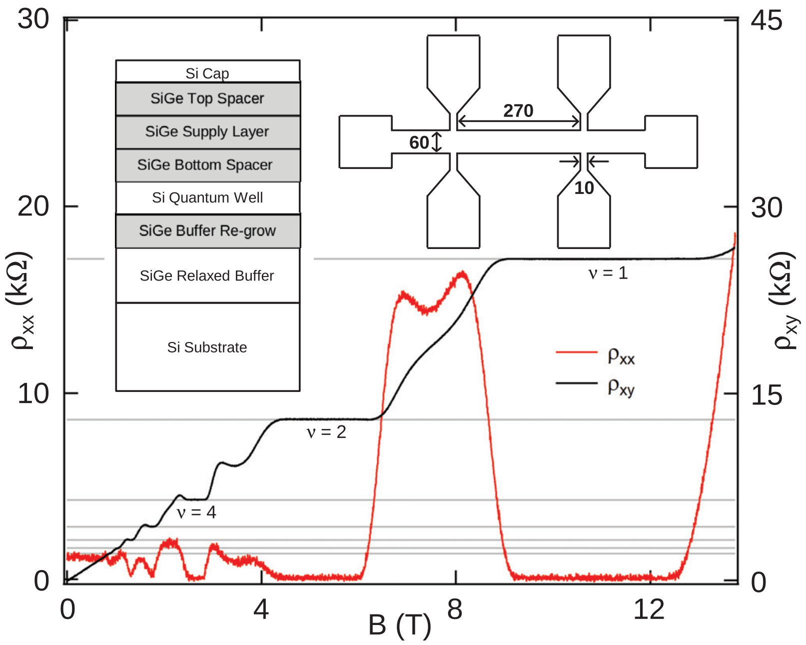

Figure 3.1: Typical Hall data set from which we extract μ = 96,000 cm^2/Vs and n = 2.5 $\times$ 10^{11}/cm^2. Wafer details are given in the main text. Horizontal lines identify the visible quantum Hall plateaus. Upper left inset: Heterostructure growth profile. Upper right inset: Hall bar geometry with dimensions given in microns.

Overshoots in ρ_{xy} on the low-field side of the resolvable quantum Hall plateaus for $\nu > 2$ have been attributed to the co-existence of incompressible strips with different filling factors [85].

3.2 Comparison of Electron Densities and Mobilities Obtained from the Commerically-Grown Modulation-Doped Heterostructures

Hall data were recorded from 16 wafers after illumination with a LED, resulting in the scatter plot of mobility as a function of density shown in Fig. 3.2(a). Hall bars fabricated on the same chip showed variations in carrier density of less than 5% and carrier mobility of less than 10%, provided that there was no evidence of parallel conduction. The data in Fig. 3.2(a) indicate that the specific heterostructure growth profile can have a large impact on 2DEG quality. Series 3 wafers support low density 2DEGs with $n \sim 2 \times 10^{11}/\text{cm}^2$, but the mobility is comparably poor, $\mu < 40{,}000$ cm^2/Vs. While series 2 wafers support low density 2DEGs with $n = 1\text{–}3 \times 10^{11}/\text{cm}^2$, the mobilities are moderate, $\mu \sim 70{,}000$ cm^2/Vs. Series 1 wafers with a 5-nm thick bottom spacer have comparably high mobilities (typically above 60,000 cm^2/Vs and reach a maximum of $\sim$ 90,000 cm^2/Vs). However densities below $3 \times 10^{11}/\text{cm}^2$ were not attainable. Increasing the bottom spacer thickness of the series 1 wafers to 10 nm results in $\mu \sim 100{,}000$ cm^2/Vs with charge densities in the range of $1\text{–}3 \times 10^{11}/\text{cm}^2$. Most GaAs DQD experiments were performed on samples with electron densities in this range and the electron mobilities on the same order of magnitude. Therefore, by extension, this series is the most promising for the fabrication of DQD devices.

For each measured sample, we attempted to perform Hall measurements prior to illumination, but the Ohmic contact resistance for low density samples was on the order of 1 MΩ, independent of wafer series. Illumination typically reduced the contact resistances to a few kΩ allowing us to make reliable Hall measurements. Furthermore, for samples with low Ohmic contact resistance prior to illumination, Hall measurements revealed non-vanishing quantum Hall minima in ρ_{xx} for all but the highest density samples. As a specific example, it is evident in the data in Fig. 3.2(b) that near the $\nu = 1$ plateau ρ_{xx} is finite prior to illumination and vanishes after illumination. However, illumination does not guarantee vanishing quantum Hall minima in ρ_{xx}. For each series, samples with the lowest densities did not exhibit zeros in the longitudinal resistance after illumination [see Fig. 3.2(c)]. Optimum QD device performance will most likely be achieved by illuminating the samples prior to measurements and by selecting material with a moderate density, rather than the lowest measurable density within a series.

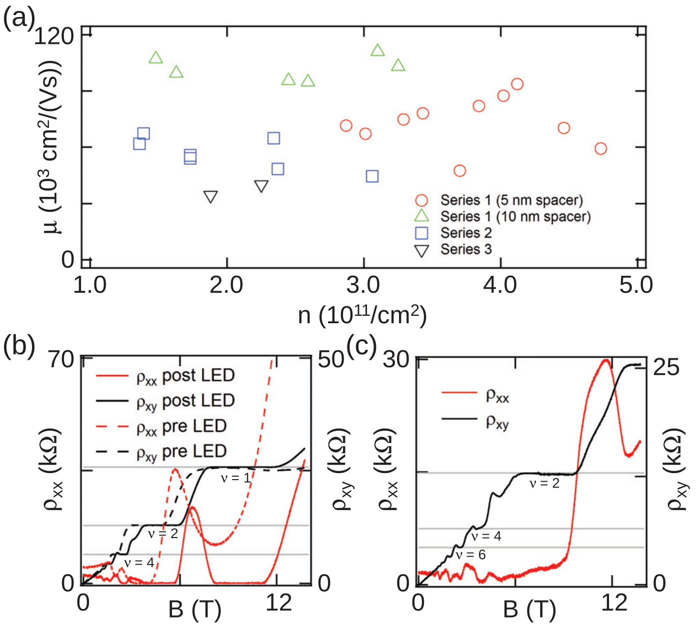

Figure 3.2: (a) Carrier mobility plotted as a function of charge density for each wafer series. (b) Hall data sets recorded before and after illumination with a LED for a series 2 wafer with a doping level of 3 × $10^{18}/\text{cm}^3$, resulting in μ = 30,000 cm^2/Vs and $n = 1.8 \times 10^{11}/\text{cm}^2$ before illumination and μ = 49,000 cm^2/Vs and $n = 2.4 \times 10^{11}/\text{cm}^2$ after illumination. (c) A series 1 wafer (5-nm spacer) with a doping level of 6 × $10^{17}/\text{cm}^3$ does not show clear zeros in ρ_{xx} after illumination with a LED. μ = 48,000 cm^2/Vs and $n = 3.7 \times 10^{11}/\text{cm}^2$ for this sample.

3.3 Coulomb Blockade in Depletion-Mode Single Quantum Dots

The first challenge we face in terms of quantum dot device fabrication is presented by the high effective mass of electron in silicon. In order to create a comparable energy splitting, we need a smaller gate geometry. This can be seen in a simple "particle in the box" equation, $E_n = \frac{n^2h^2}{8m_eL^2}$, in which h is Planck's constant, n is the energy level index, m_e is the effective electron mass and L is the dimension of the box. According to this equation, a three times higher transverse effective mass in Si implies that we need to scale down the electron beam pattern by a factor of 1.73. Through many experiments, we've found an optimum scaling factor of 2.5 [Fig. 3.3].

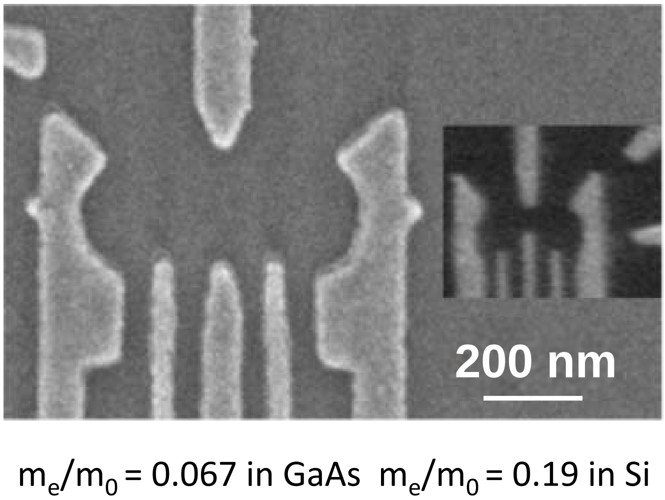

Figure 3.3: Scanning electron microscope (SEM) image of ebeam gates for a typical GaAs DQD device (from ref. [63]) and a typical Si DQD device, plotted with the same scale bar.

This presents considerable technical complications, as the resulting dimensions of the depletion gates have reached the resolution of the 30 keV electron-beam lithography tool available in Princeton at the time of this research.

We have taken many measures in order to successfully scale down the gate geometry. We take into account the proximity effect induced by the backscattered secondary electrons during the exposure of nearby gate electrodes and optimize the individual dose factors of each gate electrode in the active device. We optimize the exposure conditions of the electron-beam lithography tool by performing three-point alignment, adjusting stigmation and aperture, and optimizing the exposure time. With all these efforts, we manage to obtain a reliable electron beam lithography recipe for the much smaller Si/SiGe DQD gate pattern.

After we successfully optimize the electron beam gate recipe, we need high quality Si/SiGe two-dimensional electron gases (2DEGs) with low charge density and high carrier mobility, free of threading defects stemming from the relaxed buffer substrate growth. And on top of this, we need high quality DQD devices with low gate leakage

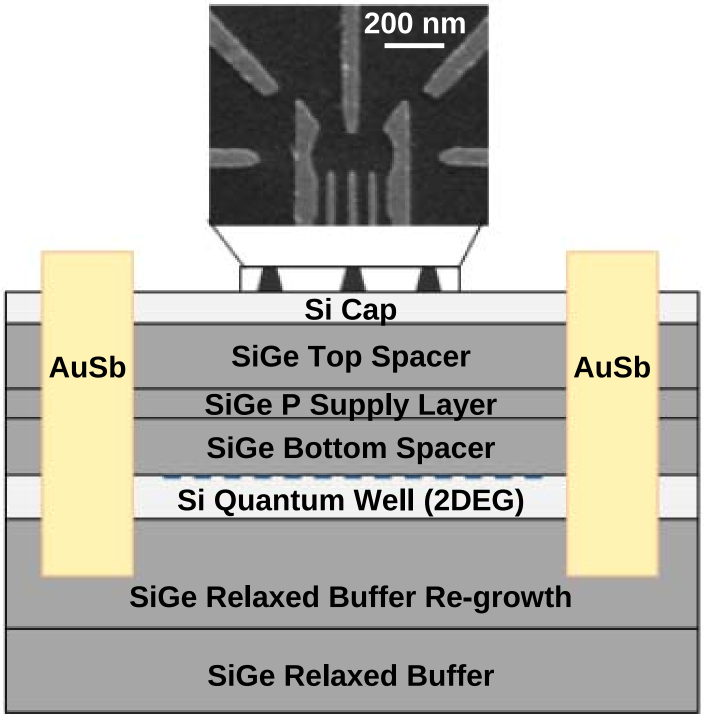

Figure 3.4: Growth profile of a typical depletion-mode silicon double quantum dot device.

and high charge stability, free of switching noise [86, 70, 73, 81, 87]. Based on the quantum Hall characterization, we fabricated QD devices on a series 1 wafer with a 5-nm spacer thickness and a doping level of $8 \times 10^{17}/\text{cm}^3$, which yields $n = 3.4 \times 10^{11}/\text{cm}^2$ and $\mu = 78{,}000\ \text{cm}^2/\text{Vs}$ [Fig. 3.4]. Low-leakage Pd top gates are used to define the DQD [see Fig. 3.4 and inset of Fig. 3.8(c)].

We begin our measurements by operating the device in the SQD regime [Fig. 3.5(a)]. The interdot tunnel coupling is mainly tuned by the gate voltages V_N and V_C. By setting these voltages to comparably positive values, the interdot tunnel barrier becomes transparent and the electron wavefunction spans over the entire active area of the device, formimg a SQD. As shown in [Fig. 3.5(b)], conductance through the DQD measured as a function of V_R and V_L exhibits a pattern consisting of parallel lines, a clear signature of Coulomb blockade. The data in Fig. 3.5(c) are obtained by measuring the conductance along the white line in Fig. 3.5(b). As shown in the data,

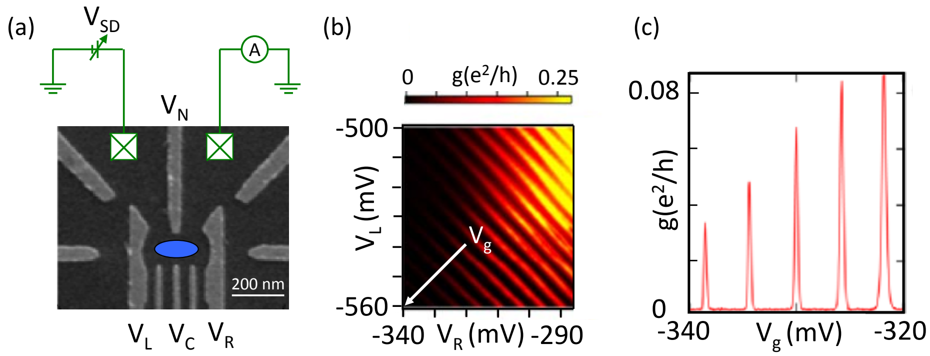

Figure 3.5: (a) SEM image of the device showing the depletion gate pattern and the measurement circuit. (b) Dot conductance, g, measured as a function of V_L and V_R. The periodic modulation of the conductance is due to Coulomb blockade. (c) Conductance g as a function of V_g.

we have obtained high quality Coulomb blockade peaks. The gate voltage along this indicated direction is hereafter defined as V_g.

Figure 3.6 shows the conductance, g, through the device measured as a function of gate voltage, V_g, and bias voltage, V_{SD}, yielding clear Coulomb diamonds in the single dot regime. The absence of abrupt switching during this 14-hour scan demonstrates the excellent stability of the device in single dot regime.

The shape of Coulomb blockade peak is described by the equation $\frac{g}{g_{max}} = \cosh^{-2}\left(\frac{e\alpha\Delta V}{2.5k_B T_e}\right)$, in which g_{max} is the height of the CB peak, ΔV is the gate voltage with respect to the CB peak position, k_B is Boltzmann's constant, T_e is the electron temperature and α is the lever arm conversion between gate voltage and energy. This parameter can be extracted by studying the CB diamond shown in Fig. 3.6. At the top or bottom point of any specific single CB diamond, the dot energy level configuration is such that $|eV_{SD}| = E_c$, in which E_c is the charging energy. Therefore, the difference in V_{SD} between these two points (ΔV_{SD}) is related to the charging energy by the relation $|e\Delta V_{SD}| = 2E_c$. Meanwhile, the difference between the left and right point of the same CB diamond (ΔV_g) is related to the charging energy by the relation $|\alpha(e\Delta V_g)| = E_c$. Therefore, the lever arm is given by $\alpha = \frac{\Delta V_{SD}}{2\Delta V_g}$. By fitting the Coulomb blockade peak shown in the inset of Fig. 3.6, we extract an electron

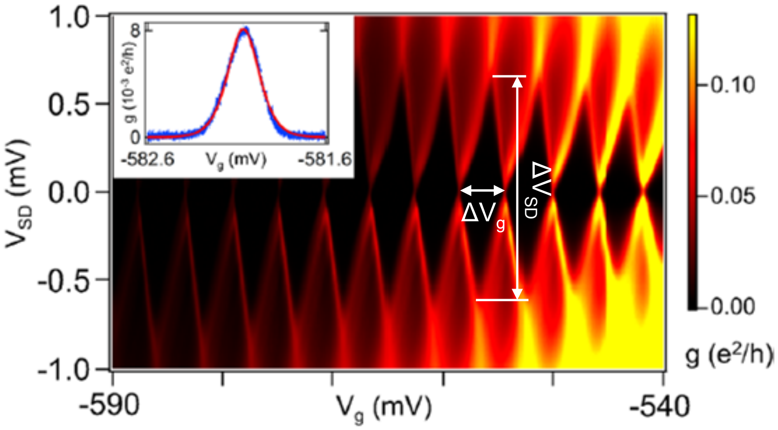

Figure 3.6: Colorscale plot of QD conductance, g, as a function of V_g and V_{SD}. Clear Coulomb diamonds are observed when the device is configured as a single dot. Inset: Conductance as a function of V_g for $V_{SD} = 0$.

temperature $T_e = 100$ mK [41]. We consistently observe electron temperatures in the range of 100–150 mK, which suggests that previous reports of high electron temperatures in Si QDs may be due to sample quality or electrical filtering [88].

3.4 Tranport Measurements and Charge-Sensing in Depletion-Mode Double Quantum Dots in the Many-Electron Regime

In the last section, we explored the single-dot regime and demonstrated single-electron charging and low electron temperatures. We now increase the interdot barrier height to explore the double dot regime [Fig. 3.7(a)]. Finite bias triangles in measurements of the dc current, I, as a function of V_L and V_R have been observed, and are a clear signature of DQD charging physics [Fig. 3.7(b)].

We measure the charge stability diagram of the DQD using a proximal QPC as a charge sensor [Fig. 3.7(c)]. Figure 3.7(d) shows the QPC channel conductance, g_{QPC}, as a function of QPC gate voltage V_{QPC}. The QPC conductance is quantized in steps

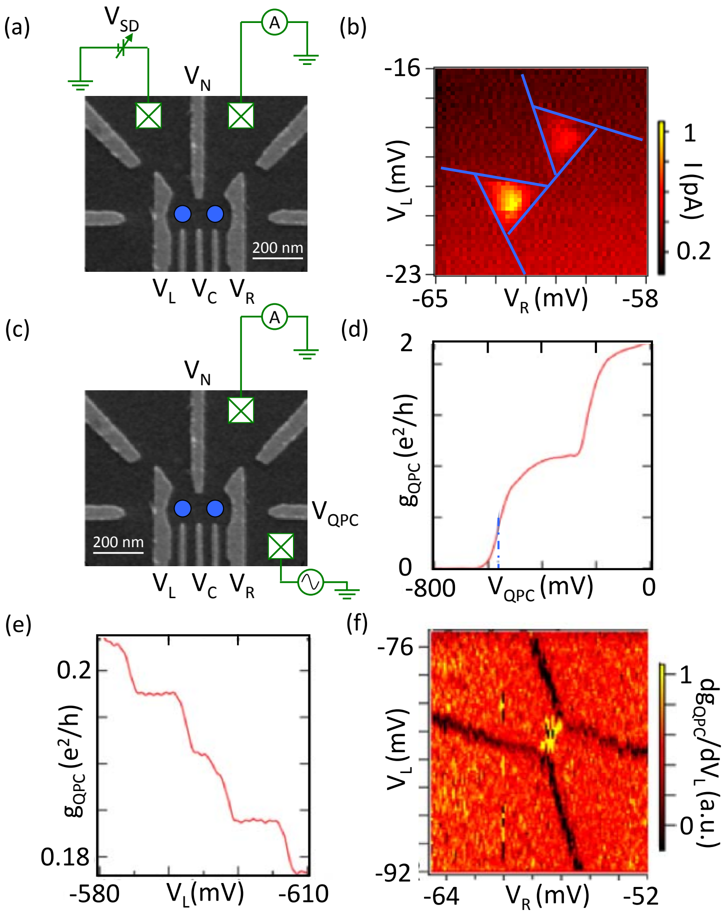

Figure 3.7: (a) DC current through the dot is measured at the double dot regime, where a high interdot tunnel barrier is established by comparably negative V_N and V_C voltages. (b) Typical finite bias triangles at many electron regimes, measured in current. (c) Charge sensing measurement is carried out by measuring the conductance across the proximal QPC channel. (d) The QPC conductance, g_{QPC}, as a function of QPC gate V_{QPC}. When g_{QPC} is parked at one of the steps in conductance (denoted by the blue line), it is highly sensitive to local electrostatic potential. A single electron tunneling event will result into an electrostatic potential change at the QPC that leads to (e) a measurable change in g_{QPC}. (f) Charge stability diagram of a DQD as a function of V_L and V_R.

of conductance quanta g_0. To operate the QPC channel as a charge sensor, we park the gate voltage at one of the steps in conductance (denoted by the blue line). At this configuration, the QPC conductance g_{QPC} is highly sensitive to the local electrostatic potential. Even single-electron tunneling events will therefore result in electrostatic potential changes at QPC that lead to a measurable change in g_{QPC} [Fig. 3.7(e)]. The DQD charge stability diagram can be mapped out by performing QCP conductance measurements as a function of V_L and V_R. These data are then differentiated with respect to V_L, resulting in the data shown in [Fig. 3.7(f)]. Black transitions (negative slopes) correspond to charge transitions that change the total number of electrons, while yellow transitions (positive slopes) correspond to interdot charge transitions. We observe clear charging lines that correspond to interdot charge transitions, where the total electron number is fixed, and transitions with the leads, where an electron is either added or removed from the DQD. The differentiated sensing data shows a clear honeycomb pattern, indicative of a typical DQD.

3.5 Towards the Few-Electron Regime in Depletion-Mode Double Quantum Dots

Although we have obtained stable transport and charge-sensing data in the many-electron regime, attempts to completely empty the DQD of electrons were unsuccessful due to the onset of switching noise at large negative gate bias voltages [Fig. 3.8(a)]. We attribute this to the random charging events at the P dopants [Fig. 3.8(b)]. In addition to this complication, we have also encountered accidental dot formation before we can enter the few-electron regime. Figure 3.8(c) shows the derivative of the charge sensor conductance, dg_{QPC}/dV_L, plotted as a function of the gate voltages V_L and V_R at more negative gate bias voltages. In contrast to the cleanest GaAs double dot devices [30], the stability diagram shows transitions with three distinct negative slopes, indicative of accidental triple QD formation [89]. The data suggests that the existence of P dopants may also introduce spatially fluctuating potential landscape. This results in a non-uniform 2DEG, and makes it difficult to form a well-controlled and symmetric double quantum well potential.

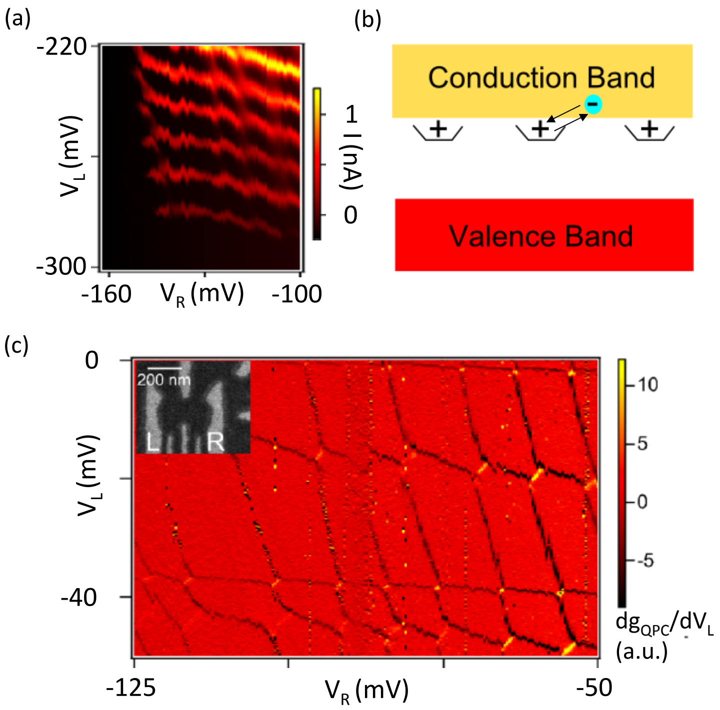

Figure 3.8: (a) Current measurement through the dot, as a function of V_L and V_R, at more negative gate voltages, in an attempt to enter the few-electron regime. The data display a honeycomb pattern, indicative of a DQD charge stability diagram. However, the data are switchy due to local charge fluctuations. (b) The charge noise may be due to random charge population/depopulation of the P dopants, which begins at large negative gate biases. (c) Charge sensing measurement of another device, with a similar gate electrode design. Derivative of the charge sensor conductance, dg_{QPC}/dV_L, measured as a function of V_L and V_R. Inset: SEM image of of a DQD similar to the one measured.

3.6 Summary

In this chapter I have described our attempts to fabricate few-electron DQD devices using depletion-mode Si/SiGe heterostructures. The depletion-mode quantum well structures are commercially grown by LSRL. We first characterized these wafers through measurements of the Hall mobility and electron density. We then scaled down the gate electrode pattern to account for the effective mass difference between GaAs and Si. This allowed us to make many-electron SQD devices and DQD devices with charge-sensing capabilities, from which we extracted an electron temperature of ~100 mK. However, the existence of the P dopant layer prevented us from reaching the few-electron regime in a DQD, motivating the development of dual-gated DQD devices discussed in the next chapter [90].

Chapter 4

Dual-Gated Silicon Quantum Dots

While Si closely approximates a "semiconductor vacuum" for electron spins, its electronic band structure leads to potential complications that are absent in the conventional GaAs/AlGaAs 2DEG system. In the previous chapter, we saw that the ~ 3 times larger effective mass of electrons in Si requires depletion gate patterns to be scaled down significantly, in order to achieve orbital level spacings comparable to those obtained in GaAs. In addition, the band structure of bulk Si consists of six degenerate valleys, which introduces an additional decoherence pathway [91]. Valley degeneracy is partially lifted by uniaxial strain in a Si/SiGe heterostructure [81]. However, the energy splitting between the lowest two valleys is highly sensitive to device specifics, such as step-edges in the quantum well [92, 93, 90]. Detailed measurements of the low-lying energy level structure and the timescales that govern energy relaxation between these levels, are therefore needed in Si quantum dots [94].

In this chapter, we systematically measure the interdot relaxation time T_1 of a single electron trapped in a Si DQD as a function of detuning ε and interdot tunnel coupling t_c. We demonstrate a four order of magnitude variation in T_1 using a single depletion gate and obtain $T_1 = 45\ \mu$s for weak interdot tunnel coupling [38]. We also use photon assisted tunneling (PAT) to probe the energy level structure of the single

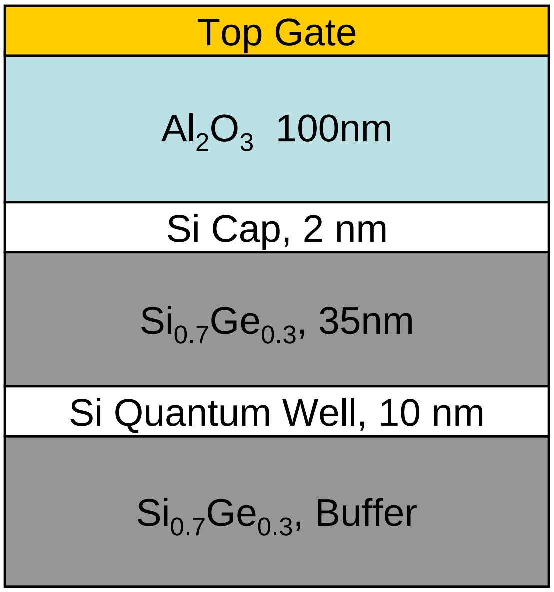

Figure 4.1: Profile of a typical undoped Si/SiGe heterostructure. Doping layer and dopants are absent in the heterostructure. Instead, the 2DEG is accumulated by applying positive voltages to the global top gate.

electron system, demonstrating spectroscopy with an energy resolution of $\sim 1\ \mu$eV. In contrast to single-electron GaAs dots, we observe low-lying excited states $\sim 55\ \mu$eV above the ground state, an energy scale that is consistent with previously measured valley splittings [92, 90].

4.1 Undoped Si/SiGe Heterostructures

In the previous chapter, we demonstrated charge-sensing and transport measurements in depletion-mode DQD devices fabricated on modulation-doped Si/SiGe heterostructures. However, we were unable to reach the few electron regime in the DQDs due to device instabilities and unintended formation of triple quantum dots at low charge occupancies. Based on results from HRL [90], where undoped structures were used, we have concluded that the only path forward is to redesign the heterostructure and

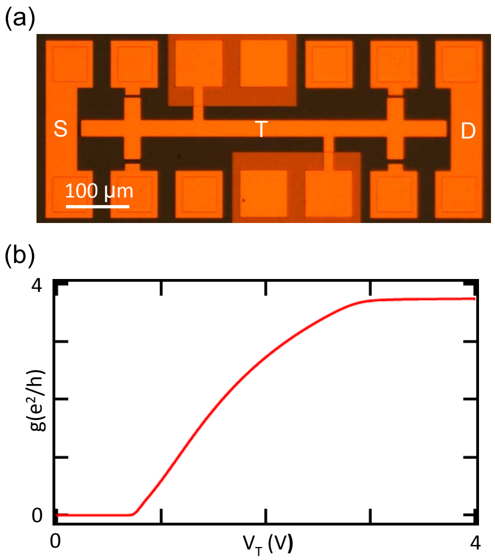

Figure 4.2: (a) Optical image of a typical accumulation-mode Hall bar device. Main contacts are labeled as S (source), D (drain) and T (top gate). (b) Conductance g as a function of top gate voltage V_T. The 2DEG turns on at $V_T = 800\ mV$ and saturates at $V_T = 3000\ mV$.

eliminate the phosphorus donors altogether, using a global top gate to accumulate the 2DEG gas instead.

Figure 4.1 shows the growth profile of a typical undoped Si/SiGe heterostructure. To characterize the heterostructure, we fabricate accumulation-mode Hall bars [Fig. 4.2(a)] and measure the longitudinal conductance as a function of top gate voltage, V_T. As shown in Fig. 4.2(b), the conductance turns on around $V_T = 800\ mV$ and increases as the top gate is swept to more positive voltages, until it saturates at $V_T = 3000\ mV$. As shown in Fig. 4.3, we have systematically measured the electron density n and electron mobility μ as a function of V_T. At an electron density of $\sim 1 - 6 \times 10^{11}/\mathrm{cm}^2$, we measure a mobility of $\sim$ 25,000 - 70,000 $\mathrm{cm}^2/\mathrm{Vs}$.

In the early stages of accumulation mode device development, we frequently encountered sudden top gate voltage threshold shifts. Specifically, the turn-on voltage would shift to more positive top gate voltages after a piece of electrical equipment is turned on or off, or after static charges are suddenly transfered around the device.

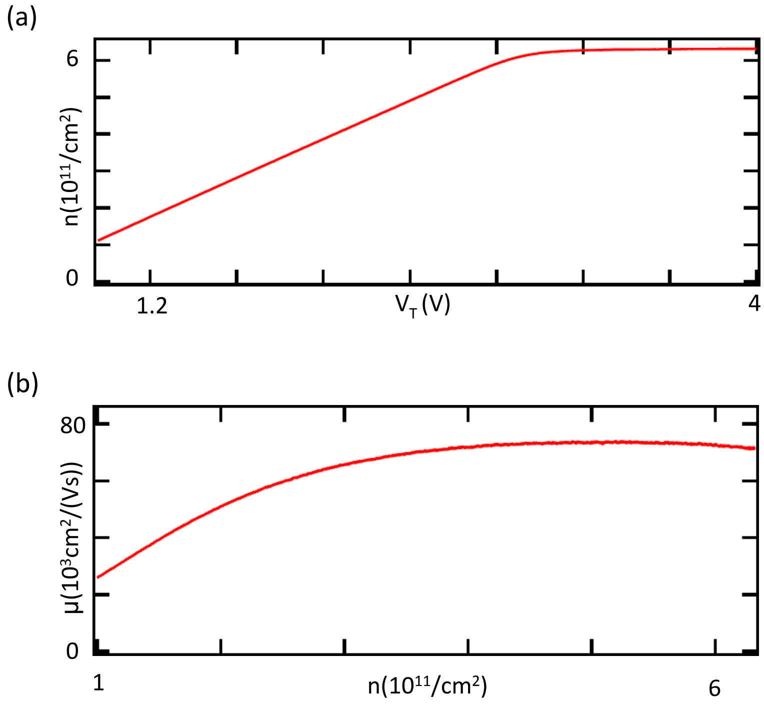

Figure 4.3: (a) Measured 2DEG density as a function of top gate voltage. (b) Measured electron mobility μ as a function of electron density n.

We attribute these random shifts to the voltage spikes in the measurement setup. We have found that the electrical properties of the device will be significantly altered if the top gate voltage is brought above the saturation voltage due to static discharge, even for a very short time period. We conducted systematic measurements to determine the relationship between the 2DEG saturation and the device shift.

Figure 4.4(a) shows six consecutive measurements of conductance g as a function of V_T. The turn-on voltage shifts by 1-2 V each time the device conductance is swept past saturation. The arrows denote different stages of charge accumulation. In the isolation stage (I), no electrons have accumulated in the Si quantum well and the device is insulating. In the accumulation stage (A), charge accumulates linearly with V_T, until it stops accumulating in the saturation stage (S). Figure 4.4(b) shows a simulated band diagram of the heterostructure in each of the three conductance stages, plotting the conduction band minimum as a function of distance from the top surface of the sample. These simulations, combined with the experimental observations, clearly explain the origin of the device shifts.

In the isolation stage, the conduction band minimum is well above the Fermi level across the entire heterostructure, resulting into no electrical conductivity. The conduction band minimum in the Si 2DEG layer is brought below the Fermi energy in the accumulation stage, so the device becomes conductive. As the gate voltage increases, more electrons accumulate in the 2DEG, resulting in an increase in conductance with V_T. However, with increasing top gate voltage the conduction band minimum in the Si cap layer eventually falls below the Fermi level, resulting in electron accumulation in the Si cap layer instead of the Si quantum well. Unlike the nearly-free 2D electrons in the Si quantum well, the newly accumulated electrons in the cap layer may be captured by charge defects at the rough interfaces, and therefore do not conduct, resulting in saturation of the device conductance. Furthermore, since these electrons are trapped, sweeping the top gate voltage back to zero will not release them back to the reservoir. The trapped electrons at the Si cap layer act effectively as a global negative top gate which shifts the electrical properties of the active 2DEG (such as the turn-on voltage).

Now that we fully understand the device shift problem, we are able to take effective measures to prevent it. By adding long time constant RC filter on the DAC filter and directly onto the circuit board, setting up a copper strap to allow a low resistance path between the measurement set up and the ground, operating device away from the saturation voltage and taking extra care handling electrical equipment connected to the sample, we are able to minimize the risk of device shifting in our experiments.

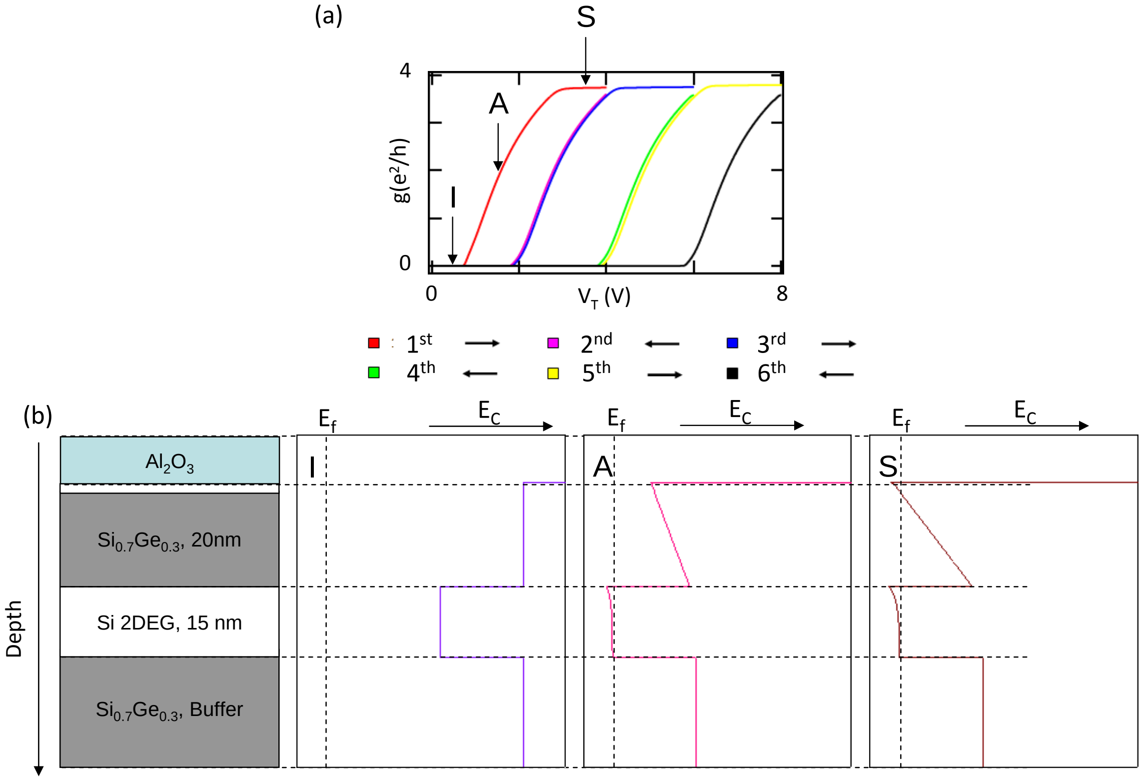

Figure 4.4: (a) Six consecutive measurements of the longitudinal conductance g as a function of top gate voltage V_T. The arrows denote different stages of the device operation, namely the isolation stage (I), the accumulation stage (A) and the saturation stage (S). (b) Simulated band diagrams of the heterostructure in each of the three conductance stages, showing the conduction band minimum as a function of depth.

4.2 Dual-Gated Few-Electron Double Quantum Dot With Fast Single-Charge Sensing

Now that we fully understand the properties of the accumulation-mode 2DEG, we can fabricate dual-gated-mode Si/SiGe DQD devices. We apply a top gate voltage $V_{\mathrm{T}} = 2$ V to accumulate carriers in a Si quantum well located ~ 40 nm below the surface of the wafer [see Fig. 4.2(a)]. The resulting 2DEG has an electron density of $\sim 4 \times 10^{11}/\mathrm{cm}^2$ and a mobility of $\sim$ 70,000 $\mathrm{cm}^2/\mathrm{Vs}$. A 100-nm thick layer of Al_2O_3 separates the top gate from the depletion gates, which are arranged to define a DQD and a single-dot charge-sensor. The depletion gate pattern is scaled down by a factor

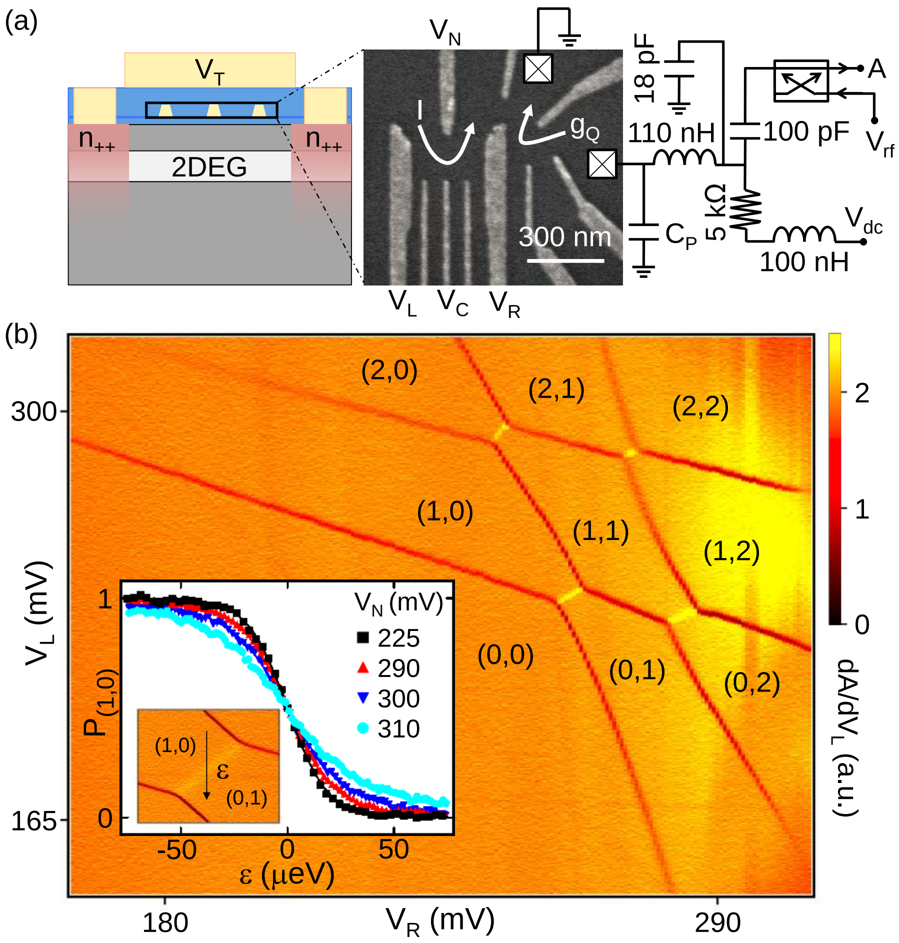

Figure 4.5: (a) The DQD is operated by biasing a global top gate at voltage V_T to accumulate carriers in the quantum well (left). Local depletion gates define the DQD confinement potential (center). Charge-sensing is performed using rf-reflectometry (right). (b) Few electron charge stability diagram visible in the derivative of the reflected rf amplitude dA/dV_L. (N_L, N_R) indicate the number of electrons in the left and right dots. (Inset) $P_{(1,0)}$ plotted as a function of detuning, for different values of V_N, showing tunable interdot tunnel coupling at the (1,0)–(0,1) interdot charge transition.

of ~ 2.5 compared to few electron GaAs DQDs to compensate for the larger effective mass of electrons in Si [30].

Compared to the depletion-mode devices, the electron beam gate pattern has also been further optimized to improve the charge sensing measurement. Instead of using a quantum point contact, a single quantum dot is used as a high sensitivity charge detector [46]. The single dot is coupled to a resonant circuit [Fig. 4.5(a)]

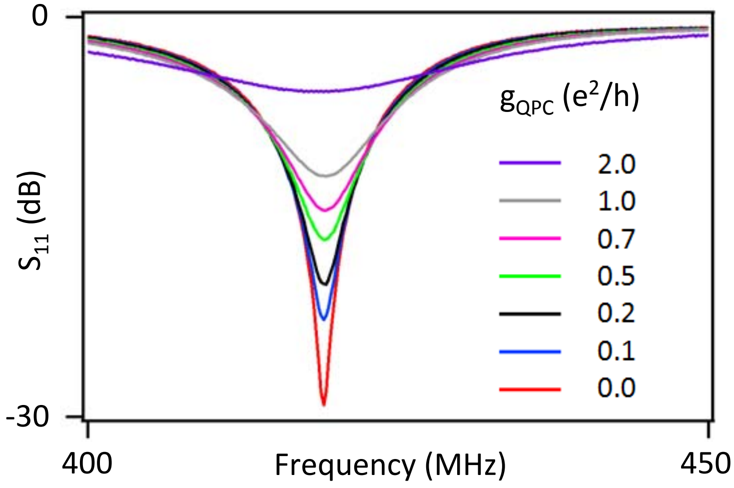

Figure 4.6: Measured reflection coefficient, S_{11}, at different charge-sensor conductances, with a device similar to the one discussed in this chapter. At the resonance frequency $f_\mathrm{r} =$ 418 MHz, the reflected signal amplitude depends strongly on the sensor conductance.

[37, 47, 48, 95, 96] that is driven near its resonance frequency $f_\mathrm{r} = 431.8$ MHz [Fig. 4.6]. The reflected amplitude A is a sensitive function of the conductance of the single dot sensor [Fig. 4.6], g_Q, which is modulated by charge transitions in the DQD. The complete RF circuit diagram can be found in Appendix B.

The single-dot sensor can be operated in different regimes depending on the specific needs of the experiment [Fig. 4.7(a)]. In general, the charge-sensing signal-to-noise ratio increases with the conductance slope (as a function of sensor gate voltage) at which the sensor is operated. By tuning the shape of the electron wave function at the dot sensor from a QPC channel to a well-defined single quantum dot, we can achieve three different operating regimes with different sensitivity. As shown in [Fig. 4.7], the signal-to-noise ratio is best when the sensor is tuned to the single dot regime. Therefore, we operate the sensor at this regime when we take charge relaxation and qubit manipulation data. Meanwhile, due to the increasing difficulty in QPC compensation in the single dot regime, the high quality sensing data can only be obtained

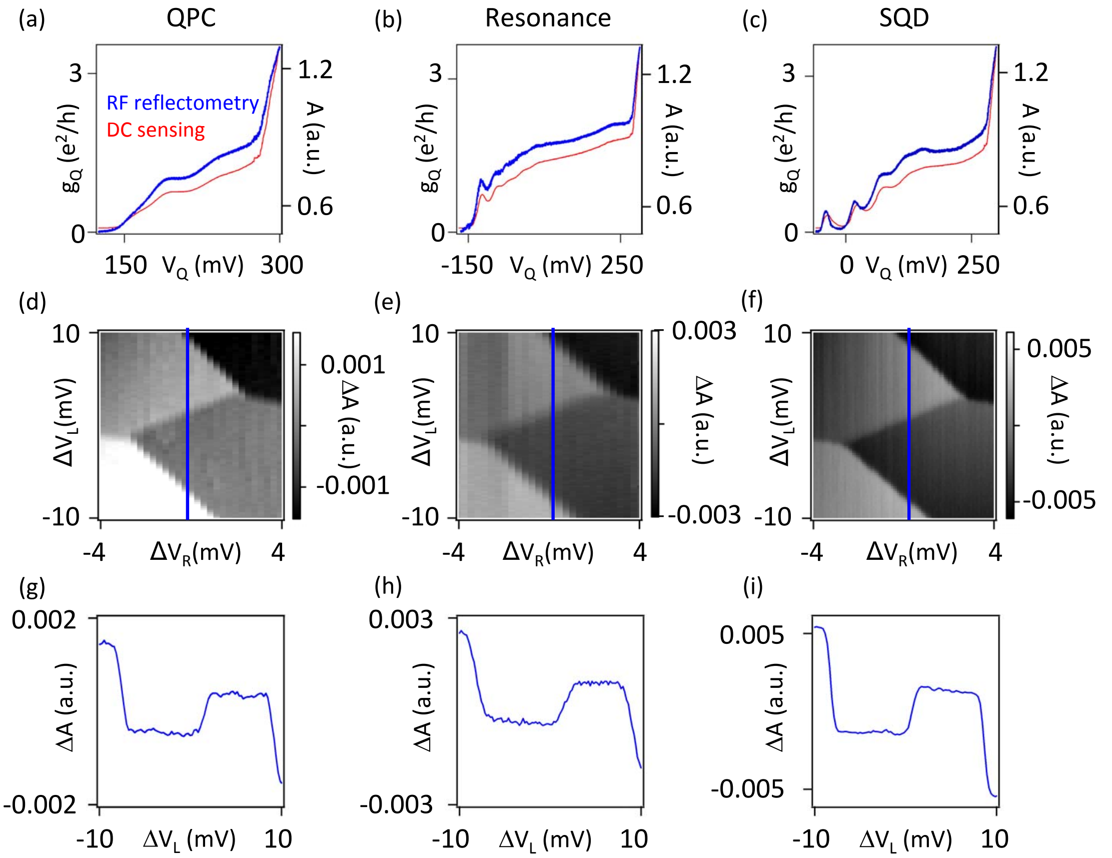

Figure 4.7: (a)–(c) Comparison of DC and RF sensing signals in different sensing regimes. The conductance slope becomes sharper as we move from the (a) QPC regime to the (c) SQD regime. (d)–(f) Comparison of raw sensing data in different sensing regimes at the same charge configuration. The quality of the data improves as the sensor is tuned towards the SQD regime. (g)–(i) 1D cut through the raw data, demonstrating increasing signal-to-noise ratio as the sensor is tuned to the SQD regime.

over a typical gate voltage range of 20 mV. For this reason, we operate the sensor as a QPC when we map out the large scale stability diagram. Therefore, in a device where both full range charge stability diagram and high quality zoomed in sensing data are important, the ability to continuously tune the sensor between different operation regimes is essential.

After optimizing the charge sensor, we demonstrate single-electron occupancy using radio frequency (RF) reflectometry [97]. We map out the DQD charge stability diagram in Fig. 4.5(b) by measuring dA/dV_{L} as a function of V_{L} and V_{R}. No charging transitions are observed in the lower left corner of the charge stability diagram, indicating that the DQD has been completely emptied of free electrons. We identify this charge configuration as (0,0), where (N_{L}, N_{R}) indicates the number of electrons in the left and right dots. We operate the device as a single-electron charge qubit near the (1,0)–(0,1) interdot charge transition. Charge dynamics are governed by the Hamiltonian $H = \frac{\varepsilon}{2}\sigma_{\mathrm{z}} + t_{\mathrm{c}}\sigma_{\mathrm{x}}$, where σ_{i} are the Pauli matrices. Tunable interdot tunnel coupling is necessary for quantum control since it sets charge qubit Larmor precession frequencies and the exchange energy in a singlet-triplet spin qubit [20, 30]. We demonstrate tunable interdot tunnel coupling in the single-electron regime by measuring the left dot occupation $P_{(1,0)}$ as a function of detuning [Fig. 4.5(b), inset]. Qubit occupation is described by

$$P_{(1,0)} = \frac{1}{2}\left[1 - \frac{\varepsilon}{\Omega}\tanh\left(\frac{\Omega}{2k_{\mathrm{B}}T_{\mathrm{e}}}\right)\right], \tag{4.1}$$

where k_{B} is Boltzmann's constant, $T_{\mathrm{e}} \sim 100$ mK is the electron temperature, and $\Omega = \sqrt{\varepsilon^2 + 4t_{\mathrm{c}}^2}$ is the qubit energy splitting [45]. With $V_{\mathrm{N}} = 225$ mV, the interdot charge transition is thermally broadened as $2t_{\mathrm{c}} < k_{\mathrm{B}}T_{\mathrm{e}}$. Increasing t_{c} by adjusting V_{N} leads to further broadening of the interdot transition. For $V_{\mathrm{N}} = 290$, 300 and 310 mV we extract $2t_{\mathrm{c}} = 3.8$, 5.9 and 9.0 GHz by fitting the data to Eq. 4.1. These results show that interdot tunnel coupling can be sensitively tuned in the single-electron regime despite the large effective mass of electrons in Si [98].

4.3 Excited State Spectroscopy

Transport measurements can be used to probe the energy level structure of the DQD [44]. In a few-electron GaAs DQD, orbital excited states are typically several meV higher in energy than the ground state [49]. We investigate the DQD energy level

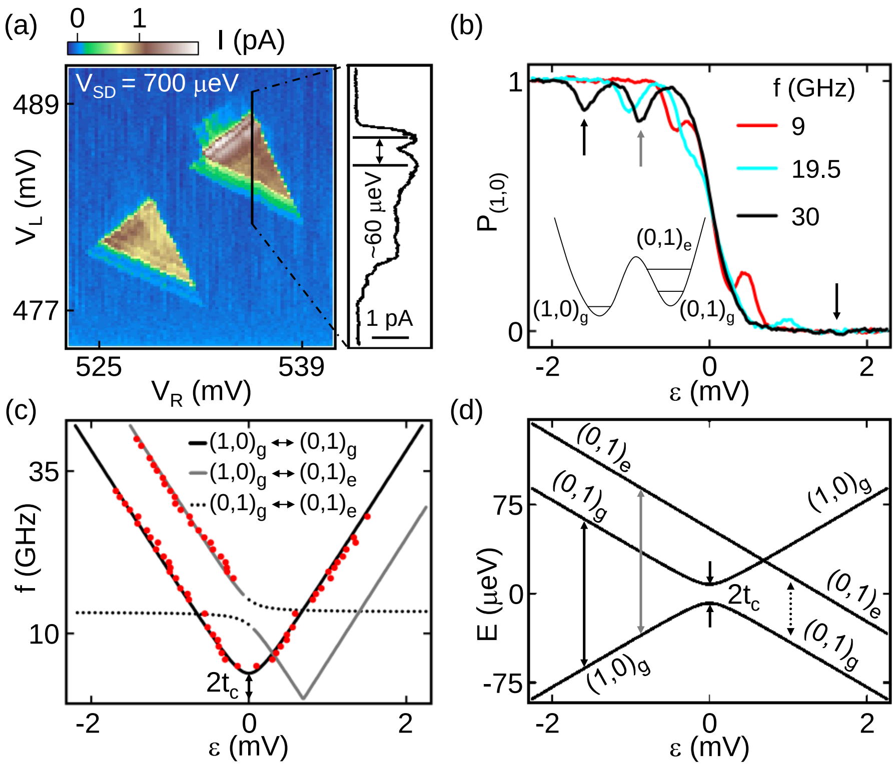

Figure 4.8: (a) (left) Current, I, measured as a function of V_{L} and V_{R} near the (1,0)–(0,1) charge transition. A cut through the finite bias triangle (right) indicates the presence of a low lying excited state. (b) $P_{(1,0)}$ plotted as a function of detuning ε for different excitation frequencies f. For $f \gtrsim 15$ GHz, a new PAT peak emerges (grey arrow) corresponding to the $(1,0)_{\mathrm{g}} \leftrightarrow (0,1)_{\mathrm{e}}$ transition. The appearance of this PAT peak is accompanied by the suppression of $(1,0)_{\mathrm{g}} \leftrightarrow (0,1)_{\mathrm{g}}$ PAT peak (black arrow) at positive detuning. (c) Transition frequencies as a function of detuning and (d) energy level diagram extracted from data in (c). The data in (c) are best fit with an interdot tunnel coupling $t_{\mathrm{c}} = 1.9$ GHz and an excited state energy $\Delta = 55$ μeV.

structure in Fig. 4.8(a), where we plot the current I as a function of V_{L} and V_{R} with a fixed source-drain bias $V_{\mathrm{SD}} = 700$ μeV. In contrast with GaAs devices, the current in the finite bias triangles is not a smooth function of gate voltage. In particular, we observe a small resonance ~ 60 μeV away from the interdot charge transition, suggesting the existence of a low-lying excited state in one of the dots.

We obtain higher energy resolution using microwave spectroscopy. Microwaves drive charge transitions (PAT spectroscopy) when the photon energy matches the qubit splitting, $hf = \Omega$, where f is the photon frequency and h is Planck's constant.

PAT transitions are directly observed as deviations from the ground state occupation in measurements of $P_{(1,0)}$ as a function of detuning [compare Fig. 4.8(b) and the inset to Fig. 4.5(b)]. For $f \lesssim 15$ GHz, the PAT peaks are symmetric around $\varepsilon = 0$ mV and shift to larger detuning with increasing photon energy, consistent with a simple two level interpretation [18, 38]. However, for $f \gtrsim 15$ GHz, an additional PAT peak emerges at negative detuning and is not accompanied by a PAT peak at positive detuning. Figure 4.8(c) shows the extracted transition frequencies as a function of detuning.

The data are fit using a three-level Hamiltonian that includes the left dot ground state $(1,0)_{\mathrm{g}}$, the right dot ground state $(0,1)_{\mathrm{g}}$, and a right dot excited state $(0,1)_{\mathrm{e}}$, as sketched in the inset of Fig. 4.8(b). The Hamiltonian can be written as

$$H = \begin{bmatrix} -\frac{\varepsilon}{2} & t_{\mathrm{c}} & t_{\mathrm{c1}} \\ t_{\mathrm{c}} & \frac{\varepsilon}{2} & i_{\mathrm{c}} \\ t_{\mathrm{c1}} & i_{\mathrm{c}} & \frac{\varepsilon}{2} + \Delta \end{bmatrix}, \tag{4.2}$$

in which ε is the detuning parameter, Δ is the excited state energy splitting, t_{c}, t_{c1} and i_{c} are the coupling terms between $(1,0)_{\mathrm{g}}$ and $(0,1)_{\mathrm{g}}$, $(1,0)_{\mathrm{g}}$ and $(0,1)_{\mathrm{e}}$, and between $(0,1)_{\mathrm{g}}$ and $(0,1)_{\mathrm{e}}$.

For the data shown in Fig. 4.8(c), the positions of the two main PAT peaks corresponding to $(1,0)_{\mathrm{g}} \leftrightarrow (0,1)_{\mathrm{g}}$ are symmetric about $\varepsilon = 0$ mV and contain no anti-crossing feature within the resolution of our measurements (~ 1 μeV). This is in agreement with t_{c1}, $i_{\mathrm{c1}} \ll t_{\mathrm{c}}$. In the following discussion, we will therefore assume t_{c1}, $i_{\mathrm{c1}} = 0$. The Hamiltonian then becomes

$$H = \begin{bmatrix} -\frac{\varepsilon}{2} & t_{\mathrm{c}} & 0 \\ t_{\mathrm{c}} & \frac{\varepsilon}{2} & 0 \\ 0 & 0 & \frac{\varepsilon}{2} + \Delta \end{bmatrix}, \tag{4.3}$$

which gives the eigenenergies

$$\begin{aligned} E_{1,2} &= \pm\frac{1}{2}\sqrt{\varepsilon^2 + 4t_{\mathrm{c}}^2} \\ E_3 &= \frac{\varepsilon}{2} + \Delta. \end{aligned} \tag{4.4}$$

PAT peaks are expected at resonant microwave frequencies

$$\begin{aligned} f_1 &= \left|\frac{\varepsilon}{2} + \Delta + \frac{1}{2}\sqrt{\varepsilon^2 + 4t_{\mathrm{c}}^2}\right| /h \\ f_2 &= \left|\frac{\varepsilon}{2} + \Delta - \frac{1}{2}\sqrt{\varepsilon^2 + 4t_{\mathrm{c}}^2}\right| /h \\ f_3 &= \sqrt{\varepsilon^2 + 4t_{\mathrm{c}}^2}/h. \end{aligned} \tag{4.5}$$

When $|\varepsilon| \gg t_c$, we have $f_1 \approx \Delta/h$ at negative ε and $f_2 \approx \Delta/h$ at positive ε. This corresponds to the intradot transition between $(0,1)_{\mathrm{g}}$ and $(0,1)_{\mathrm{e}}$. This transition does not involve net charge transfer from the left dot to the right dot and can therefore not be detected using charge sensing. As a result, no PAT peaks are visible at $f = \Delta/h$.

Using the expressions above, the fit to the data gives $t_c = 1.94$ GHz and $\Delta = 55$ μeV. These values are consistent with the charge sensing data shown in the inset of Fig. 4.5(b) and the dc transport data shown in Fig. 4.8(a). The energy eigenstates obtained from the model are plotted as a function of detuning in Fig. 4.8(d). We note that an excited state is observed in the left quantum dot in Device 2, with $\Delta = 64$ μeV [Fig. 4.9]. For both devices, the excited state energy is highly sensitive to V_{N} and V_{C}, suggesting that it is not purely orbital in origin [93].

In addition to the asymmetry of the excited state PAT peak position, we have observed two other notable features in our PAT spectroscopy data. First of all, the PAT peak for the $(1,0)_{\mathrm{g}} \leftrightarrow (0,1)_{\mathrm{e}}$ transition is absent at positive detuning. Second, the peak height of the $(1,0)_{\mathrm{g}} \leftrightarrow (0,1)_{\mathrm{e}}$ PAT peak can be suppressed at higher frequencies

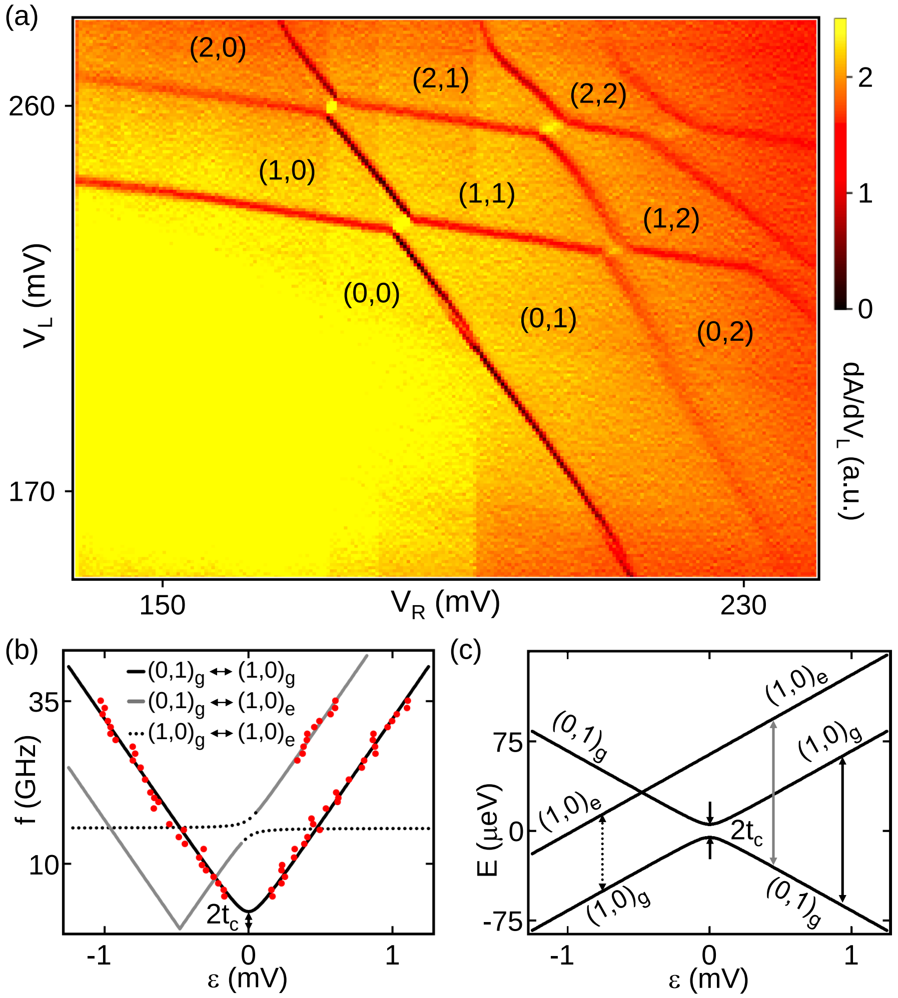

Figure 4.9: (a) Few electron stability diagram of device 2. (b) Qubit transition frequency as a function of detuning and (c) energy level diagram extracted from data in (b). The data in (b) are best fit with an interdot tunnel coupling $t_c = 1.3$ GHz and excited state energy of 64 μeV.

($f \gtrsim 15$ GHz) [Fig. 4.8(b)]. We note that both these features can be explained within our simple three-level model.

At negative detuning [Fig. 4.10(a)], $(1,0)_g$ is the ground state of the system and the coherent charge oscillations occur when the applied microwave frequency $f = \left(E_{(0,1)_e} - E_{(1,0)_g}\right)/h$ [Fig. 4.10(a)]. In contrast, $(0,1)_g$ becomes the new ground state at positive detuning [Fig. 4.10(b)]. As a result, the electron is trapped in $(0,1)_g$ as

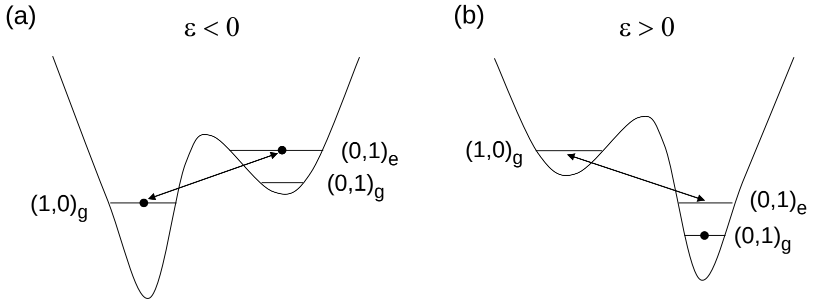

Figure 4.10: Sketch of the energy level diagram for the $(1,0)_\mathrm{g} \leftrightarrow (0,1)_\mathrm{e}$ PAT peak at (a) negative and (b) positive values of ε. The corresponding PAT peak is absent at negative ε due to the electron being trapped in $(0,1)_\mathrm{g}$.

we attempt to drive charge oscillations between $(1,0)_\mathrm{g}$ and $(0,1)_\mathrm{e}$, resulting in the suppression of the excited state PAT peak.

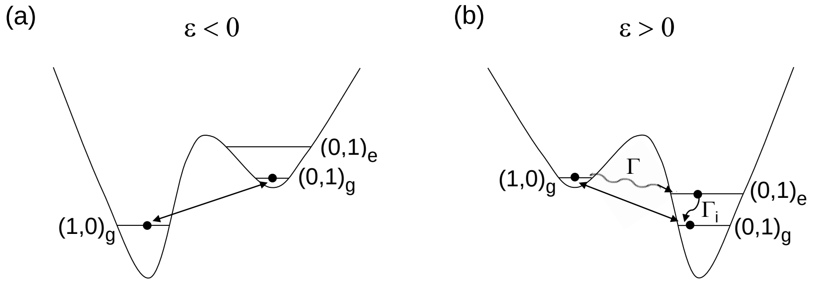

Figure 4.11: Sketch of the energy level diagram for the $(1,0)_\mathrm{g} \leftrightarrow (0,1)_\mathrm{g}$ PAT peak for $f \gtrsim 15$ GHz, at (a) negative and (b) positive values of ε. The PAT peak height at negative ε can be suppressed under certain conditions, due to the electron being partially trapped in $(0,1)_\mathrm{e}$.

Figure 4.11 shows the energy level diagram for the $(1,0)_\mathrm{g} \leftrightarrow (0,1)_\mathrm{e}$ transition at $f \gtrsim 15$ GHz. At negative detuning [Fig. 4.11(a)], $(0,1)_\mathrm{e}$ is the highest energy state and does not interfere with the coherently driven charge oscillation $(1,0)_\mathrm{g} \leftrightarrow (0,1)_\mathrm{e}$. However, at positive detuning [Fig. 4.11(b)], $(0,1)_\mathrm{e}$ lies between $(0,1)_\mathrm{g}$ and $(1,0)_\mathrm{g}$. Depending on the value of t_c and the energy deference between $(1,0)_\mathrm{g}$ and $(0,1)_\mathrm{e}$, the interdot transition rate Γ can be faster or comparable to the intradot relaxation rate Γ_i. Under such a condition, the $(1,0)_{\mathrm{g}}$ charge state can leak to $(0,1)_{\mathrm{e}}$ during the charge oscillation and result in the electron being partially trapped in $(0,1)_{\mathrm{e}}$. The PAT peak height will therefore decrease due to the reduced time averaged probability of the electron being in the $(1,0)_{\mathrm{g}}$ state.

Several additional features observed in the data are explained by the three-level model. The $(0,1)_{\mathrm{g}} \leftrightarrow (0,1)_{\mathrm{e}}$ intradot charge transition [dotted line, Fig. 4.8(c)] is not visible since the charge detector is only sensitive to interdot charge transitions. We also note that the $(0,1)_{\mathrm{e}} \leftrightarrow (1,0)_{\mathrm{g}}$ PAT peak is not visible at positive detuning. At low temperatures, the qubit population resides in the ground state $(0,1)_{\mathrm{g}}$, preventing microwave transitions from $(0,1)_{\mathrm{e}}$ to $(1,0)_{\mathrm{g}}$. Finally, the $(0,1)_{\mathrm{g}} \leftrightarrow (1,0)_{\mathrm{g}}$ PAT peak is suppressed when $\varepsilon > \Delta$ due to population trapping in $(0,1)_{\mathrm{e}}$.

4.4 Charge Relaxation Time T_1

The longer spin relaxation times measured in Si compared to GaAs are attributed to the absence of piezoelectric phonon coupling, along with a weaker spin-orbit interaction. Likewise, the absence of piezoelectric phonon coupling in Si is expected to result in longer charge relaxation times than in GaAs where $T_1 \sim 10$ ns [99]. We measure the interdot charge relaxation time T_1 by applying microwaves to V_{L} with a 50% duty cycle and varying the pulse period τ [Fig. 4.12(a)]. We focus on the $(1,0)_{\mathrm{g}}$ $\leftrightarrow (0,1)_{\mathrm{g}}$ transition at negative detuning, where the high energy state $(0,1)_{\mathrm{e}}$ is not populated. Simulations of $P_{(1,0)}$ as a function of time, t, for $\tau = 1$ μs are shown in Fig. 4.12(a) for three realistic values of T_1. During the first half of the pulse cycle, microwaves coherently drive the $(1,0)_{\mathrm{g}} \leftrightarrow (0,1)_{\mathrm{g}}$ charge transition, resulting in an average $P_{(1,0)} = 0.5$. The microwave excitation is then turned off, leading to charge relaxation during the second half of the pulse cycle, with $P_{(1,0)}$ approaching 1 on a timescale set by T_1.

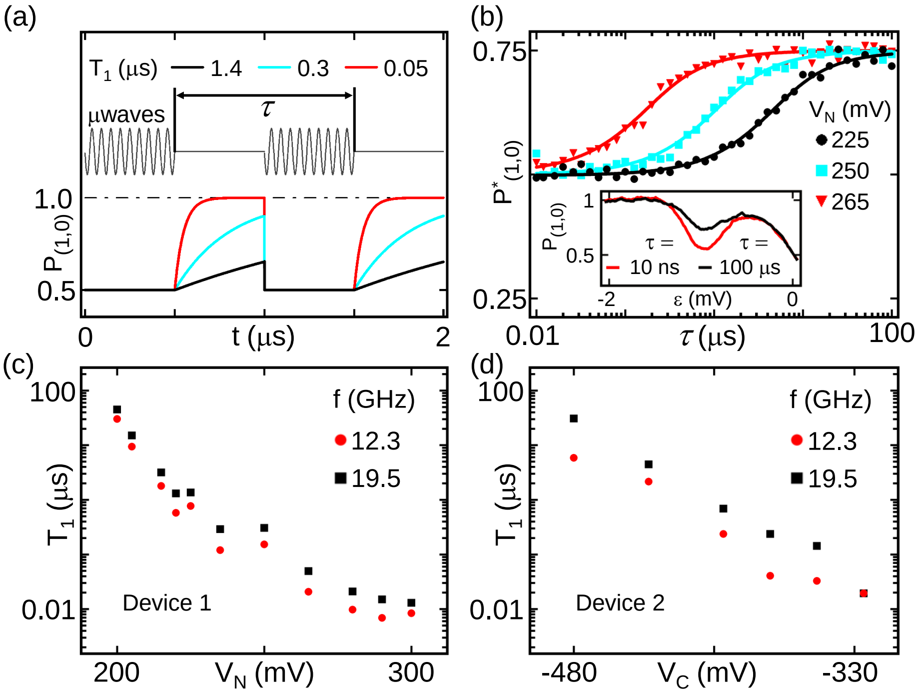

Figure 4.12: (a) Pulse sequence used to measure T_1 and simulated qubit response. $P_{(1,0)} = 0.5$ when resonant microwaves drive transitions between $(0,1)_{\rm g}$ and $(1,0)_{\rm g}$, and approaches 1 on a timescale set by T_1 when the microwaves are turned off. (b) $P^*_{(1,0)}$ as a function of τ extracted for different $V_{\rm N}$ at $f = 19.5$ GHz. Fits to the data give $T_1 = 1.4$ μs, 0.3 μs and 0.05 μs for $V_{\rm N} = 225$ mV, 250 mV and 265 mV. (Inset) Comparison of typical PAT peaks at different τ, with fixed $V_{\rm N} = 225$ mV and $f = 25.9$ GHz. (c) T_1 as a function of $V_{\rm N}$ in device 1. (d) T_1 as a function of $V_{\rm C}$ in device 2. In both devices, T_1 increases as the interdot barrier is made less transparent.

In the inset of Fig. 4.12(b), $P_{(1,0)}$ is measured as a function of detuning for $\tau = 10$ ns and $\tau = 100$ μs. As expected, the PAT peak is smaller for longer periods due to charge relaxation. Specifically, in the limit $\tau \ll T_1$, relaxation has no time to occur during the second half of the pulse cycle, leading to a time-averaged value of $P_{(1,0)}$ $= 0.5$. In contrast, in the limit $\tau \gg T_1$, relaxation happens quickly, leaving $P_{(1,0)} =$ 1 for the majority of the second half of the pulse cycle. Combined with $P_{(1,0)} = 0.5$ for the first half of the pulse cycle, a time-averaged value of $P_{(1,0)} = 0.75$ is expected. Due to experimental limitations, such as frequency dependent attenuation in the coax lines and finite pulse rise times at small τ, we are unable to drive the transitions to saturation for some device configurations. To extract T_1 we therefore fit the raw $P_{(1,0)}$

data as a function of τ to the form

$$P_{(1,0)} = P_{\max} + (P_{\min} - P_{\max})\,\frac{2T_1(1 - e^{-\tau/(2T_1)})}{\tau}, \tag{4.6}$$

where $P_{\max}$ and $P_{\min}$ account for the limited visibility of the PAT peaks [38]. Extracted T_1 values are insensitive to the rescaling of the data via $P_{\max}$ and $P_{\min}$.

The interdot charge relaxation rate is strongly dependent on the depletion gate voltages that tune the interdot tunnel coupling. This variation is directly visible in the data shown in Fig. 4.12(b) for V_{N} = 225 mV, 250 mV and 265 mV. To facilitate a direct comparison of the data, we plot the normalized electron occupation $P^{*}_{(1,0)}$ = 0.5 + 0.25 × $(P_{(1,0)} - P_{\min})/(P_{\max} - P_{\min})$, using the values of $P_{\min}$ and $P_{\max}$ extracted from fits to Eq. 4.6. In Fig. 4.12(c), we plot T_1 over a wide range of V_{N} for two different excitation frequencies. We see a longer characteristic relaxation time for larger interdot barrier heights. Notably, T_1 is tunable over four orders of magnitude with a maximum observed value of 45 μs. The same overall trend is observed in data from Device 2 [Fig. 4.12(d)] where the interdot tunnel coupling was tuned using V_{C}. Interdot tunnel coupling t_{c} is only measurable in charge sensing when $2t_{\mathrm{c}} > k_{\mathrm{B}}T_{\mathrm{e}}$ [45]. For Device 1 [see Fig. 4.12(c)] we obtain $2t_{\mathrm{c}}$ = 2.4, 3.8 and 5.9 GHz for V_{N} = 280, 290 and 300 mV and for Device 2 [see Fig. 4.12(d)] we obtain $2t_{\mathrm{c}}$ = 3.2 GHz for V_{C} = -325 mV.

4.5 Excited State Charge Relaxation Time

Another essential parameter for quantum control of charge and spin qubits is the detuning parameter, ε [30]. An understanding of its influence on the relaxation time is therefore important. The bottom panel of Fig. 4.13(a) shows T_1 as a function of $f \propto \varepsilon$ for the $(0,1)_{\mathrm{g}} \leftrightarrow (1,0)_{\mathrm{g}}$ transition. Data are taken at f = 12.3, 19.5, 25.9 and 30.0 GHz, as indicated by the arrows in the energy level diagram in the upper panel

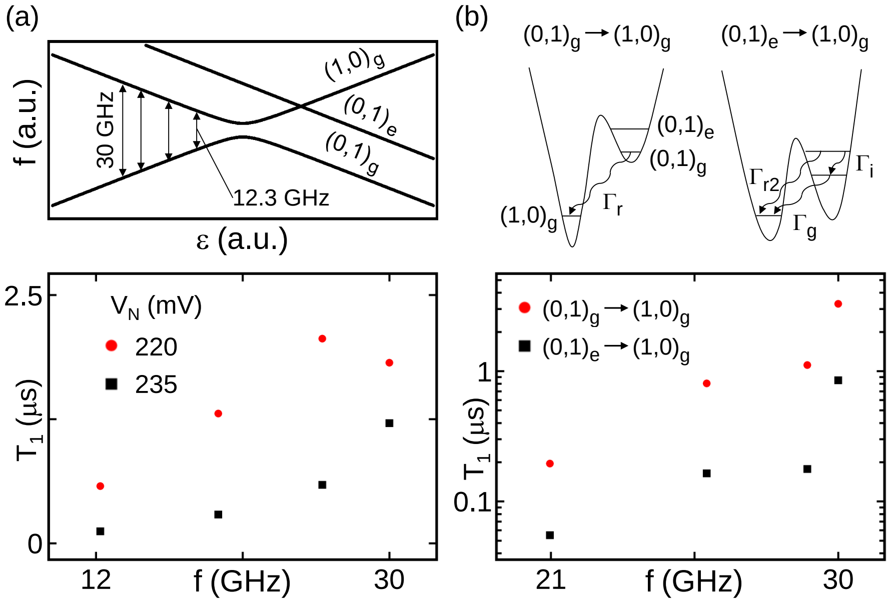

Figure 4.13: (a) T_1 increases weakly with f for the $(0,1)_{\mathrm{g}} \rightarrow (1,0)_{\mathrm{g}}$ transition (lower). Data are taken at the four values of f indicated by arrows in the energy level diagram (upper). (b) T_1 for the $(0,1)_{\mathrm{g}} \rightarrow (1,0)_{\mathrm{g}}$ and $(0,1)_{\mathrm{e}} \rightarrow (1,0)_{\mathrm{g}}$ transitions as a function of f with $V_{\mathrm{N}} = 250$ mV (lower). There are two $(0,1)_{\mathrm{e}} \rightarrow (1,0)_{\mathrm{g}}$ relaxation pathways (upper). Our measurements suggest a fast intradot relaxation rate.

of Fig. 4.13(a). To study the lifetime of the excited state, we also measure T_1 for both the $(0,1)_{\mathrm{g}} \rightarrow (1,0)_{\mathrm{g}}$ and the $(0,1)_{\mathrm{e}} \rightarrow (1,0)_{\mathrm{g}}$ relaxation processes at the same values of f [bottom panel of Fig. 4.13(b)]. Our data indicate that T_1 increases weakly as a function of detuning for the range of frequencies accessible in our cryostat, and that $(0,1)_{\mathrm{e}} \rightarrow (1,0)_{\mathrm{g}}$ relaxation is faster than $(0,1)_{\mathrm{g}} \rightarrow (1,0)_{\mathrm{g}}$ relaxation for the same energy splitting. This implies a fast intradot relaxation rate of the excited state. In contrast with the $(0,1)_{\mathrm{g}} \rightarrow (1,0)_{\mathrm{g}}$ relaxation process, $(0,1)_{\mathrm{e}}$ can relax via two distinct pathways [top panel of Fig. 4.13(b)]. The first relaxation process is a direct transition from $(0,1)_{\mathrm{e}} \rightarrow (1,0)_{\mathrm{g}}$ with a rate Γ_{r2}, while the second pathway proceeds via intradot charge relaxation to $(0,1)_{\mathrm{g}}$ with a rate Γ_{i} followed by an interdot transition to $(1,0)_{\mathrm{g}}$ with rate Γ_{g}. We have $\Gamma_{\mathrm{g}} > \Gamma_{\mathrm{r}}$ based on T_1's weakly increasing dependence on the detuning [Fig. 4.13(c)]. We also estimate $\Gamma_{\mathrm{r}} \geq \Gamma_{\mathrm{r2}}$ because the energy splitting is the same in both relaxation process and the initial and final states may have different valley components which could potentially suppresses the relaxation rate [94]. The much smaller excited state T_1 therefore implies that $(0,1)_{\mathrm{e}} \rightarrow (0,1)_{\mathrm{g}} \rightarrow (1,0)_{\mathrm{g}}$ is the dominant relaxation path due to a fast intradot relaxation rate [100]. Based on the measured T_1 at $f = 21$ GHz, we make a rough lower bound estimate on Γ_{i} of $\sim 1.5 \times 10^7\ s^{-1}$. This fast valley relaxation rate can be expected in realistic devices due to the interface-induced strong valley-orbit mixing [101].

4.6 Theory of Phonon-Mediated Charge Relaxation

To gain a better understanding of our data, we employ a phonon-mediated relaxation model from reference [99]. The electron-phonon coupling Hamiltonian in a Si quantum well takes the form of

$$H_{\mathrm{e-ph}} = i \sum_{\mathbf{Q},\lambda} \left(\frac{\hbar |\mathbf{Q}|}{2\rho V c_\lambda} \right)^{\frac{1}{2}} D^{\lambda}_{\mathbf{Q}} \left(a^{+}_{\mathbf{Q},\lambda} e^{i\mathbf{Q}\cdot\mathbf{r}} - a_{\mathbf{Q},\lambda} e^{-i\mathbf{Q}\cdot\mathbf{r}} \right), \tag{4.7}$$

where

$$D^{\lambda}_{\mathbf{Q}} = \left(\Xi_d \hat{\mathbf{e}}^{\lambda}_{\mathbf{Q}} \cdot \hat{\mathbf{Q}} + \Xi_u \hat{e}^{\lambda}_{\mathbf{Q},z} \hat{Q}_z \right). \tag{4.8}$$

Here $a_{\mathbf{Q},\lambda}$ ($a^{+}_{\mathbf{Q},\lambda}$) are the annihilation (creation) operators for phonons belonging to branch λ ($\lambda =$ TA1, TA2 for transverse phonons and $\lambda =$ LA for longitudinal phonons) with wave number $\mathbf{Q}$, and speed of sound in Si c_λ. V is the volume of the Si quantum well layer and ρ is the density of Si. Ξ_{u} and Ξ_{d} are the shear and dilation potential constants and $\hat{\mathbf{Q}}$ are the phonon unit wave vectors [99]. The phonon unit polarization vectors $\hat{\mathbf{e}}^{\lambda}_{\mathbf{Q}}$ are chosen in the following form

$$\begin{aligned}\hat{\mathbf{e}}_{\mathbf{Q}}^{LA} &= \hat{\mathbf{Q}} = \mathbf{Q}/|\mathbf{Q}| \\ \hat{\mathbf{e}}_{\mathbf{Q}}^{TA1} &= (Q_xQ_z, Q_yQ_z, -Q_\parallel^2)/QQ_\parallel \\ \hat{\mathbf{e}}_{\mathbf{Q}}^{TA2} &= (Q_y/Q_\parallel, -Q_x/Q_\parallel, 0),\end{aligned} \tag{4.9}$$

where $\mathbf{Q}_\parallel = (Q_x.Q_y, 0)$, $Q_\parallel = (Q_x^2 + Q_y^2)^{\frac{1}{2}}$.

In the regime of interest where $\varepsilon \gg t_c$, the initial and final states of the charge transition can be treated as non-hybridized $(0,1)_\mathrm{g}$ and $(1,0)_\mathrm{g}$ charge states. We assume Gaussian wavefunctions of the form,

$$|1,0\rangle_\mathrm{g} = (\frac{1}{\sqrt{\pi}a})(\frac{1}{\sqrt{\pi}b})^{\frac{1}{2}} e^{-\frac{(x+d)^2+y^2}{2a^2} - \frac{z^2}{2b^2}} \tag{4.10}$$

$$|0,1\rangle_\mathrm{g} = (\frac{1}{\sqrt{\pi}a})(\frac{1}{\sqrt{\pi}b})^{\frac{1}{2}} e^{-\frac{(x-d)^2+y^2}{2a^2} - \frac{z^2}{2b^2}}, \tag{4.11}$$

in which a is the dot radius, b is the vertical confinement and $2d$ is the separation of the two dots. All these values depend strongly on the voltages on the top gate and the depletion gates, as well as device specifics.

For the LA phonon, the electron-phonon coupling Hamiltonian takes the form

$$\begin{aligned}H_\mathrm{e-ph}^{LA} =& i\sum_{\mathbf{Q},\lambda} \left(\frac{\hbar|\mathbf{Q}|}{2\rho V c_\lambda}\right)^{\frac{1}{2}} \Xi_\mathrm{d} \left(1 + \frac{\Xi_\mathrm{u}}{\Xi_\mathrm{d}} \frac{Q_z^2}{|\mathbf{Q}|^2}\right) \\ & \times \left(a_{\mathbf{Q},\lambda}^+ e^{i\mathbf{Q}\cdot\mathbf{r}} - a_{\mathbf{Q},\lambda} e^{-i\mathbf{Q}\cdot\mathbf{r}}\right).\end{aligned} \tag{4.12}$$

The transition rate is given by Fermi's golden rule,

$$\begin{aligned}\Gamma_{LA} = 1/T_1 =& \frac{2\pi}{\hbar} \sum_{\mathbf{q}} |\langle 1,0|_\mathrm{g} H_\mathrm{e-ph}^{LA} |0,1\rangle_\mathrm{g}|^2 \delta(\hbar\omega_\mathbf{Q} - \Omega) \\ =& \frac{\pi \Xi_\mathrm{d}^2}{\rho V c_\mathrm{l}} \sum_{\mathbf{Q}} |\mathbf{Q}| \left(1 + \frac{\Xi_\mathrm{u}}{\Xi_\mathrm{d}} \frac{Q_z^2}{|\mathbf{Q}|^2}\right)^2 \\ & \times |\langle 1,0|_\mathrm{g} e^{i\mathbf{Q}\cdot\mathbf{r}} |0,1\rangle_\mathrm{g}|^2 \delta(\hbar\omega_\mathbf{Q} - \Omega),\end{aligned} \tag{4.13}$$

in which

$$\begin{aligned}
&|\langle 1,0|_{\mathrm{g}} e^{i\mathbf{Q}\cdot\mathbf{r}}|0,1\rangle_{\mathrm{g}}| \\
&=(\frac{1}{\sqrt{\pi}a})^2(\frac{1}{\sqrt{\pi}b})\iiint e^{-\frac{x^2+y^2+d^2}{a^2}-\frac{z^2}{b^2}}e^{i\mathbf{Q}\cdot\mathbf{r}}dxdydz, \\
&=e^{-\frac{d^2}{a^2}-\frac{1}{4}[a^2(Q_{\mathrm{x}}^2+Q_{\mathrm{y}}^2)+b^2Q_{\mathrm{z}}^2]}
\end{aligned} \tag{4.14}$$

therefore the transition rate is

$$\begin{aligned}
\Gamma_{LA}=&\frac{\pi\Xi_{\mathrm{d}}^2}{\rho V c_{\mathrm{l}}}e^{-\frac{2d^2}{a^2}}\sum_{\mathbf{Q}}|\mathbf{Q}|\left(1+\frac{\Xi_{\mathrm{u}}}{\Xi_{\mathrm{d}}}\frac{Q_z^2}{|\mathbf{Q}|^2}\right)^2 \\
&\times e^{-\frac{1}{2}[a^2(Q_{\mathrm{x}}^2+Q_{\mathrm{y}}^2)+b^2Q_{\mathrm{z}}^2]}\delta(\hbar\omega_{\mathbf{Q}}-\Omega) \\
=&\frac{\pi\Xi_{\mathrm{d}}^2}{\rho V c_{\mathrm{l}}}\frac{V}{(2\pi)^3}e^{-\frac{2d^2}{a^2}}\iiint|\mathbf{Q}|\left(1+\frac{\Xi_{\mathrm{u}}}{\Xi_{\mathrm{d}}}\frac{Q_z^2}{|\mathbf{Q}|^2}\right)^2 \\
&\times e^{-\frac{1}{2}[a^2(Q_{\mathrm{x}}^2+Q_{\mathrm{y}}^2)+b^2Q_{\mathrm{z}}^2]}\delta(\hbar c_{\mathrm{l}}|\mathbf{Q}|-\Omega)dQ_{\mathrm{x}}dQ_{\mathrm{y}}dQ_{\mathrm{z}} \\
=&\frac{\Xi_{\mathrm{d}}^2}{8\pi^2\rho c_{\mathrm{l}}}e^{-\frac{2d^2}{a^2}}\iiint|\mathbf{Q}|\left(1+\frac{\Xi_{\mathrm{u}}}{\Xi_{\mathrm{d}}}\frac{Q_z^2}{|\mathbf{Q}|^2}\right)^2 \\
&\times e^{-\frac{1}{2}a^2|\mathbf{Q}|^2}e^{-\frac{1}{2}(b^2-a^2)Q_{\mathrm{z}}^2}\delta(\hbar c_{\mathrm{l}}|\mathbf{Q}|-\Omega)|\mathbf{Q}|^2\sin\theta \\
&d|\mathbf{Q}|d\theta d\phi \\
=&\frac{\Xi_{\mathrm{d}}^2}{4\pi\rho c_{\mathrm{l}}}\frac{\Omega^3}{(\hbar c_{\mathrm{l}})^4}e^{-\frac{2d^2}{a^2}}e^{-\frac{1}{2}\left(\frac{a\Omega}{\hbar c_{\mathrm{l}}}\right)^2} \\
&\int\left(1+\frac{\Xi_{\mathrm{u}}}{\Xi_{\mathrm{d}}}\cos^2\theta\right)^2e^{-\frac{1}{2}(b^2-a^2)\left(\frac{\Omega}{\hbar c_{\mathrm{l}}}\right)^2\cos^2\theta} \\
&\sin\theta d\theta.
\end{aligned} \tag{4.15}$$

For the TA phonon, the electron-phonon coupling Hamiltonian takes the form

$$\begin{aligned}
H_{\mathrm{e-ph}}^{TA}=&i\sum_{\mathbf{Q},\lambda}\left(\frac{\hbar|\mathbf{Q}|}{2\rho V c_\lambda}\right)^{\frac{1}{2}}\left(-\Xi_{\mathrm{u}}\frac{Q_zQ_\parallel}{|\mathbf{Q}|^2}\right) \\
&\times\left(a_{\mathbf{Q},\lambda}^+e^{i\mathbf{Q}\cdot\mathbf{r}}-a_{\mathbf{Q},\lambda}e^{-i\mathbf{Q}\cdot\mathbf{r}}\right),
\end{aligned} \tag{4.16}$$

therefore the transition rate is

$$
\begin{aligned}
\Gamma_{TA} =& \frac{\pi \Xi_{\mathrm{u}}^2}{\rho V c_{\mathrm{t}}} e^{-\frac{2d^2}{a^2}} \sum_{\mathbf{Q}} |\mathbf{Q}| \left(\frac{Q_z Q_{\parallel}}{|\mathbf{Q}|^2} \right)^2 \\
& \times e^{-\frac{1}{2}[a^2(Q_{\mathrm{x}}^2+Q_{\mathrm{y}}^2)+b^2 Q_{\mathrm{z}}^2]} \delta(\hbar\omega_{\mathbf{Q}} - \Omega) \\
=& \frac{\pi \Xi_{\mathrm{u}}^2}{\rho V c_{\mathrm{t}}} \frac{V}{(2\pi)^3} e^{-\frac{2d^2}{a^2}} \iiint |\mathbf{Q}| \left(\frac{Q_z Q_{\parallel}}{|\mathbf{Q}|^2} \right)^2 \\
& \times e^{-\frac{1}{2}[a^2(Q_{\mathrm{x}}^2+Q_{\mathrm{y}}^2)+b^2 Q_{\mathrm{z}}^2]} \delta(\hbar c_{\mathrm{t}} |\mathbf{Q}| - \Omega) dQ_{\mathrm{x}} dQ_{\mathrm{y}} dQ_{\mathrm{z}} \\
=& \frac{\Xi_{\mathrm{u}}^2}{8\pi^2 \rho c_{\mathrm{t}}} e^{-\frac{2d^2}{a^2}} \iiint |\mathbf{Q}| \left(\frac{Q_z Q_{\parallel}}{|\mathbf{Q}|^2} \right)^2 \\
& \times e^{-\frac{1}{2} a^2 |\mathbf{Q}|^2} e^{-\frac{1}{2}(b^2-a^2) Q_{\mathrm{z}}^2} \delta(\hbar c_{\mathrm{t}} |\mathbf{Q}| - \Omega) |\mathbf{Q}|^2 \sin\theta \\
& d|\mathbf{Q}| d\theta d\phi \\
=& \frac{\Xi_{\mathrm{u}}^2}{4\pi \rho c_{\mathrm{t}}} \frac{\Omega^3}{(\hbar c_{\mathrm{t}})^4} e^{-\frac{2d^2}{a^2}} e^{-\frac{1}{2}\left(\frac{a\Omega}{\hbar c_{\mathrm{t}}}\right)^2} \\
& \int e^{-\frac{1}{2}(b^2-a^2)\left(\frac{\Omega}{\hbar c_{\mathrm{t}}}\right)^2 \cos^2\theta} \sin^3\theta \cos^2\theta d\theta.
\end{aligned}
\tag{4.17}
$$

The total charge relaxation rate is given by $1/T_1 = \Gamma_{TA} + \Gamma_{LA}$.

An important result is that T_1 scales with $e^{\frac{2d^2}{a^2}}$. When V_{N} is swept from 300 mV to 200 mV in device 1, the tunnel barrier becomes less transparent as $2d$ increases when the dots move further apart (and at the same time, dot a decreases). We note that T_1 is extremely sensitive to a and d [Fig. 4.14], which depend strongly on device specifics. As a result, a quantitative estimation of T_1 requires a precise understanding of the heterostructure profile, actual device gate pattern layout and details of the confinement potential. This is beyond the scope of the discussion presented here. We will focus on a scaling law for T_1 in the remainder of this section.

To understand how T_1 scales with V_{N} (or V_{C}) in the far-detuned regime, we present a simple theory on the the effect of V_{N} and V_{C} on the confinement potential and the dot separation. We assume an interdot barrier potential $V_{\mathrm{b}} = V_0 e^{-\frac{x^2}{w^2}}$, where V_0 depends linearly on the gate voltage V_{N} (or V_{C}). In the limit $V_0 = 0$, the confinement potential

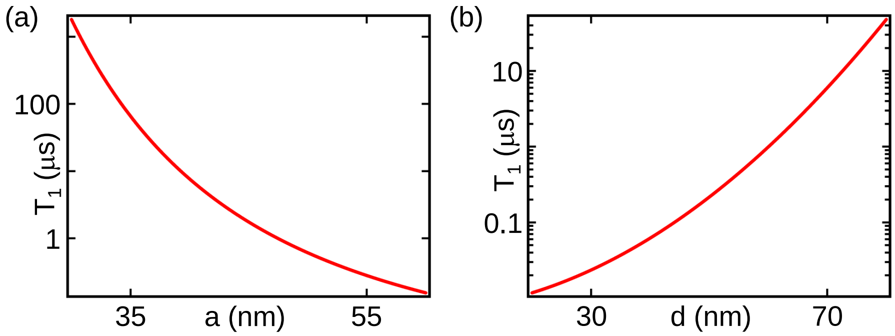

Figure 4.14: Simulated T_1 (a) as a function of a, at $d = 75$ nm and (b) as a function of d, at $a = 38$ nm. T_1 changes by orders of magnitude with a small change in a or d.

is assumed to be harmonic, $V_{\text{conf}} = \frac{1}{2}m\omega^2x^2$. In the presence of a finite interdot barrier, $V_{\text{conf}} = \frac{1}{2}m\omega^2x^2 + V_0e^{-\frac{x^2}{w^2}}$ forms a double well potential, with minima at $x = -d$ and $x = d$ by definition.

We Taylor-expand the barrier potential near $x = d$, which gives

$$\begin{aligned} V_{\text{conf}}|_{x\to d} &\approx \frac{1}{2}m\omega^2x^2 + (x-d)\left(\frac{dV_b}{dx}\right)_{x\to d} \\ &= \frac{1}{2}m\omega^2x^2 - V_0\frac{2d}{w^2}e^{-\frac{d^2}{w^2}}(x-d) \\ &= \frac{1}{2}m\omega^2\left(x - \frac{2dV_0}{mw^2\omega^2}e^{-\frac{d^2}{w^2}}\right)^2 - C \end{aligned} \tag{4.18}$$

in which C is a constant independent of x.

By definition of d, we have

$$\begin{aligned} d &= \frac{2dV_0}{mw^2\omega^2}e^{-\frac{d^2}{w^2}} \\ \Rightarrow d^2 &= w^2lnV_0 + C_1 \end{aligned} \tag{4.19}$$

in which C_1 is a constant independent of V_0. Combined with the previously obtained result $T_1 \propto e^{\frac{2d^2}{a^2}}$, we therefore have $T_1 \propto V_0^{\frac{w^2}{a^2}}$.

For device 1 where T_1 is tuned by V_{N}, we therefore have $T_1 \propto (V_{\mathrm{N0}} - V_{\mathrm{N}})^{\frac{w^2}{a^2}}$, in which V_{N0} is a constant offset. Similarly, we expect $T_1 \propto (V_{\mathrm{C0}} - V_{\mathrm{C}})^{\frac{w^2}{a^2}}$ for T_1 data extracted from device 2 [Fig. 4.12(d)]. The best power law fit to the T_1 data gives $w/a \sim 2.7$ for device 1 and $w/a \sim 2.3$ for device 2.

We note that in our simplified model, both w and a are treated as independent of V_{N} (or V_{C}). In reality, w increases and a decreases gradually as V_{N} (or V_{C}) is swept to more negative values, resulting in the deviation from the power law dependence. This is in agreement with our observations, in which T_1 has increased with a slightly faster power law at more negative gate values. A more quantitative theory of T_1 would require a complete understanding of the device specifics and the details of a realistic confinement potential.

Now let us turn to the zero detuning limit ($\varepsilon = 0$), in this case, the initial and final states are the fully hybridized bonding and anti-bonding states given by

$$|+\rangle = \frac{1}{\sqrt{2}}(|1,0\rangle_{\mathrm{g}} + |0,1\rangle_{\mathrm{g}}), \tag{4.20}$$

$$|-\rangle = \frac{1}{\sqrt{2}}(|1,0\rangle_{\mathrm{g}} - |0,1\rangle_{\mathrm{g}}). \tag{4.21}$$

The relaxation rate is given similarly to Eq. 4.13,

$$\begin{aligned}\Gamma_{LA} =& \frac{\pi \Xi_{\mathrm{d}}^2}{\rho V c_{\mathrm{l}}} \sum_{\mathbf{Q}} |\mathbf{Q}| \left(1 + \frac{\Xi_{\mathrm{u}}}{\Xi_{\mathrm{d}}} \frac{Q_z^2}{|\mathbf{Q}|^2}\right)^2 \\ & \times |\langle + | e^{i\mathbf{Q}\cdot\mathbf{r}} | - \rangle|^2 \delta(\hbar\omega_{\mathbf{Q}} - \Omega),\end{aligned} \tag{4.22}$$

in which

$$\begin{aligned}&|\langle + | e^{i\mathbf{Q}\cdot\mathbf{r}} | - \rangle| \\ &= \frac{1}{2}(|\langle 1,0|_{\mathrm{g}} e^{i\mathbf{Q}\cdot\mathbf{r}} |1,0\rangle_{\mathrm{g}} - \langle 0,1|_{\mathrm{g}} e^{i\mathbf{Q}\cdot\mathbf{r}} |0,1\rangle_{\mathrm{g}}|),\end{aligned} \tag{4.23}$$

where

$$\begin{aligned}
&\langle 1,0|_{\mathrm{g}} e^{i\mathbf{Q}\cdot\mathbf{r}} |1,0\rangle_{\mathrm{g}} \\
&= (\frac{1}{\sqrt{\pi}a})^2 (\frac{1}{\sqrt{\pi}b}) \iiint e^{-\frac{(x+d)^2+y^2}{a^2}-\frac{z^2}{b^2}} e^{i\mathbf{Q}\cdot\mathbf{r}} dxdydz \\
&= (\frac{1}{\sqrt{\pi}a}) e^{-\frac{1}{4}[a^2Q_{\mathrm{x}}^2+b^2Q_{\mathrm{z}}^2]} \int e^{-\frac{(x+d-i\frac{a^2}{2}Q_x)^2}{a^2}-\frac{d^2}{a^2}} e^{\frac{(d-i\frac{a^2}{2}Q_x)^2}{a^2}} dx \\
&= e^{-iQ_xd} e^{-\frac{1}{4}[a^2(Q_{\mathrm{x}}^2+Q_{\mathrm{y}}^2)+b^2Q_{\mathrm{z}}^2]}.
\end{aligned} \tag{4.24}$$

Note that instead of the $e^{-\frac{d^2}{a^2}}$ prefactor we have in the far-detuned regime (which corresponds to envelope decay as a function of d), the prefactor we have near $\varepsilon = 0$ is e^{-iQ_xd} (which corresponds to oscillating behavior as a function of d). Similarly, we have

$$\begin{aligned}
&\langle 0,1|_{\mathrm{g}} e^{i\mathbf{Q}\cdot\mathbf{r}} |0,1\rangle_{\mathrm{g}} \\
&= e^{iQ_xd} e^{-\frac{1}{4}[a^2(Q_{\mathrm{x}}^2+Q_{\mathrm{y}}^2)+b^2Q_{\mathrm{z}}^2]},
\end{aligned} \tag{4.25}$$

therefore we have

$$\begin{aligned}
&|\langle + | e^{i\mathbf{Q}\cdot\mathbf{r}} | - \rangle| \\
&= \frac{1}{2}(|\langle 1,0|_{\mathrm{g}} e^{i\mathbf{Q}\cdot\mathbf{r}} |1,0\rangle_{\mathrm{g}} - \langle 0,1|_{\mathrm{g}} e^{i\mathbf{Q}\cdot\mathbf{r}} |0,1\rangle_{\mathrm{g}}|) \\
&= \sin(Q_xd) e^{-\frac{1}{4}[a^2(Q_{\mathrm{x}}^2+Q_{\mathrm{y}}^2)+b^2Q_{\mathrm{z}}^2]}.
\end{aligned} \tag{4.26}$$

The relaxation rate in the zero detuning limit can then be written as

$$
\begin{aligned}
\Gamma_{LA} =& \frac{\pi \Xi_{\mathrm{d}}^2}{\rho V c_{\mathrm{l}}} \sum_{\mathbf{Q}} |\mathbf{Q}| \left(1 + \frac{\Xi_{\mathrm{u}}}{\Xi_{\mathrm{d}}} \frac{Q_z^2}{|\mathbf{Q}|^2}\right)^2 \\
& \times \sin^2(Q_x d) e^{-\frac{1}{2}[a^2(Q_{\mathrm{x}}^2+Q_{\mathrm{y}}^2)+b^2 Q_{\mathrm{z}}^2]} \delta(\hbar\omega_{\mathbf{Q}} - \Omega) \\
=& \frac{\pi \Xi_{\mathrm{d}}^2}{\rho V c_{\mathrm{l}}} \frac{V}{(2\pi)^3} \iiint |\mathbf{Q}| \left(1 + \frac{\Xi_{\mathrm{u}}}{\Xi_{\mathrm{d}}} \frac{Q_z^2}{|\mathbf{Q}|^2}\right)^2 \\
& \times \sin^2(Q_x d) e^{-\frac{1}{2}[a^2(Q_{\mathrm{x}}^2+Q_{\mathrm{y}}^2)+b^2 Q_{\mathrm{z}}^2]} \delta(\hbar c_{\mathrm{l}} |\mathbf{Q}| - \Omega) dQ_{\mathrm{x}} dQ_{\mathrm{y}} dQ_{\mathrm{z}} \\
=& \frac{\Xi_{\mathrm{d}}^2}{8\pi^2 \rho c_{\mathrm{l}}} \iiint |\mathbf{Q}| \left(1 + \frac{\Xi_{\mathrm{u}}}{\Xi_{\mathrm{d}}} \frac{Q_z^2}{|\mathbf{Q}|^2}\right)^2 \\
& \times \sin^2(Q_x d) e^{-\frac{1}{2}a^2|\mathbf{Q}|^2} e^{-\frac{1}{2}(b^2-a^2)Q_z^2} \delta(\hbar c_{\mathrm{l}} |\mathbf{Q}| - \Omega) |\mathbf{Q}|^2 \sin\theta \\
& d|\mathbf{Q}| d\theta d\phi \\
=& \frac{\Xi_{\mathrm{d}}^2}{8\pi^2 \rho c_{\mathrm{l}}} \frac{\Omega^3}{(\hbar c_{\mathrm{l}})^4} e^{-\frac{1}{2}\left(\frac{a\Omega}{\hbar c_{\mathrm{l}}}\right)^2} \\
& \iint \sin^2\left(\frac{\Omega d \sin\theta \cos\phi}{\hbar c_{\mathrm{l}}}\right) \left(1 + \frac{\Xi_{\mathrm{u}}}{\Xi_{\mathrm{d}}} \cos^2\theta\right)^2 \\
& \times e^{-\frac{1}{2}(b^2-a^2)\left(\frac{\Omega}{\hbar c_{\mathrm{l}}}\right)^2 \cos^2\theta} \sin\theta d\theta d\phi,
\end{aligned}
\tag{4.27}
$$

since $\frac{\Omega}{\hbar c_{\mathrm{l}}} \ll 1$, we have $\sin\left(\frac{\Omega d \sin\theta\cos\phi}{\hbar c_{\mathrm{l}}}\right) = \frac{\Omega d \sin\theta\cos\phi}{\hbar c_{\mathrm{l}}}$, which is equivalent to the dipole approximation made in [94]. We then have

$$
\begin{aligned}
1/T_1 =& \frac{\Xi_{\mathrm{d}}^2 d^2}{8\pi \rho c_{\mathrm{l}}} \frac{\Omega^5}{(\hbar c_{\mathrm{l}})^6} e^{-\frac{1}{2}\left(\frac{a\Omega}{\hbar c_{\mathrm{l}}}\right)^2} \\
& \int \left(1 + \frac{\Xi_{\mathrm{u}}}{\Xi_{\mathrm{d}}} \cos^2\theta\right)^2 \\
& \times e^{-\frac{1}{2}(b^2-a^2)\left(\frac{\Omega}{\hbar c_{\mathrm{l}}}\right)^2 \cos^2\theta} \sin^3\theta d\theta,
\end{aligned}
\tag{4.28}
$$

Note that $\Gamma_{LA} \propto \Omega^5$ (similarly, we also have $\Gamma_{TA} \propto \Omega^5$) comes from the intradot integration of the electron operator. At zero detuning, the interdot integration component cancels out and the integration contains purely intradot components which gives Ω^5, consistent with the result found in reference [94] where the intradot relaxation is discussed. In the far-detuned regime, the integration of the electron operator contains purely interdot components which gives an Ω^3 dependence, the "missing" Ω^2 is replaced by decay prefactor $e^{\frac{-2d^2}{a^2}}$ which gives rise to the strong t_c dependence of T_1 observed in our data. Our experiment is carried out in the far-detuned regime, therefore only the results from Eq. 4.15 and Eq. 4.17 are used to generate the simulation plots shown in [Fig. 4.14].

4.7 Summary

We have developed a reliable fabrication recipe for dual gate DQD devices, based on the undoped heterostructures. The accumulated 2DEG is stable and absent of the switching noises previously encountered in the doped devices. With the improved electron beam gate design, we are able to reproducibly empty the devices with electrons and consistently form few electron qubits. We have enhanced our charge sensing capability by implementing a SQD sensor design and RF reflectometry setup.

We have measured charge relaxation times in a single electron Si/SiGe DQD, demonstrating a four order of magnitude variation in T_1 with gate voltage. Energy level spectroscopy indicates the presence of a low-lying excited state. From the estimated dot radius $a \sim 38$ nm, we expect orbital level spacings on the order of 1 meV, a factor of 18 larger than the value obtained from PAT spectroscopy ($\Delta = 55$ μeV). This suggests that the low-lying excited state is a valley-orbit mixed state. Since spin state preparation and readout rely on large excited state energies, a more detailed understanding of the low-lying energy states will be beneficial to the development of Si spin qubits [10].

We are unable to observe spin-blockade at the two electron transitions in all of the dual gate devices ($\sim$ 10 devices) we have measured at the base temperature. We attribute this to the valley splitting in our device being too small, due to the valley orbit coupling and the presence of lattice steps in the active device region. A new device design with potentially more localized and uniform electron wavefunction, is therefore proposed to enhance the valley splitting. In the next chapter, we will discuss the design and initial development of these accumulation-only devices.

Chapter 5

Accumulation-Only Mode Si Quantum Dots

In the previous chapter, we successfully formed a high quality single-electron charge qubit, measured the energy level structure, and systematically measured its charge relaxation time T_1. We then attempted to form a singlet-triplet qubit. To look for signs of spin blockade, we have systematically examined the two-electron transitions in both transport and pulsed charge-sensing measurements. We measured finite bias triangles at negative and positive source-drain bias as shown in Figure 5.1. In contrast with GaAs DQD devices, the region of strong current suppression at negative bias (spin blockade region) was not observed [Fig. 5.1(a)].

To confirm the absence of Pauli blockade, we also performed pulse-gate experiments. A series of pulses was applied to V_L and V_R, as shown in Figure 5.1(c). The double dot was cycled through three configurations, while the charge-sensing measurement is performed [Figure 5.1(c)]. The DQD is pulsed to (0,1) in the "empty" (E) step (10% of the pulse period), and a new electron is added to the left dot in the subsequent "reset" (R) step (10% of the pulse period), resulting into (1,1) charge state with a mixture of four possible spin configurations (singlet S, triplets T_-, T_0

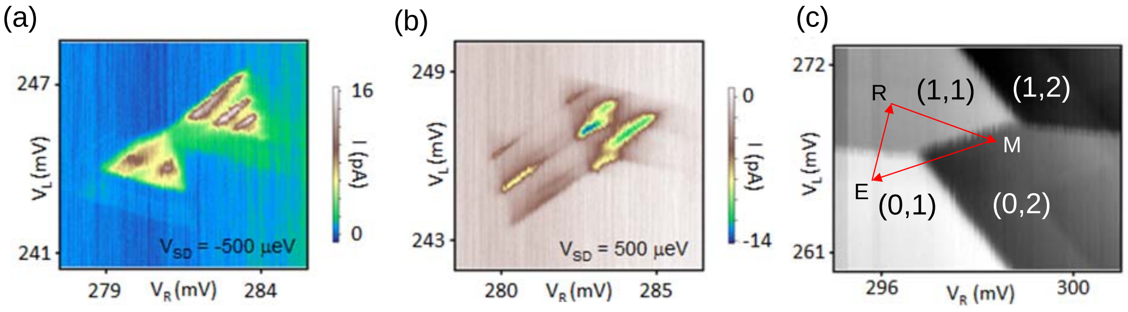

Figure 5.1: The finite bias triangles measured in current, I, at the (1,1) - (0,2) charge transition, with a 50 mT in-plane external magnetic field and a (a) negative and (b) positive source-drain bias voltages applied to a dual-gated DQD device. (c) Pulse-gate charge sensing data. No sign of spin blockade has been observed in either type of data.

and T_+). In the "measurement" (M) step (80% of the pulse period), (1,1)S is pulsed to (0,2)S while the spin triplet states remains in the (1,1) charge configuration due to spin blockade. In contrast with GaAs DQDs [31, 63], the spin-blockaded region (with some portion of (1,1) in the (0,2) region in the stability diagram) was not observed [Fig. 5.1(c)].

We performed similar experiments on more than ten DQD devices, but didn't observe signs of spin blockade in any of the devices. One possible explanation for the lack of spin blockade is a small valley splitting. The valley splitting has so far presented the biggest challenge in the field of Si quantum computing. It prevents us from establishing spin qubits and motivates us to develop a new type of DQD device that will potentially enhance the valley splitting. In this chapter, we introduce valley physics in Si QDs. We show that a tighter and more uniform electron wavefunction is desirable to maximize the valley splitting in DQD devices. Following this logic, we have designed several new DQD device geometries and have obtained some initial transport data.

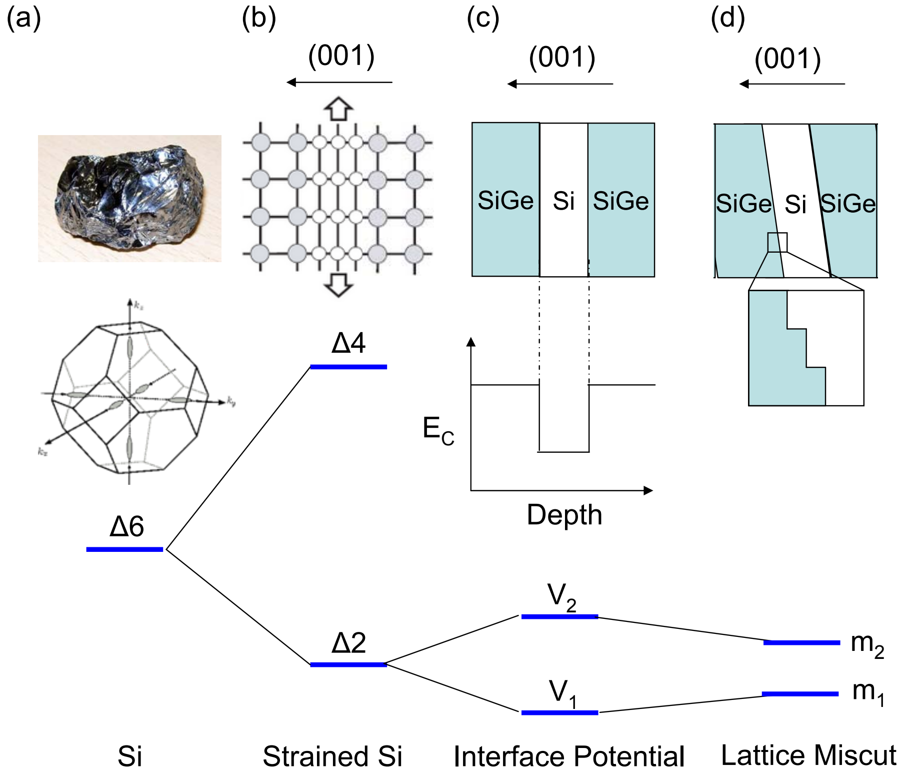

Figure 5.2: (a) The six-fold valley degeneracy in Si (pictures adapted from Wikipedia). (b) Due to lattice mismatch induced strain in the Si quantum well, the six-fold degeneracy is partially lifted. The resulting ground state is two-fold degenerate. (c) Due to the presence of a sharp interface potential in the Si/SiGe heterostructure, the remaining two-fold degeneracy is fully lifted, achieving the maximum valley splitting. (d) The presence of a lattice miscut creates a tilt angle between the heterostructure growth axis and the (001) lattice direction. This results in valley-orbit coupling that suppresses the valley splitting.

5.1 Valley Splitting in Silicon Quantum Dots

In contrast to GaAs, the Si conduction band has a six-fold valley degeneracy [81]. The positions of the conduction band minima are found along the six [100] directions near the X points in the Brillouin zone, specifically at $\mathbf{k}$ = [k_0, 0, 0], [-k_0, 0, 0], [0, k_0, 0], [0, -k_0, 0], [0, 0, k_0] and [0, 0, -k_0], where $k_0 \sim 0.85 \frac{2\pi}{a_0}$ [Fig. 5.2(a)]. Ideally this six-fold degeneracy would be fully lifted, resulting in a single ground state valley that is isolated in energy from other valley states.

In a GaAs/AlGaAs heterostructure, the lattice constant is 5.65325 $\AA$ for GaAs and 5.6533+0.0078x $\AA$ for $\mathrm{Al}_x\mathrm{Ga}_{1-x}\mathrm{As}$. Therefore, even for x=1, the lattice mismatch is as small as 0.14%. However, in a Si/SiGe heterostructure, the lattice constant is 5.431 $\AA$ for Si and 5.431 + 0.20x + 0.027x^2 $\AA$ for $\mathrm{Si}_{1-x}\mathrm{Ge}_x$. For the $\mathrm{Si}_{0.7}\mathrm{Ge}_{0.3}$/Si heterostructures used in this thesis, this gives a lattice mismatch as large as $\sim$ 1.15%. As a result, the thin Si quantum well that has been grown on the relaxed SiGe buffer is uniaxially strained in the x-y plane in order to match the lattice constant of SiGe. This uniaxial strain breaks the symmetries of the six valleys into two groups [Fig. 5.2(b)], the four-fold degenerate valley excited states Δ_4 ($\mathbf{k}$ = [k_0, 0, 0], [-k_0, 0, 0], [0, k_0, 0], [0, -k_0, 0]) and the doubly degenerate valley ground states Δ_2 ($\mathbf{k}$ = [0, 0, k_0], [0, 0, -k_0]), with an energy splitting of $\sim$ 0.2 eV for Si on relaxed $\mathrm{Si}_{0.7}\mathrm{Ge}_{0.3}$ [81]. Therefore, the Δ_4 valleys are energetically irrelevant, and we only need to consider the two low-lying Δ_2 valleys..

The presence of electrostatic fields along the (001) direction (the quantum well growth direction) further lifts the Δ_2 valley degeneracy and gives rise to a valley splitting E_V. Because the coupling matrix element is proportional to the interface electric field E_i, one can expect a linearly dependent valley splitting $E_V \propto E_i$. Indeed, in accumulation-only devices where dots are directly accumulated underneath gate electrodes, recent experiments have demonstrated a gate-tunable valley splitting that scales linearly with the gate voltage [101] . Up until now, we have been assuming a flat and defect-free heterostructure interface, with the growth direction of the heterostructure perfectly aligned with the [001] direction. Under these conditions, the valley index is a good quantum number and the valley splitting is maximized with the valley eigenstates fully coupled.

In reality, the growth direction of the heterostructure (z direction) does not perfectly match with the (001) lattice direction. This lattice miscut (typically under 1 degree) and other surface defects result in atomic steps in the quantum well that lead

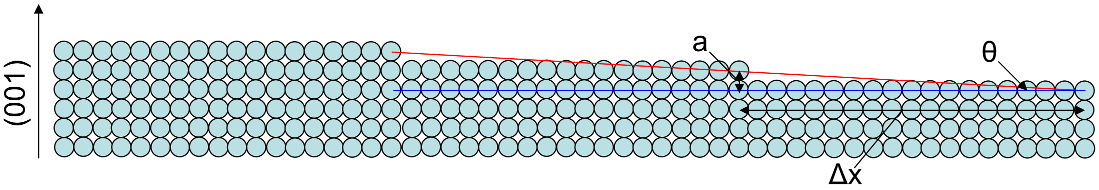

Figure 5.3: Schematic of lattice miscut in Si/SiGe heterostructure. The blue line corresponds to the lattice plane perpendicular to (001) direction, while the red line corresponds to the cut direction of Si substrate. The resulting atomic steps are separated by $\Delta x = \frac{a}{\tan \theta}$, in which a $\approx$ 0.54 nm is the lattice constant of Si and θ is the lattice miscut angle.

to destructive interference between the valley states, which in turn suppress the valley splitting [92]. The valley splitting, instead of the singlet-triplet splitting, becomes the smallest energy scale in the device, limiting the size of the readout window. Based on the variational principle, theorists have also predicted that the atomic steps give rise to the valley-orbit coupling, which mixes the pure valley states with higher orbital levels, transforming the ground states into valley-orbit mixed states [93]. This is consistent with the energy scale and the orbital nature of the low-lying excited states we observed in our dual-gated devices [51]. Valley-orbit coupling has also been posited as a possible mechanism leading to faster qubit relaxation, analogous to spin-orbit coupling [93, 21].

Assuming a typical lattice miscut angle of 0.5 degrees and Si lattice constant of 0.54 nm, one can estimate an average separation of atomic steps to be $\Delta x \approx \frac{0.54}{\tan 0.5^\circ} \approx$ 62 nm [Fig. 5.3]. Intuitively, one can expect that reducing the electron wavefunction span will lower the probability of having the wavefunction overlap with a step edge. Applying an electric or magnetic field confines the electron wavefunction, therefore leading to potentially larger valley splittings [92, 93, 101]. The tightest electron confinement has been achieved recently in accumulation-only device architectures [101]. The strong electron confinement, combined with the tunable interface electric field, has given rise to a valley splitting as large as 0.8 meV, approaching the theoretically predicted maximum value in Si/SiGe heterostructures [101].

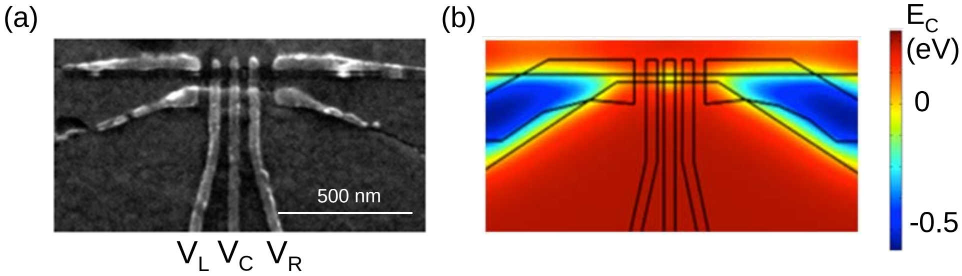

Figure 5.4: (a) A SEM image of a typical accumulation only device developed in the Petta Lab. (b) Simulation of its electrostatic potential with realistic gate voltages applied.

5.2 Accumulation-Only Device Development

Motivated by the large valley splitting recently measured by the Dzurak group [101], we have been developing our own accumulation-only device structure in the Petta Lab. Figure 5.4(a) shows a SEM image of the new device geometry. There are two layers of Al gates in the device, namely the 25 nm thick screening gates deposited directly on top of the heterostructure and the 45 nm thick accumulation gates deposited on top of those. The two layers of gates are electrically isolated from each other by a native Al_2O_3 layer with a thickness of around 5 nm. In contrast to the dual-gate DQD devices discussed in the previous chapter, there is no global top gate or global 2DEG accumulation in this device. The dot is locally accumulated by the 45 nm thick center plunger gate V_C, and a comparably negative voltage is applied on the screening gates (top and bottom part of the SEM image) to prevent unnecessary 2DEG accumulation outside the active dot region. The left plunger gate voltage V_L and right plunger voltage V_R are used to adjust the lead-dot coupling, and a pair of comparably large accumulation gates form a conducting channel all the way from the active dot region towards the ion-implanted ohmic contacts.

The simulation shown in Figure 5.4(b) demonstrates a potentially more uniform and tighter confinement potential, and may result in a larger valley splitting. In addition, the dot is formed using a single accumulation gate compared to many depletion

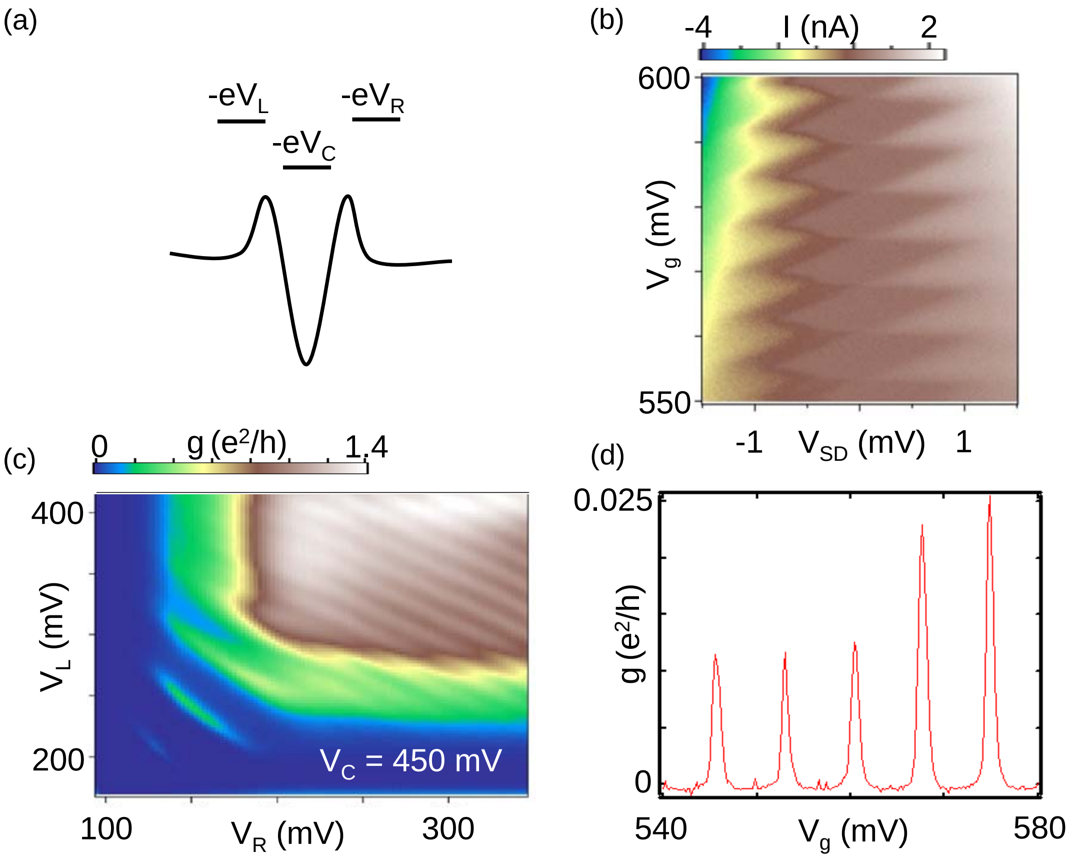

Figure 5.5: (a) Schematic diagram showing the confinement potential of the device. The dot is accumulated locally using a single gate V_C, where the lead-dot barriers are controlled by two plunger gate voltages V_L and V_R. (b) Coulomb diamond measured in current as a function of gate voltage V_g and source-drain bias voltage. (c) Measured conductance as a function of plunger gate voltages V_L and V_R, in a device with similar gate geometry as in Figure 5.4. (d) 1D conductance measurement as a function of V_g, demonstrating typical Coulomb blockade peaks.

gates in our previous device architectures. Due to the local nature of the dot accumulation, the dot is predominantly controlled by a single accumulation gate instead of being equally coupled to many depletion gates. The reduced cross-capacitive coupling promises a more easily tunable Hamiltonian, by providing independent tuning of the dot potential, dot-lead tunnel couplings, and the interdot tunnel coupling. Furthermore, scaling up the current SQD design to a DQD, triple quantum dot (TQD) or quadruple quantum dot (QQD) only requires adding more plunger gates between the ohmic accumulation gates, making the process lithographically easy.

We have cooled down a device fabricated in this gate architecture, demonstrating the formation of a single quantum dot. Figure 5.5(a) depicts the SQD confinement potential, where the dot-lead tunnel barrier is controlled by the gate voltages V_L and V_R and the dot chemical potential is tuned by the center plunger gate voltage V_C. By applying an appropriate combination of gate voltages, it is possible to form a single quantum dot [Fig. 5.5(a)]. Figure 5.5(c) shows measurements of the conductance as a function of plunger gates V_L and V_R. The parallel lines are Coulomb blockade peaks [Fig. 5.5(d)], indicative of single dot formation. In addition, the Coulomb diamonds [Fig. 5.5(b)] have also been observed in the current measurement, further confirming the single dot formation.

5.3 Future Si Spin Qubit Devices: Singlet-Triplet Qubits and Exchange-Only Qubits

In the previous section, we demonstrated the fabrication of accumulation only SQDs. Qubit rotations can be achieved for a single electron spin in a SQD using electron spin resonance (ESR) techniques [102], where the qubit basis states are defined by the Zeeman-split single electron spin states. However, full access to the Bloch sphere as well as controlled coherent Rabi oscillations using ESR is technically challenging, as the Rabi oscillation frequency is proportional to the applied microwave power. The realization of robust electron spin qubits therefore requires scaling up the SQD device to DQD and TQD device geometries, which allows us to explore singlet-triplet qubits and exchange-only qubits.

In the first chapter, we introduced singlet-triplet spin qubits [30, 21, 34]. In a singlet-triplet qubit, the z-axis rotation frequency is set by the exchange coupling J and the x-axis rotation frequency is set by the hyperfine field difference ΔB_{nuc}. Rotations about two-axes provide full access to the Bloch sphere. In GaAs singlet-triplet spin qubits, σ_z oscillations were demonstrated by simply tuning the detuing parameter ε [30], and nuclear spin polarization was used to generate a field gradient [32].

However, the hyperfine field is much weaker in Si/SiGe quantum dots, whose naturally abundant isotope contains zero nuclear spin. While this promises improved qubit coherence, a much deeper pulse in the detuning parameter ε is required to successfully project the qubit state towards the x-y plane of the Bloch sphere, which introduces further uncertainties and inefficiencies into the coherent manipulation of the qubit states [90]. Furthermore, in an ultra-coherent Si qubit where the Si 2DEG layer is isotopically purified, the same σ_x rotation schemes would cease to function.

There are many ways in which a σ_x rotation can be performed in the absence of nuclear field. One example is to implement a micromagnet next to the DQD, creating a slanting magnetic field that defines the σ_x matrix elements [102]. Figure 5.6(a) shows our old dual-gated device design with a 20 nm nickel micro-magnet deposited right next the active DQD device. Under a 100 mT external magnetic field along the x-direction, the nickel layer is magnetized and creates a strong local field that decays quickly as a function of distance. Figure 5.6(b) shows a simulation of B_Z as a function of distance to the micromagnet edge, in the plane that cuts through the center of the micromagnet. As expected, the field is strong in the proximity of the micromagnet, but decays quickly as a function of distance. Careful alignment of the micro-magnet provides a field difference of $\Delta B \approx 5$ mT between the left and right dot, suitable for singlet-triplet qubit operations. The fabrication recipe of the micromagnet has already been well defined in the Petta Lab. Therefore it would be lithographically trivial to implement the micromagnet in our new accumulation-only DQD device architecture.

Another way to enable efficient two-axis rotations in isotopically purified Si spin qubits is to implement the so-called exchange-only qubit scheme [103]. The qubit uti-

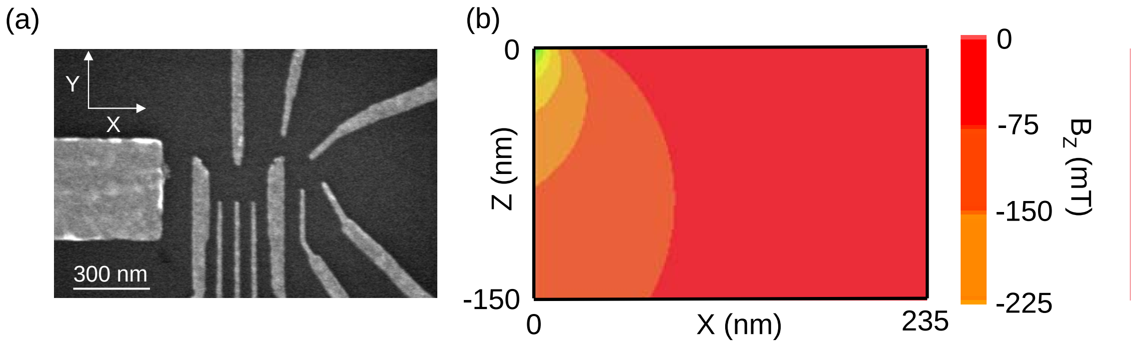

Figure 5.6: (a) A SEM image of a dual-gated DQD device with a nearby Ni micromagnet. (b) Simulated z component of the total field, B_Z, in the presence of a $B_X = 100$ mT external field as a function of distance to the magnet edge.

lizes three electron spin states, and therefore is realized in a TQD device architecture [89]. The three electron spin states contain eight eigenstates in total, namely four quadruplet states and two pairs of doublet states. In an exchange-only qubit, only the doublet states are utilized for qubit manipulation.

The total of four doublet states can be labeled as $|\Delta_{S_Z}\rangle$ and $|\Delta'_{S_Z}\rangle$, where $S_Z = \pm\frac{1}{2}$ is the z-projection of total electron spin. The qubit basis states are formed within the doublet states that share the same S_Z, and the system Hamiltonian is experimentally tuned by the detuning parameter across the three electron transitions (2, 0, 1) - (1, 1, 1) - (1, 0, 2), which continuously set the nearest neighbor exchange coupling J_{12} (left-most two electrons) and J_{23} (right-most two electrons). When pulsed towards the (1, 0, 2) charge configuration, the exchange coupling J_{12} eventually vanishes and $J_{12}/J_{23} \rightarrow 0$. The doublet eigenstates then become

$$|D_{\frac{1}{2}}\rangle = \frac{1}{\sqrt{6}}(|\uparrow\uparrow\downarrow\rangle + |\uparrow\downarrow\uparrow\rangle - 2|\downarrow\uparrow\uparrow\rangle) \tag{5.1}$$

$$|D_{-\frac{1}{2}}\rangle = \frac{1}{\sqrt{6}}(|\downarrow\downarrow\uparrow\rangle + |\downarrow\uparrow\downarrow\rangle - 2|\uparrow\downarrow\downarrow\rangle) \tag{5.2}$$

$$|D'_{\frac{1}{2}}\rangle = \frac{1}{\sqrt{2}}(|\uparrow\uparrow\downarrow\rangle - |\uparrow\downarrow\uparrow\rangle) \tag{5.3}$$

$$|D'_{-\frac{1}{2}}\rangle = \frac{1}{\sqrt{2}}(|\downarrow\downarrow\uparrow\rangle - |\downarrow\uparrow\downarrow\rangle). \tag{5.4}$$

Similarly, when pulsed towards the (2, 0, 1) charge configuration, the exchange coupling J_{23} eventually vanishes and $J_{23}/J_{12} \rightarrow 0$. The doublet eigenstates then become

$$|\overline{D}_{\frac{1}{2}}\rangle = -\frac{1}{\sqrt{6}}(|\downarrow\uparrow\uparrow\rangle + |\uparrow\downarrow\uparrow\rangle - 2|\uparrow\uparrow\downarrow\rangle) \tag{5.5}$$

$$|\overline{D}_{-\frac{1}{2}}\rangle = -\frac{1}{\sqrt{6}}(|\uparrow\downarrow\downarrow\rangle + |\downarrow\uparrow\downarrow\rangle - 2|\downarrow\downarrow\uparrow\rangle) \tag{5.6}$$

$$|\overline{D'}_{\frac{1}{2}}\rangle = -\frac{1}{\sqrt{2}}(|\uparrow\downarrow\uparrow\rangle - |\downarrow\uparrow\uparrow\rangle) \tag{5.7}$$

$$|\overline{D'}_{-\frac{1}{2}}\rangle = -\frac{1}{\sqrt{2}}(|\downarrow\uparrow\downarrow\rangle - |\uparrow\downarrow\downarrow\rangle). \tag{5.8}$$

These states are fundamental for exchange-only qubit definition and coherent manipulations [103]. For example, one can define $|D_{\frac{1}{2}}\rangle$ and $|D'_{\frac{1}{2}}\rangle$ as the qubit basis states. By pulsing towards the (1, 0, 2) charge configuration, these states become the system eigenstates and coherent Rabi oscillations around the σ_Z axis are achieved with a Rabi frequency proportional to the exchange coupling between the rightmost electron pair, J_{23}. $|\overline{D}_{\frac{1}{2}}\rangle$ and $|\overline{D'}_{\frac{1}{2}}\rangle$ defines the other rotation axes. The two exchange rotation axes are separated by 120 degrees on the Bloch sphere. Pulsing towards the (2, 0, 1) charge configuration will then allow coherent Rabi oscillations around this tilted axis, with a Rabi frequency proportional to the exchange coupling between the leftmost electron pair, J_{12}. Therefore, by only adjusting the detuning parameter ε, two-axis coherent oscillations and arbitrary access to the Bloch sphere can be achieved in an exchange-only qubit, without the need of a slanting magnetic field or dynamically polarized hyperfine field [104].

5.4 Summary

In this chapter, we have developed a new quantum dot device architecture with an accumulation-only gate design. The new device promises easier control of the system Hamiltonian as well as linear scalability towards more complicated qubit devices. Most importantly, the local nature of the dot accumulation scheme gives rise to a tighter and more uniform electronic confinement potential, promises enhanced valley splitting, a physical property crucial to the robustness of Si spin qubits.

We have demonstrated the fabrication of accumulation-only SQD devices. Working towards ultra-coherent spin qubits in isotopically purified Si, future work will include scaling-up the devices to DQD and TQD. Full Bloch sphere control can be achieved in singlet-triplet spin qubits in DQDs using the exchange interaction and local magnetic field gradients generated by micromagnets. In TQDs, full qubit control can be achieved by adjusting two exchange couplings in the device.

Chapter 6

Conclusions

At the time of this writing, qubits in solid state systems are being widely investigated, both experimentally and theoretically. Quantum computers [3, 4] have many advantages over the classical computers. First and foremost, the computational capability of a quantum computer in solving certain solving certain realistic problems is enhanced exponentially [5, 6]. Furthermore, the data storage mechanism is quantum mechanical and the data security is arguably unbreakable [7]. These advantages bode well for the education, industry, science, civil and military sectors. For this reason, despite the overwhelming challenges, great efforts are being put into realizing this quantum dream of human civilization.

To realize this vision, we must first demonstrate a robust qubit. Many approaches have been taken in solid state systems, such as the circuit quantum electrodynamics (cQED) architecture [8, 9, 10, 11, 12, 13, 14, 15, 16, 17, 18], nitrogen vacancy centers in diamond [19] and electrons in electrically defined semiconductor quantum dots (which is the focus of this thesis). Many landmark experiments demonstrating qubit realization and coherent control [21, 30, 31, 32, 33, 34, 35, 36] have been successfully performed in GaAs quantum dots in the past fifteen years, inspired by the Loss-DiVincenzo proposal [20, 39]. However, due to the relatively strong spin-orbit interaction and hyperfine interaction in the GaAs 2DEG system, the qubit robustness and coherence are found to be orders of magnitude lower [21, 30, 31, 32, 33, 34, 35, 36] than required by a practical quantum computer.

Although pulse techniques such as dynamic decoupling can improve the qubit coherence to some extent, a more direct and effective approach is to improve the qubit environment by switching to a different 2DEG host material. As a result, silicon becomes one of the best candidates for future ultra-coherent qubits [70], due to its much weaker spin-orbit coupling and hyperfine interaction. In addition, a nuclear-spin-free environment ("semiconductor vacuum") that is almost completely free of hyperfine interactions (with a ^{29}Si concentration smaller than 400 ppm) can be created for qubit electrons, using isotopic purification [71].

Motivated by Silicon's great promise for ultra-coherent qubits, we started the Si/SiGe QD project in the Petta Lab. At the beginning of this study, we were presented with many challenges in our attempts to fabricate high quality DQD devices. These difficulties include comparably lower heterostructure quality, significantly higher electron effective mass and the instability of P donors. Over the six years of my thesis research, these challenges have been overcome and we have successfully realized high quality single-electron charge qubits in Si quantum dots.

Hoping to emulate the successful path of GaAs QD research, we began our project by fabricating depletion-mode DQDs on modulation-doped Si/SiGe heterostructures. With careful engineering and control of the heterostruture growth parameters, we managed to obtain many Si 2DEG samples of decent quality. We resolved the challenge of the high effective mass by optimizing our electron beam lithography recipe, after which we were able to fabricate many-electron QDs and demonstrate basic transport measurements in them, such as Coloumb blockade and finite bias triangles. In addition, we successfully realized charge sensing using both DC and RF measurement techniques.

However, we were unable to reach the few electron regime in the DQDs due to device instabilities and unintended formation of triple quantum dots at low charge occupancies. The difficulties of forming high quality quantum dots from doped Si/SiGe heterostructures have encouraged us to develop new approaches to realize Si qubits. Based on results from HRL [90], where undoped structures were used, we have concluded the only path forward is to redesign the heterostructure and eliminate the Phosphorus donors altogether, using a global top gate to accumulate the 2DEG instead. Based on these newly developed enhancement-mode heterostructures, we have consistently and reproducibly realized single electron charge qubits in dual-gated Si DQD devices. We systematically measured the interdot relaxation time T_1 of a single electron trapped in a Si DQD as a function of detuning ε and interdot tunnel coupling t_c and demonstrated a four order of magnitude variation in T_1 using a single depletion gate, all of the way up to $T_1 = 45$ μs [38, 51]. We showed that our data are consistent with a phonon mediated charge relaxation theory [51]. In addition, we also used photon assisted tunneling (PAT) to probe the energy level structure of the single electron system, demonstrating spectroscopy with an energy resolution of ~ 1 μeV. In contrast with single electron GaAs dots, we observed low-lying excited states ~ 55 μeV above the ground state, an energy scale that is consistent with previously measured valley splittings [92, 90].

Despite their success in hosting high quality charge qubits, for over ten dual-gated devices that we have investigated at cryogenic temperature, no sign of spin blockade has been observed at the two-electron transitions. We suspect this is due to disorder near the quantum well, which is predicted to result in small valley splittings. This challenge prevented us from establishing robust spin qubits and motivated us to develop new types of DQD devices. A few months before this thesis was written, we successfully developed a fabrication recipe for the next generation of Si QD devices, namely the accumulation-only device architecture. The new device architecture promises enhanced valley splitting, less cross-gate-capacitive coupling and linear scaling of QDs. Based on the new device architecture, our future research will involve realizing singlet-triplet qubits in DQDs, implementing exchange-only qubits in TQDs and fabricating spin chains. We look forward to the exciting on-going research of Si qubits in the Petta Lab, both for the promise it holds for a future quantum computer and for studies of fundamental quantum physics.

Appendix A

Low-Frequency Circuits

This appendix describes the low frequency measurement setup used to acquire data for this thesis. Low-frequency charge-sensing, dot conductance, and dot current measurement circuits are described. Figure A.1 shows the circuit diagram.

The dot conductance and current are measured using a voltage-biased circuit configuration. An Agilent 33250 signal generator creates AC and DC signals. These signals are divided by a 1000:1 voltage divider consisting a 50 kΩ and 50 Ω resistors. The divided signal is then connected to the source reservoir, providing low-frequency source-drain excitation and the DC source-drain bias voltage.

The resulting current is measured with an Ithaco current amplifier, giving a voltage output proportional to the gain of the amplifier times the current flowing into the drain reservoir ("system ground" defined by the ground of the current amplifier). For DC current measurements, the output of the current amplifier is first filtered by a low-pass RC filter (with a RC time constant of 0.1 ms, the same as the typical current amplifier rise time used in our DC measurements) to filter out the AC signal, and then sent to a National Instruments data acquisition (NIDAQ) system. For AC conductance measurements, the output of the current amplifier is connected to the Stanford Research (SR) lock-in amplifier (which is synchronized with the Agilent

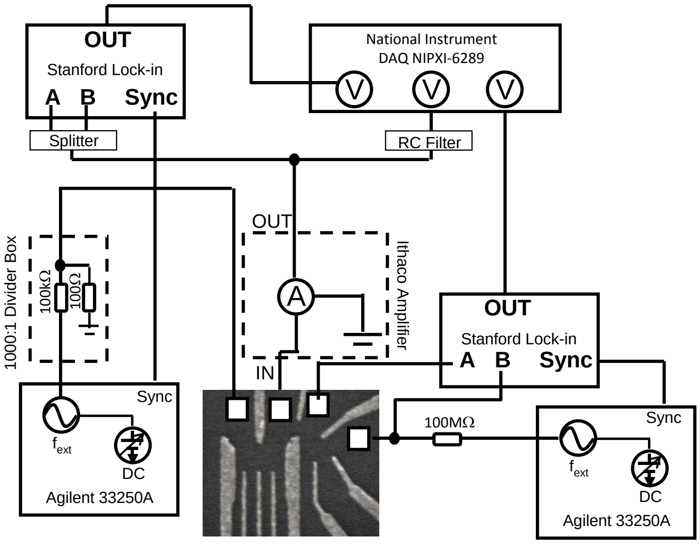

Figure A.1: Low-frequency measurement setup used to acquire data for this thesis. The diagram contains low-frequency charge-sensing, dot conductance, and dot current measurement circuits. The dot conductance and current are measured using a voltage-biased circuit configuration. AC and DC signals created by an Agilent 33250 signal generator are divided by a 1000:1 voltage divider before being connected to the source reservoir. The resulting current is measured with an Ithaco current amplifier. For DC current measurements, the output of the current amplifier is first filtered by a low-pass RC filter before being sent to a National Instruments Data acquisition (NIDAQ) system. For AC conductance measurements, the output of the current amplifier is connected to the Standard Research (SR) lock-in amplifier, the output of which is then sent to the NIDAQ. Simultaneous measurements of DC current and AC differential conductance are allowed with this setup. The charge sensing measurement is performed using a current-biased circuit configuration. The AC and DC signals created by another Agilent 33250 signal generator are connected to a 100 MΩ resistor and then connected to the source contact of the QPC channel. The differential input ports on another SR lock-in amplifier are connected to the contacts on both sides of the QPC channel to measure the voltage drop across it. The output of the lock-in is connected to the NIDAQ, and the measured output voltage is then converted numerically to QPC conductance in the data acquisition program.

33250 signal generator). The output of the SR lock-in amplifier is sent to the NIDAQ, and the measured output voltage is then converted numerically to dot conductance in the data acquisition program. This setup allows simultaneous measurements of the DC current and AC differential conductance of the quantum dot device.

The charge sensing measurement is performed using a current-biased circuit configuration. The AC and DC signals created by another Agilent 33250 signal generator are connected to a 100 MΩ resistor and then connected to the source contact of the QPC channel. We normally operate the QPC with a conductance around 0.1 g_0, which corresponds to a QPC resistance of ∼256 kΩ, orders of magnitude smaller than the 100 MΩ resistor. Therefore, the 33250 signal generator together with the 100 MΩ resistor can be considered as a current source in the charge-sensing measurement.

The differential input ports on another SR lock-in amplifier (which is synchronized with the Agilent 33250 signal generator) are connected to the ohmic contacts on both sides of the QPC channel to measure the voltage drop across the QPC. The output of the lock-in is connected to the NIDAQ, and the measured output voltage is converted numerically to QPC conductance in the data acquisition program.

Appendix B

Radio-Frequency Circuits

This appendix describes the radio-frequency measurement setup used to acquire data for this thesis. Fast charge-sensing, PAT spectroscopy and charge relaxation time T_1 measurement circuits are described. Figure B.1 shows the circuit diagram.

The fast charge sensing measurement utilizes the RF reflectometry technique. In this setup, a RF microwave excitation is generated by an Agilent N5181A signal generator, typically with a frequency ranging from 300 MHz to 500 MHz. This signal is sent to a Mini-Circuit ZEDC-15-2B directional coupler. The output of the directional coupler is connected to a frequency doubler and a high-pass filter, and then connected to the LO port of Analog Devices AD5348 Evaluation Board. This portion of the signal is used as a reference for demodulation, which will be hereafter referred to as the reference signal. The other signal exiting the directional coupler is attenuated by 50 dB at room temperature, and further attenuated by a -30 dB attenuator at 4K and another Mini-Circuit ZEDC-15-2B directional coupler (-15 dB) at the cold plate of the dilution refrigerator (50 mK), before it is connected to the source contact of the QPC via a bias tee. This portion of the signal will be hereafter referred to as the carrier signal.

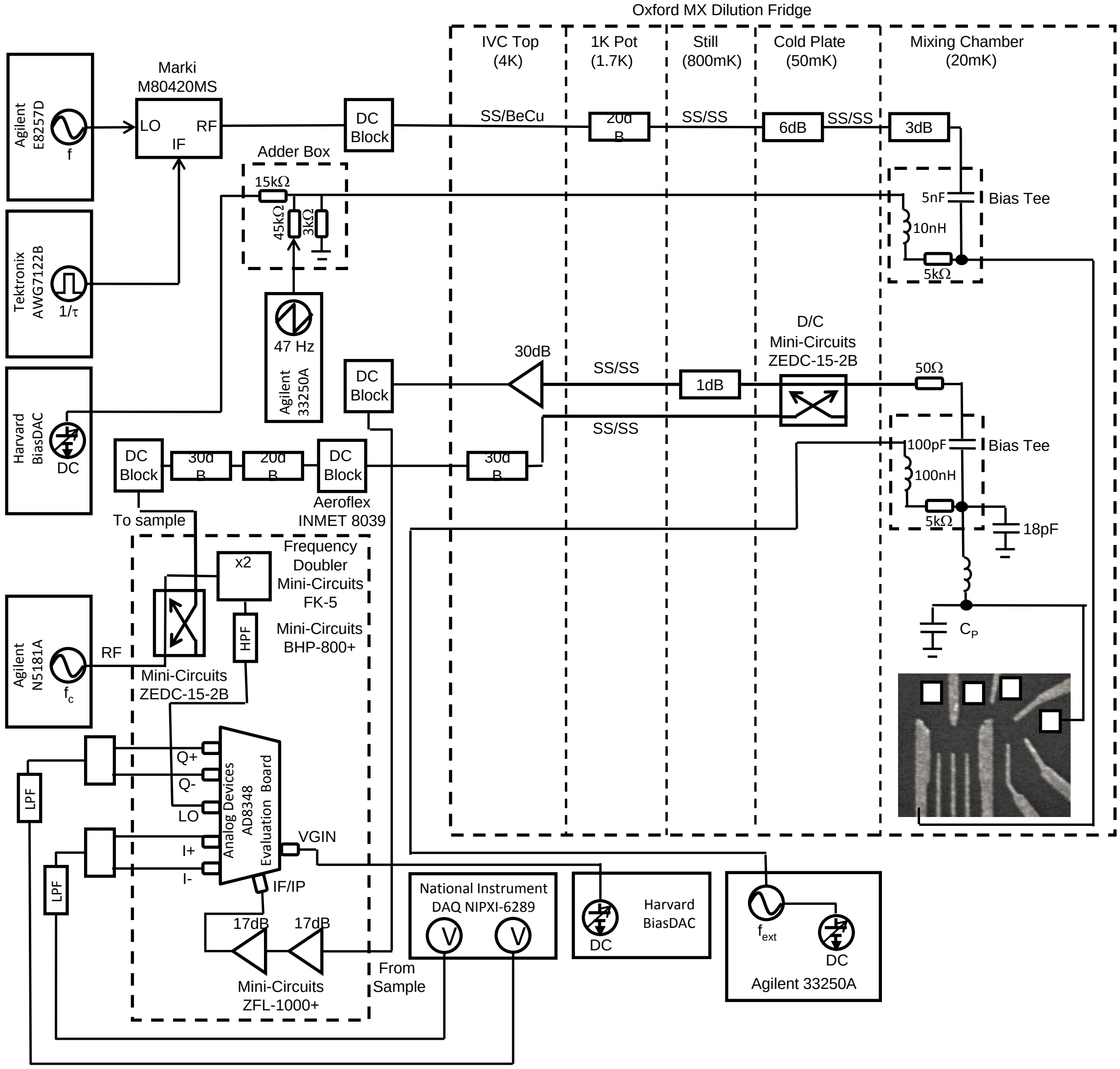

Figure B.1: Radio-frequency measurement setup used to acquire data for this thesis. Fast charge sensing, PAT spectroscopy and charge relaxation time T_1 measurement circuits are included. The fast charge sensing measurement utilizes the RF reflectometry technique. The QPC channel, the parasitic capacitance C_P together with the carefully-chosen capacitors and inductors, forms the so-called impedance-matching network. When the carrier wave frequency f_C matches with the resonant frequency f_R, the reflected signal will be extremely sensitive to changes in the QPC conductance, g_{QPC}. This enables a fast charge sensing measurement. In the PAT spectroscopy measurement, an Agilent E8257D generates a microwave signal with typical frequency f_{ext} ranging from 5 GHz to 30 GHz to drive the resonant transition. The microwave signal is rapidly switched on and off using a Marki M80420MS switch, the IF port of which is connected to a Tektronix AWG7122B arbitrary waveform generator. This enables application of chopped microwave excitation with an 50% on/off ratio. By varying the period τ of the microwave excitation, a measurement of the charge relaxation time T_1 can be performed.

The bias tee consists of a 5 nF capacitor, 5 kΩ resistor and 10 nH inductor, which enables simultaneous application of low frequency (from Agilent 33250A) and radio frequency (from Agilent N5181A) excitations to the connected ohmic contacts and gate electrodes. The QPC channel, the parasitic capacitance C_P together with the carefully-chosen capacitors and inductors, forms the so-called impedance-matching network. The attenuated signal from N5181A is then reflected by the impedance-matching network. When the carrier wave frequency f_C matches the resonant frequency f_R (typically around 430 MHz in our experiments), the network's impedance become 50 Ω (same as the characteristic impedance of the coax cable used in out experiments) and the reflected signal is minimized. In such condition, the reflected signal will be extremely sensitive to changes in the QPC conductance, g_{QPC}, as it modifies the impedance of the matching network. Therefore, by setting $f_C = f_R$ and monitoring the reflected signal, fast measurement of g_{QPC} can be achieved.

This is of course just a part of the story. Now that we have fast measurements of the QPC conductance at any given DQD gate configuration, we need to sweep the gate voltages in order to obtain a full charge stability diagram. In the DC charge sensing measurement, each data point is taken separately as the data taking program steps the gate voltages V_L and V_R by controlling the Harvard BiasDAC. In the fast charge sensing measurement, both a DC voltage offset (provided by the BiasDAC) and a low-frequency AC sweep (triangular wave generated by another Agilent 33250A) are applied to V_L through an adder box consisting of a series of 45 kΩ, 15 kΩ and 3 kΩ resistors. While V_R is still stepped by the BiasDAC, a triangular waveform is used to sweep V_L at a frequency of 47 Hz.

Sweeping these gate voltages (V_R and V_L) modulates g_{QPC} and therefore the amplitude of the reflected signal. If we Fourier-transform the g_{QPC} modulation, the dominating terms would be low-frequency components. For the sake of our discussion here, we will focus on one of these low frequency components, with a frequency of f_0. The amplitude-modulated (AM) reflected signal will then have two frequency components, $f_+ = f_C + f_0$ and $f_- = f_C$ - f_0. The reflected signal is then consecutively amplified by a 30 dB Cryogenic amplifier at 4K and two 17 dB amplifiers before it is connected to the IF/IP port of the Analog Devices AD8348 evaluation board. The signal is further amplified by a built-in variable-gain amplifier (VGA), with a gain set by BiasDAC through the VGIN port of the evaluation board.

The frequency of the amplified signal is then doubled by a built-in frequency doubler in the evaluation board, in order to separate the in-phase (I) and quadrature phase (Q) components (instead of a 90-degree phase difference, they will have a 180-degree phase difference with each other, making them easier to separate and process). The frequency components of the amplified wave then become $2f_+ = 2f_C + 2f_0$ and $2f_- = 2f_C$ - $2f_0$. It then mixes with the reference wave at frequency $2f_C$ in the built-in mixer in the evaluation board, resulting in a total of three frequency components, namely $4f_C + 2f_0$, $4f_C$ - $2f_0$ and $2f_0$. The frequency of the mixed signal is then divided by a factor of two in the evaluation board, resulting in new frequency components, namely $2f_C + f_0$, $2f_C$ - f_0 and f_0. The high-frequency components ($2f_C + f_0$, $2f_C$ - f_0) are then filtered by a low-pass filter, leaving only the f_0 waveform (which is the original g_{QPC} response to the sweep signal). The resulting output waveform from the Q and I ports are connected to a National Instrument data acquisition (NIDAQ) board, and then numerically converted to the fast charge-sensing data.

The PAT spectroscopy and charge relaxation time T_1 measurements rely on the capability to apply well-calibrated and well-controlled microwave excitations to the gate electrodes on the DQD device. An Agilent E8257D generates a microwave signal with typical frequency f_{ext} ranging from 5 GHz to 30 GHz. The signal is fed through a Marki M80420MS switch and subsequently filtered by a 20 dB attenuator at 1 K, a 6 dB attenuator at 50 mK and a 3 dB attenuator at 20 mK before it is connected to V_L. When the single photon energy matches the energy-level energy splitting in the DQD, PAT peaks can be observed in the RF fast charge-sensing measurement described above. By stepping f_{ext} and detuning ε, a full energy spectroscopy of the DQD can be measured.

In addition, a series of step pulses generated by the Tektronic AWG7122B arbitrary waveform generator is connected to the IF port of Marki M80420MS. This enables fast switching of the applied microwave excitation. In the charge relaxation time T_1 measurement, the microwave signal generated by the Agilent E8257D is chopped by the AWG-controlled Marki M80420MS with an 50% on/off ratio. By varying the period τ of the microwave excitation, a measurement of the charge relaxation time T_1 can be performed.

Bibliography

[1] B. J. Copeland. The modern history of computing. In *The Stanford Encyclopedia of Philosophy*. 2008.

[2] J. Bardeen and W. H. Brattain. *Physical Review*, 74:230–231, 1948.

[3] D. Deutsch. *Proc. R. Soc. A*, 400:97–117, 1985.

[4] M. A. Nielsen and I. L. Chuang. *Quantum Computation and Quantum Information*. Cambridge University Press, Cambridge, 2000.

[5] P. W. Shor. *SIAM J. Comput.*, 26:1484–1509, 1997.

[6] L. K. Grover. In *Proceedings of the Twenty-eighth Annual ACM Symposium on Theory of Computing*, 1996.

[7] W. K. Wootters and W.H. Zurek. *Nature (London)*, 299:802, 1982.

[8] A. Blais, R-S. Huang, A. Wallraff, S. M. Girvin, and R. J. Schoelkopf. *Phys. Rev. A*, 69:062320, 2004.

[9] M. Ansmann, H. Wang, R. C. Bialczak, M. Hofheinz, E. Lucero, M. Neeley, A. D. O'Connell, D. Sank, M. Weides, J. Wenner, A. N. Cleland, and J. M. Martinis. *Nature (London)*, 461:504, 2009.

[10] O. Astafiev, Yu. A. Pashkin, Y. Nakamura, T. Yamamoto, and J. S. Tsai. *Phys. Rev. Lett.*, 93:267007, 2004.

[11] K. Bladh, T. Duty, D. Gunnarsson, and P. Delsing. *N. Jour. Phys.*, 7:180, 2005.

[12] T. Duty, D. Gunnarsson, K. Bladh, and P. Delsing. *Phys. Rev. B*, 69:140503, 2004.

[13] T. Duty, G. Johansson, K. Bladh, D. Gunnarsson, C. Wilson, and P. Delsing. *Phys. Rev. Lett.*, 95:206807, 2005.

[14] A. Guillaume, J. F. Schneiderman, P. Delsing, H. M. Bozler, and P. M. Echternach. *Phys. Rev. B*, 69:132504, 2004.

[15] G. Johansson, L. Tornberg, and C. M. Wilson. *Phys. Rev. B*, 74:100504, 2006.

[16] J. Majer, J. M. Chow, J. M. Gambetta, J. Koch, B. R. Johnson, J. A. Schreier, L. Frunzio, D. I. Schuster, A. A. Houck, A. Wallraff, A. Blais, M. H. Devoret, S. M. Girvin, and R. J. Schoelkopf. *Nature (London)*, 449:443–447, 2007.

[17] J. B. Majer, F. G. Paauw, A. C. J. ter Haar, C. J. P. M. Harmans, and J. E. Mooij. *Phys. Rev. Lett.*, 94:090501, 2005.

[18] Y. Nakamura, Yu. A. Pashkin, and J. S. Tsai. *Nature (London)*, 398:786–788, 1999.

[19] D. D. Awschalom, R. Epstein, and R. Hanson. *Scientific American*, pages 84–91, October 2007.

[20] D. Loss and D. P. DiVincenzo. *Phys. Rev. A*, 57:120–126, 1998.

[21] R. Hanson, L. P. Kouwenhoven, J. R. Petta, S. Tarucha, and L. M. K. Vandersypen. *Rev. Mod. Phys.*, 79:1217–1265, 2007.

[22] G. Burkard, H-A. Engel, and D. Loss. *Fortschr. Phys.*, 48:965–986, 2000.

[23] M. A. Eriksson, M. Friesen, S. N. Coppersmith, R. Joynt, L. J. Klein, K. Slinker, C. Tahan, P. M. Mooney, J. O. Chu, and S. J. Koester. *Quantum Inf. Proc.*, 3:133, 2004.

[24] L. Jacak, P. Hamrylak, and A. Wojs. *Quantum Dots*. Springer, Germany, 1998.

[25] L. P. Kouwenhoven, D. G. Austing, and S. Tarucha. *Rep. Prog. Phys.*, 64:701–736, 2001.

[26] L. P. Kouwenhoven, C. M. Marcus, P. L. McEuen, S. Tarucha, R. M. Westervelt, and N. S. Wingreen. In *Mesoscopic Electron Transport*, 1997.

[27] L. P. Kouwenhoven, T. H. Oosterkamp, M. W.S. Danoesastro, M. Eto, D. G. Austing, T. Honda, and S. Tarucha. *Science*, 278:1788–1792, 1997.

[28] E. A. Laird. *Electrical control of quantum dot spin qubits*. PhD thesis, Harvard University, 2009.

[29] B. Michaelis, C. Emary, and C. W. J. Beenakker. *Euro. Phys. Lett.*, 73:677–683, 2006.

[30] J. R. Petta, A. C. Johnson, J. M. Taylor, E. A. Laird, A. Yacoby, M. D. Lukin, C. M. Marcus, M. P. Hanson, and A. C. Gossard. *Science*, 309:2180–2184, 2005.

[31] J. R. Petta, A. C. Johnson, A. Yacoby, C. M. Marcus, M. P. Hanson, and A. C. Gossard. *Phys. Rev. B*, 72:161301, 2005.

[32] J. R. Petta, J. M. Taylor, A. C. Johnson, A. Yacoby, M. D. Lukin, C. M. Marcus, M. P. Hanson, and A. C. Gossard. *Phys. Rev. Lett.*, 100:067601, 2008.

[33] J. R. Petta, H. Lu, and A. C. Gossard. *Science*, 327:669–672, 2010.

[34] J. M. Taylor, J. R. Petta, A. C. Johnson, A. Yacoby, C. M. Marcus, and M. D. Lukin. *Phys. Rev. B*, 76:035315, 2007.

[35] H. Bluhm, S. Foletti, I. Neder, M. Rudner, D. Mahalu, V. Umansky, and A. Yacoby. *Nat. Phys.*, 7:109, 2011.

[36] A. Johnson. *Charge Sensing and Spin Dynamics in GaAs Quantum Dots*. PhD thesis, Harvard University, 2005.

[37] D. J. Reilly, C. M. Marcus, M. P. Hanson, and A. C. Gossard. *Appl. Phys. Lett.*, 91:162101, 2007.

[38] J. R. Petta, A. C. Johnson, C. M. Marcus, M. P. Hanson, and A. C. Gossard. *Phys. Rev. Lett.*, 93:186802, 2004.

[39] D. P. DiVincenzo. *Fortschr. Phys.*, 48:771–783, 2000.

[40] S. Gustavsson, R. Leturcq, B. Simovic, R. Schleser, T. Ihn, P. Studerus, K. Ensslin, D. C. Driscoll, and A. C. Gossard. *Phys. Rev. Lett.*, 96:076605, 2006.

[41] C. W. J. Beenakker. *Phys. Rev. B*, 44:1646–1656, 1991.

[42] H. Grabert and M. H. Devoret. *Single Charge Tunneling, Coulomb Blockade Phenomena in Nanostructures*. NATO ASI Plenum, New York, 1992.

[43] L. J. Klein, K. A. Slinker, J. L. Truitt, S. Goswami, K. L. M. Lewis, S. N. Coppersmith, D. W. van der Weide, M. Friesen, R. H. Blick, D. E. Savage, M. G. Lagally, C. Tahan, R. Joynt, M. A. Eriksson, J. O. Chu, J. A. Ott, and P. M. Mooney. *Appl. Phys. Lett.*, 84:4047–4049, 2004.

[44] W. G. van der Wiel, S. De Franceschi, J. M. Elzerman, T. Fujisawa, S. Tarucha, and L. P. Kouwenhoven. *Rev. Mod. Phys.*, 75:1–22, 2002.

[45] L. DiCarlo, H. J. Lynch, A. C. Johnson, L. I. Childress, K. Crockett, C. M. Marcus, M. P. Hanson, and A. C. Gossard. *Phys. Rev. Lett.*, 92:226801, 2004.

[46] C. Barthel, M. Kjærgaard, J. Medford, M. Stopa, C. M. Marcus, M. P. Hanson, and A. C. Gossard. *Phys. Rev. B*, 81:161308, 2010.

[47] T. M. Buehler, D. J. Reilly, R. P. Starrett, N. A. Court, A. R. Hamilton, A. S. Dzurak, and R. G. Clark. *J. Appl. Phys.*, 96:4508–4513, 2004.

[48] M. C. Cassidy, A. S. Dzurak, R. G. Clark, K. D. Petersson, I. Farrer, D. A. Ritchie, and C. G. Smith. *Appl. Phys. Lett.*, 91:222104, 2007.

[49] A. C. Johnson, C. M. Marcus, M. P. Hanson, and A. C. Gossard. *Phys. Rev. B*, 71:115333, 2005.

[50] A. C. Johnson, J. R. Petta, C. M. Marcus, M. P. Hanson, and A. C. Gossard. *Phys. Rev. B*, 72:165308, 2005.

[51] K. Wang, C. Payette, Y. Dovzhenko, P. W. Deelman, and J. R. Petta. *Phys. Rev. Lett.*, 111:046801, 2013.

[52] K. D. Petersson, C. G. Smith, D. Anderson, P. Atkinson, G. A. C. Jones, and D. A. Ritchie. *Phys. Rev. Lett.*, 103:016805, 2009.

[53] K. D. Petersson, J. R. Petta, H. Lu, and A. C. Gossard. *Phys. Rev. Lett.*, 105:246804, 2010.

[54] K. Ono, D. G. Austing, Y. Tokura, and S. Tarucha. *Science*, 297:1313–1317, 2002.

[55] M. Prada, R. H. Blick, and R. Joynt. *Phys. Rev. B*, 77:115438, 2008.

[56] J. Könemann, R. J. Haug, D. K. Maude, V. I. Fal'ko, and B. L. Altshuler. *Phys. Rev. Lett.*, 94:226404, 2005.

[57] R. Winkler. *Spin-orbit coupling effects in two-dimensional electron and hole systems.* Springer, Berlin, 2003.

[58] N. W. Ashcroft and N. D. Mermin. *Solid State Physics.* Saunders College, 1976.

[59] J. D. Jackson. *Classical electrodynamics.* Wiley, 1999.

[60] C. Fasth, A. Fuhrer, L. Samuelson, Vitaly N. Golovach, and Daniel Loss. *Phys. Rev. Lett.*, 98:266801, 2007.

[61] K. C. Nowack, F. H. L. Koppens, Yu. V. Nazarov, and L. M. K. Vandersypen. *Science*, 318:1430–1433, 2007.

[62] I. A. Merkulov, Al. L. Efros, and M. Rosen. *Phys. Rev. B*, 65:205309, 2002.

[63] A. C. Johnson, J. R. Petta, J. M. Taylor, A. Yacoby, M. D. Lukin, C. M. Marcus, M. P. Hanson, and A. C. Gossard. *Nature (London)*, 435:925–928, 2005.

[64] F. H. L. Koppens, J. A. Folk, J. M. Elzerman, R. Hanson, L. H. Willems van Beveren, I. T. Vink, H. P. Tranitz, W. Wegscheider, L. P. Kouwenhoven, and L. M. K. Vandersypen. *Science*, 309:1346–1350, 2005.

[65] E. A. Laird, C. Barthel, E. I. Rashba, C. M. Marcus, M. P. Hanson, and A. C. Gossard. *Phys. Rev. Lett.*, 99:246601, 2007.

[66] E. Fermi. *Zeitschrift fur Physik*, 60:320–333, 1930.

[67] E. L. Hahn. *Physical Review*, 80:580–594, 1950.

[68] H. Y. Carr and E. M. Purcell. *Phys. Rev.*, 94:630–638, 1954.

[69] S. Meiboom and D. Gill. *Review of Scientific Instruments*, 29:688–691, 1958.

[70] E. A. Fitzgerald, Y.-H. Xie, D. Monroe, P. J. Silverman, J. M. Kuo, A. R. Kortan, F. A. Thiel, and B. E. Weir. *J. Vac. Sci. Technol. B*, 10:1807–1819, 1992.

[71] B. Andreas, Y. Azuma, G. Bartl, P. Becker, H. Bettin, M. Borys, I. Busch, M. Gray, P. Fuchs, K. Fujii, H. Fujimoto, E. Kessler, M. Krumrey, U. Kuetgens, N. Kuramoto, G. Mana, P. Manson, E. Massa, S. Mizushima, A. Nicolaus, A. Picard, A. Pramann, O. Rienitz, D. Schiel, S. Valkiers, and A. Waseda. *Phys. Rev. Lett.*, 106:030801, 2011.

[72] D. W. Greve. *Materials Science and Engineering: B*, 18:22 – 51, 1993.

[73] K. Ismail, M. Arafa, K. L. Saenger, J. O. Chu, and B. S. Meyerson. *Appl. Phys. Lett.*, 66:1077–1079, 1995.

[74] K. Ismail, B. S. Meyerson, and P. J. Wang. *Appl. Phys. Lett.*, 58:2117–2119, 1991.

[75] T. M. Lu, J. Liu, J. Kim, K. Lai, D. C. Tsui, and Y. H. Xie. *Appl. Phys. Lett.*, 90:182114, 2007.

[76] T. M. Lu, D. R. Luhman, K. Lai, D. C. Tsui, L. N. Pfeiffer, and K. W. West. *Appl. Phys. Lett.*, 90:112113, 2007.

[77] T. M. Lu, D. C. Tsui, C.-H. Lee, and C. W. Liu. *Appl. Phys. Lett.*, 94:182102, 2009.

[78] D. Monroe, Y. H. Xie, E. A. Fitzgerald, and P. J. Silverman. *Phys. Rev. B*, 46:7935–7937, 1992.

[79] R. Braunstein, A. R. Moore, and F. Herman. *Phys. Rev.*, 109:695–710, 1958.

[80] R. People and J. C. Bean. *Appl. Phys. Lett.*, 48:538–540, 1986.

[81] F. Schäffler. *Semicond. Sci. Technol.*, 12:1515, 1997.

[82] D. Monroe, Y. H. Xie, E. A. Fitzgerald, P. J. Silverman, and G. P. Watson. *J. Vac. Sci. Technol. B*, 11:1731–1737, 1993.

[83] M. Thalakulam, C. B. Simmons, B. M. Rosemeyer, D. E. Savage, M. G. Lagally, M. Friesen, S. N. Coppersmith, and M. A. Eriksson. *Appl. Phys. Lett.*, 96:183104, 2010.

[84] K. Yao. *Silicon And Silicon-germanium Epitaxy For Quantum Dot Device Fabrications Towards An Electron Spin-Based Quantum Computer.* PhD thesis, Princeton University, 2009.

[85] J. Sailer, A. Wild, V. Lang, A. Siddiki, and D. Bougeard. *N. Jour. Phys.*, 12:113033, 2010.

[86] G. Abstreiter, H. Brugger, T. Wolf, H. Jorke, and H. J. Herzog. *Phys. Rev. Lett.*, 54:2441–2444, 1985.

[87] A. Wild, J. Sailer, J. Nutzel, G. Abstreiter, S. Ludwig, and D. Bougeard. *N. Jour. Phys.*, 12:113019, 2010.

[88] M. Thalakulam, C. B. Simmons, B. J. Van Bael, B. M. Rosemeyer, D. E. Savage, M. G. Lagally, M. Friesen, S. N. Coppersmith, and M. A. Eriksson. *Phys. Rev. B*, 84:045307, 2011.

[89] L. Gaudreau, S. A. Studenikin, A. S. Sachrajda, P. Zawadzki, A. Kam, J. Lapointe, M. Korkusinski, and P. Hawrylak. *Phys. Rev. Lett.*, 97:036807, 2006.

[90] B. M. Maune, M. G. Borselli, B. Huang, T. D. Ladd, P. W. Deelman, K. S. Holabird, A. A. Kiselev, I. Alvarado-Rodriguez, R. S. Ross, A. E. Schmitz, M. Sokolich, C. A. Watson, M. F. Gyure, and A. T. Hunter. *Nature (London)*, 481:344–374, 2012.

[91] T. Ando, A. B. Fowler, and F. Stern. *Rev. Mod. Phys.*, 54:437–672, 1982.

[92] S. Goswami, M. Slinker, K. A.and Friesen, L. M. McGuire, J. L. Truitt, C. Tahan, L. J. Klein, J. O. Chu, P. M. Mooney, D. W. van der Weide, R. Joynt, S. N. Coppersmith, and M. A. Eriksson. *Nat. Phys.*, 3:41, 2007.

[93] M. Friesen and S. N. Coppersmith. *Phys. Rev. B*, 81:115324, 2010.

[94] C. Tahan and R. Joynt. *Phys. Rev. B*, 89:075302, 2014.

[95] M. Jung, M. D. Schroer, K. D. Petersson, and J. R. Petta. *Appl. Phys. Lett.*, 100:253508, 2012.

[96] H. Qin and D. A. Williams. *Appl. Phys. Lett.*, 88:203506, 2006.

[97] R. J. Schoelkopf, P. Wahlgren, A. A. Kozhevnikov, P. Delsing, and D. E. Prober. *Science*, 280:1238–1242, 1998.

[98] C. B. Simmons, M. Thalakulam, B. M. Rosemeyer, B. J. Van Bael, E. K. Sackmann, D. E. Savage, M. G. Lagally, R. Joynt, M. Friesen, S. N. Coppersmith, and M. A. Eriksson. *Nano Letters*, 9:3234–3238, 2009.

[99] M. Raith, P. Stano, and J. Fabian. *Phys. Rev. B*, 86:205321, 2012.

[100] T. Fujisawa, D. G. Austing, Y. Tokura, Y. Hirayama, and S. Tarucha. *Nature (London)*, 419:278, 2002.

[101] C. H. Yang, A. Rossi, R. Ruskov, N. S. Lai, F. A. Mohiyaddin, S. Lee, C. Tahan, G. Klimeck, A. Morello, and A. S. Dzurak. *Nat Commun*, 4:2069, 2013.

[102] M. Pioro-Ladrière, T. Obata, Y. Tokura, Y.-S. Shin, T. Kubo, K. Yoshida, T. Taniyama, and S. Tarucha. *Nat. Phys.*, 4:776–779, 2008.

[103] E. A. Laird, J. M. Taylor, D. P. DiVincenzo, C. M. Marcus, M. P. Hanson, and A. C. Gossard. *Phys. Rev. B*, 82:075403, 2010.

[104] H. Bluhm, S. Foletti, D. Mahalu, V. Umansky, and A. Yacoby. *Phys. Rev. Lett.*, 105:216803, 2010.